IOWA STATE UNIVERSITY
Digital Repository

2012

Ab Initio Nuclear Structure Calculations for Light Nuclei

Robert Chase Cockrell
Iowa State University

Ab initio **nuclear structure calculations for light nuclei**

by

Chase Cockrell

A dissertation submitted to the graduate faculty

in partial fulfillment of the requirements for the degree of

DOCTOR OF PHILOSOPHY

Major: Nuclear Physics

Program of Study Committee:

James P. Vary, Major Professor

Cliff Bergman

Kai-Ming Ho

Craig Ogilvie

Kirill Tuchin

Iowa State University

Ames, Iowa

2012

DEDICATION

This thesis is dedicated to mt grandfather, William Hughes, PhD, ISU class of 1952. Without his encouragement, I might not be a scientist.

TABLE OF CONTENTS

LIST OF TABLES

LIST OF FIGURES

ACKNOWLEDGEMENTS

I would like to take this opportunity to thank those who have helped me conduct the research presented in this thesis. I would first like to thank Dr. James P. Vary for acting as my advisor and for his constant guidance throughout the past five years. I would also like to thank Dr. Pieter Maris for acting as a second advisor and for his assistance in performing large calculations. I would also like to thank my committee members for their efforts: Dr. Craig Ogilvie, Dr. Kai-Ming Ho, Dr. Kirill Tuchin, and Dr. Clifford Bergman.

ABSTRACT

We perform no-core full configuration calculations for the Lithium isotopes, ^{6}Li, ^{7}Li, and ^{8}Li with the realistic nucleon-nucleon interaction JISP16. We obtain a set of observables, such as spectra, radii, multipole moments, transition probabilities, etc., and compare with experiment where available. We obtain underbinding by 0.5 MeV, 0.7 MeV, and 1.0 MeV for ^{6}Li, ^{7}Li, ^{8}Li respectively. Magnetic moments are well-converged and agree with experiment to within 20%.

We then introduce the One-Body Density Matrix. We present a method to remove the spurious center-of-mass component from the space-fixed density distribution. We present space-fixed and translationally-invariant density distributions for various states of ^{6}Li, ^{7}Li, and ^{8}Li. We also examine select translationally-invariant density distributions from the ground state and several excited states of ^{9}Be. The resulting translationally-invariant densities can be used to examine convergence issues and better represent features of the nuclear shape. Convergence properties of these density distributions shed light on the convergence properties of experimental one-body observables.

We then present a method to calculate the space-fixed and translationally-invariant Wigner Function using our One-Body Density Matrices. We present a novel visualization of these Wigner Functions.

CHAPTER 1.   Introduction

The rapid development of *ab initio* quantum many-body methods for solving finite nuclei has opened a range of nuclear phenomena for evaluation to high precision using realistic inter-nucleon interactions. The many-body approach adopted in this work is referred to as the no-core full configuration (NCFC) method (1; 2; 3). The NCFC method produces the stationary state solutions of the nuclear Hamiltonian eigenvalue problem. The eigenvalues represent the many-body spectra and the eigenfunctions represent the wavefunctions. From the wavefunctions we evaluate additional experimental observables. When sufficient computational resources are available, we quantify uncertainties in the theoretical results.

We investigate light nuclei where spurious center of mass (cm) motion effects must be removed to ensure precise results. For this reason, the traditional harmonic oscillator (HO) basis is adopted. This enables us to isolate and remove spurious cm motion effects from all observables and from the one-body density matrices that encode reduced information derived from the many-body wavefunctions. A further advantage in using the HO basis is its ease in performing analytical evaluations and straightforward matrix element calculations (6).

We evaluate the nuclear Hamiltonian matrix and solve for its low-lying eigenvalues and eigenvectors using a set of finite set of single-particle HO states. The HO states are characterized by two basis space parameters, the HO energy $\hbar\Omega$ and the many-body basis space cutoff $N_{\max}$. $N_{\max}$ is defined as the maximum number of total oscillator quanta allowed in the many-body basis space above the minimum for that nucleus. Independence of both parameters $\hbar\Omega$ and $N_{\max}$ signals numerical convergence; for bound states, exact results are attained in the limit of a complete (infinite dimensional) basis. For the spectra we use an extrapolation to the complete basis space and we quantify the uncertainties due to the extrapolation.

In this work, we evaluate nucleon densities and observables such as spectra, radii, and

multipole moments. We work in a HO basis where the many-body wavefunctions are super-positions of Slater determinants. A Slater determinant of HO single-particle wavefunctions possesses 3A coordinates and is, therefore, overcomplete with respect to the internal (3A-3) coordinates. That is the superposition of Slater determinants produces wavefunctions that specify the motion of the cm of the system even though our nuclear Hamiltonian is free of cm components. Therefore, we adopt and develop techniques to control and remove the cm motion effects. In this work, we introduce a technique for unfolding the cm motion from the one-body density. This allows us to obtain the translationally-invariant densities, without any smearing effects from the cm motion. Indeed, as we will show, salient details of the density are often enhanced in the translationally-invariant density, compared to the single-particle densities that are commonly used in configuration interaction calculations.

We further investigate the properties of single-particle motion in the nucleus by considering its Wigner Function(7). This allows one to take an object used primarily to calculate static observables and consider dynamic processes.

1.1 Basic Terminology and Second-Quantized Notation

For the purposes of this work, several inner products and operators will now be defined using the traditional Dirac bra-ket notation and creation/destruction operators.

$$H_0 \mid \alpha \rangle \;=\; \epsilon_\alpha \mid \alpha \rangle \tag{1.1}$$

$$\langle \vec{r} \mid \alpha \rangle \;=\; \phi_\alpha(\vec{r}) \tag{1.2}$$

$$\langle \vec{q} \mid \alpha \rangle \;=\; \int d^3 r \langle \vec{q} | \vec{r} \rangle \langle \vec{r} | \alpha \rangle$$
$$= \widetilde{\phi_\alpha}(\vec{q}) \tag{1.3}$$

where H_0 is defined below, r represents a nucleon coordinate, q represents its momentum, and $\widetilde{\phi_i}$ is the Fourier transform of ϕ_i. Greek indeces such as α, β,etc. represent sets of single-particle quantum numbers and they are defined according to the chosen set of commuting observables appropriate for the system. For example, one may define a Greek index to represent, $\{n, l, m\}$ for a spinless particle in a spherical potential;$\{n, l, s, j, m_j\}$ for a particle with spin s in a spherical potential, etc. H_0 represents a generic single-particle Hamiltonian which gives an energy

eigenvalue ϵ_α when acting upon the state $|\alpha\rangle$. The $\phi(\vec{r})$'s are HO wavefunctions in coordinate space and the $\widetilde{\phi}(\vec{q})$ are HO wavefunctions in momentum space. The HO wavefunctions are further discussed in Section 1.4.

Second quantization provides a convenient formalism to express operators, basis states, and observables in the many-body framework. As this work is concerned solely with fermionic systems, we use the following conventions:

$$a_\alpha^\dagger \,|\,0\rangle \;=\; |\,\alpha\rangle \tag{1.4}$$

$$a_\alpha^\dagger \,|\,\alpha\rangle \;=\; 0 \tag{1.5}$$

$$a_\alpha \,|\,0\rangle \;=\; 0 \tag{1.6}$$

$$a_\alpha \,|\,\alpha\rangle \;=\; |\,0\rangle \tag{1.7}$$

$$\left\{a_\alpha, a_\beta^\dagger\right\} \;=\; \delta_{\alpha\beta} \tag{1.8}$$

$$\{a_\alpha, a_\beta\} \;=\; 0 \tag{1.9}$$

$$\left\{a_\alpha^\dagger, a_\beta^\dagger\right\} \;=\; 0 \tag{1.10}$$

Through Eq. 4, we see that when we act on the vacuum, represented by $|0\rangle$, with the creation operator, $a_\alpha^\dagger$, we obtain the state defined by $|\alpha\rangle$. Eq. 5 is a second-quantized form of the Pauli exclusion principle. Applying a raising operator to the same state does not create a second particle in the identical state. Eq. 6 shows that when an annihilation operator acts on the vacuum, a vanishing result is obtained, while in Eq. 7, an annihilation operator acts on its corresponding state, leaving only the vacuum. The remaining Eqs. 8-10 present the conventional anticommutation relations for fermions.

Second quantization allows one to write down the Hamiltonian and represent the basis states:

$$
\begin{aligned}
H_0 \;&=\; \sum_{\alpha,\beta}\langle \alpha \mid H_0 \mid \beta\rangle a_\alpha^\dagger a_\beta \\[2mm]
H_I \;&=\; \frac{1}{4}\sum_{\alpha,\beta,\gamma,\delta}\langle \alpha\beta \mid H_I^{(2)} \mid \gamma\delta\rangle a_\alpha^\dagger a_\beta^\dagger a_\delta a_\gamma \\[2mm]
&\quad +\frac{1}{36}\sum_{\alpha,\beta,\gamma,\delta,\epsilon,\zeta}\langle \alpha\beta\gamma \mid H_I^{(3)} \mid \delta\epsilon\zeta\rangle a_\alpha^\dagger a_\beta^\dagger a_\gamma^\dagger a_\zeta a_\epsilon a_\delta
\end{aligned}
\tag{1.11}
$$

$$+\frac{1}{576} \sum_{\alpha,\beta,\gamma,\delta,\epsilon,\zeta,\eta,\theta} \langle \alpha\beta\gamma\delta \mid H_I^{(4)} \mid \epsilon\zeta\eta\theta \rangle a_\alpha^\dagger a_\beta^\dagger a_\gamma^\dagger a_\delta^\dagger a_\theta a_\eta a_\zeta a_\epsilon \tag{1.12}$$

$$\mid \Phi_i \rangle \;\; = \;\; \{ a_\alpha^\dagger a_\beta^\dagger a_\gamma^\dagger ... a_\omega^\dagger \}_i \mid 0 \rangle = \mid \alpha, \beta, \gamma, ..., \omega \rangle \tag{1.13}$$

The first term in the expression given for H_I is the two-body interaction; the second term is the three-body interaction, and the third term is the four-body interaction. $H_I^{(K)}$ represents a K-body Hamiltonian. The fractional coefficients in front of the multi-body terms ensure that there is no over-counting, and can be easily calculated as $\frac{1}{(N_K!)^2}$, where N_K represents the number of independent "bodies" the Hamiltonian term incorporates.

Now, where repeated indices imply summation, the two-body Hamiltonian becomes:

$$\begin{aligned} H \;\; &= \;\; \frac{1}{4} \sum_{\alpha,\beta,\gamma,\delta} \langle \alpha\beta \mid H_I \mid \gamma\delta \rangle a_\alpha^\dagger a_\beta^\dagger a_\gamma a_\delta \\ &= \;\; \sum_{\alpha<\beta,\gamma<\delta} \langle \alpha\beta \mid H_I \mid \gamma\delta \rangle a_\alpha^\dagger a_\beta^\dagger a_\gamma a_\delta \\ &= \;\; \frac{1}{4} H_{\alpha\beta\gamma\delta} \alpha^\dagger \beta^\dagger \gamma\delta \end{aligned} \tag{1.14}$$

where we have omitted the superscript for compactness of notation as we address only NN interactions henceforth, and,

$$H_{\alpha\beta\gamma\delta} \equiv \langle \alpha\beta \mid H_I \mid \gamma\delta \rangle \tag{1.15}$$

Note that in the m-scheme, the NN interaction conserves angular momentum projection so that $m_\alpha + m_\beta = m_\gamma + m_\delta$.

1.2 Many-Body Methods

1.2.1 A Historical Overview of the Nuclear Shell Model

In 1932, Heisenberg ushered in the era of microscopic nuclear structure physics (8) by introducing the concept that protons and neutrons comprise the nucleus. Soon after, Bartlett (9) presented an analogy comparing the nucleus to an electronic system: "If an analogy with the external electronic system subsists, then the $\alpha-$particle may represent a closed s-shell, with two neutrons and two protons, while ^{16}O is obtained by adding on a closed p-shell with six neutrons and six protons." Bartlett continued to heavier systems, eventually making the claim that all nuclei with A$\leq$144 exhibit clear shell structure (10).

The nuclear shell model was then further explored by Elasser (11; 12; 13; 14). Elasser hypothesized that since, in contrast with the electronic shell model, there is no large central force to be considered, so the level structure may be different and should be explored with experiment. Elasser's analysis of $\alpha-$decays (13) showed that the proton and neutron shell closure numbers are independent of each other.

The shell model began to gain more widespread consideration in 1936 upon the publication of a famous review article by Bethe and Bacher (15). Bethe and Bacher made the claim that when a nucleus has a configuration resulting in all full shells, that nucleus would be particularly stable. They also made the claim that when a new shell is occupied, the binding energy of the particle in the new shell would be less than those particles that contributed to a closed shell. Bethe and Bacher also urged caution when comparing nuclear shell structure to electronic shell structure. They argued that the leading order approximation of single-nucleon energies alone would not be sufficient to predict shell structure. This approximation must be used in combination with inter-nucleon interactions and configuration mixing. They summarize: "Therefore, apparent deviations from the simple shell structure expected should of course be attributed to the crude approximation used. Under no circumstances do such deviations justify far-reaching ad hoc assumptions." However, they did go on to claim that the shell model theory will fail for heavier nuclei, though the claim was not fully justified.

There were no more significant shell model developments until 1948(16; 17; 18; 19). A wealth of experimental data had been acquired in the previous decade, and led Maria Goeppert Mayer (who won the Nobel Prize with Eugene Wigner and J. Hans Jensen in 1963) to make the claim that there is strong experimental evidence for the "magic numbers," 20, 50, 82, and 126. Her hypothesis was based on binding energies, isotopic abundance, and experimentally observed magnetic dipole moments. She showed that the nucleon separation energy was approximately 30% lower just beyond the magic numbers.

Drawing inspiration from Mayer, Feenberg and Hammack (20; 21) presented single-particle level schemes that worked with Mayer's magic numbers. Feenberg and Hammack claimed that the 2s orbit closed the shell at magic number 20, full 1f and 1g shells will be closed at magic number 50, and the 1h and 2d orbits are fully occupied at magic number 82. Nordheim (22)

agreed with the magic numbers, but not the level scheme presented by Feenberg and Hammack that reproduced them. Nordheim proposed that the 2s and 1d orbits closed to give the magic number 20, the 1f, 2p, and 2d orbitals are fully occupied for the magic number 50, and the 1g and 2f orbits are fully occupied for the magic number 82. There was not enough experimental evidence to determine which of the many shell closure possibilities led to the magic number, 126.

Progress in nuclear shell theory at this time was being held up by conflicts between magnetic dipole moment calculations based on model assumptions and experiment. Schmidt (23) proposed that the magnetic moments could be plotted as functions of spin. These plots would be known as "Schmidt lines." Schmidt found two parallel lines corresponding to the magnetic moments of even or odd nuclei. Because these lines did not closely intersect with experimental data, Schmidt claimed that the simple picture of the shell model must be augmented with corrections to explain the experimental deviation from calculation.

The behavior that Schmidt displayed was viewed as consistent with LS coupling, where L is the total orbital angular momentum for a nucleus and S is its total spin. The magnetic moments that lay close to a Schmidt line were considered evidence for a single value of L that couples to the spin. The problem with this is it became extremely difficult to construct closed shells at the higher magic numbers that were consistent with the experimental magnetic moments.

Mayer solved this problem in 1950 (19) by introducing a strong spin-orbit interaction in which state spins of odd-even nuclei were assumed to be given by the spin of the partially unoccupied orbital so that $J = j$, the total nuclear angular momentum equal to the total angular momentum of the single-particle filling the unoccupied shell. (19) explains all of the previously hypothesized magic numbers with a jj-coupling scheme in the shell model. This model was also discovered independently by Haxel, Jensen, and Seuss(24; 25). Though this phenomenological shell model is still not perfect, Mayer, Jensen, Haxel, and Seuss laid a foundation that is still used today and can even be found in the work presented in this thesis. Further, a main goal of this thesis is to derive nuclear structure features from first principles that are traditionally explained by the phenomenological shell model.

Until 1975, research into the phenomenological shell model was primarily focused on de-

termining effective NN interactions from experimental data and theoretical models of free NN interactions (26; 27; 28). Around 1975, a number of difficulties were encountered, including spurious CM contributions, the neglect of higher-body interactions (NNN and above), and poor convergence due to the tensor component of the NN force (Vary-Sauer-Wong effect). Progress was slow until the early 1990's, when significant computational resources became more available to the research community. This made new approaches, such as the No-Core Shell Model (NCSM), possible.

1.2.2 No-Core Shell Model

Traditionally, to calculate effective shell-model operators, a model space with a full closed shell core would be defined and additional nucleons would be restricted to the valence space, a set of single-particle states above the filled core states. For light nuclei, however, it is possible to consider a model space that allows all nucleons to contribute. This would be considered a No-Core Shell Model (NCSM). (29; 30)

In the NCSM, we begin with the translationally-invariant Hamiltonian for the A-nucleon system:

$$
\begin{aligned}
H_A \;=\; T_{\text{rel}} + V \;=\;& \frac{1}{A} \sum_{i<j} \frac{(\vec{p}_i - \vec{p}_j)^2}{2m} \\
& + \sum_{i<j} V_{ij} \,,
\end{aligned}
\tag{1.16}
$$

where m is the nucleon mass (in this case, taken to be 938.92 MeV, the average of the proton and neutron masses), and V_{ij} is the combination of the NN interaction and the Coulomb interaction. We specifically discuss NN interactions in what follows but the techniques are easily generalized to input multi-body interactions. Next, we add the HO cm Hamiltonian to Eq. 1.16 where:

$$
H_{cm} \;=\; T_{cm} + U_{cm}
\tag{1.17}
$$

$$
U_{cm} \;=\; \frac{1}{2} A m \Omega \vec{R}^2
\tag{1.18}
$$

$$
\vec{R} \;=\; \frac{1}{A} \sum_{i=1}^{A} \vec{r}_i .
\tag{1.19}
$$

The HO H_{cm} will be subtracted later so that it does not influence the translationally invariant properties of the many-body system. The addition of the HO cm term is convenient, and allows

us to write the modified Hamiltonian:

$$H_A^\Omega = \sum_{i=1}^{A} T_i + \sum_{i<j} V_{ij} + \sum_{i=1}^{A} \frac{1}{2} Am\Omega^2 \vec{r}_i^2 \qquad (1.20)$$

$$= \sum_{i=1}^{A} h_i + \sum_{i<j}^{A} \left[V_{ij} - \frac{m\Omega^2}{2A} (\vec{r}_i - \vec{r}_j)^2 \right] \qquad (1.21)$$

where we have,

$$h_i = -\frac{\hbar^2}{2m} \nabla_i^2 + \frac{1}{2} m\Omega \vec{r}_i^2. \qquad (1.22)$$

We then follow Da Providencia and Shakin (31) and Lee, Suzuki, and Okamoto (32) and perform a unitary transformation of the Hamiltonian, which accommodates short-range two-body correlations:

$$\mathcal{H} = e^{-S} H_A^\Omega e^S. \qquad (1.23)$$

We choose S such that $\mathcal{H}$ and H_A^Ω have the same symmetries and eigenspectra in the subspace $\mathcal{K}$ of the full Hilbert space. The subspace is defined by the chosen cutoff N_{max} introduced above.

We now develop an a-body $(a \leq A)$ effective Hamiltonian:

$$\mathcal{H} = \mathcal{H}^{(1)} + \mathcal{H}^{(A)} \qquad (1.24)$$

where,

$$\mathcal{H}^{(1)} = \sum_{i=1}^{A} h_i \qquad (1.25)$$

$$\mathcal{H}^{(A)} = \frac{\binom{A}{2}}{\binom{A}{a}\binom{a}{2}} \sum_{i_1<i_2<...<i_a}^{A} \widetilde{V}_{i_1 i_2 ... i_a}, \qquad (1.26)$$

with,

$$\widetilde{V}_{i_1 i_2 ... i_a} = e^{-S^{(a)}} H_a^\Omega e^{S^{(a)}} - \sum_{i=1}^{a} h_i \qquad (1.27)$$

where $S^{(a)}$ is an a-body operator;

$$H_a^\Omega = \sum_{i=1}^{a} h_i + \sum_{i<j}^{a} V_{ij} \qquad (1.28)$$

Thus, the effective Hamiltonian, $\mathcal{H}_{N_{max},\Omega}$, on the subspace $\mathcal{K}$ of the full Hilbert space can be expressed as a sum of progressively higher many-body interactions (30):

$$\mathcal{H}_{N_{max},\Omega}^{(A)} \;\; = \;\; \mathcal{H}^{(1)} + \mathcal{V}_{N_{max},\Omega}^{(2)} + \mathcal{V}_{N_{max},\Omega}^{(3)} + ... + \mathcal{V}_{N_{max},\Omega}^{(A)} \tag{1.29}$$

where $\mathcal{V}_{N_{max},\Omega}^{(a)}$ is an a-body interaction operator. Recall from Eq. 1.7 that when an N-body operator acts on an system of a nucleons, the result is zero when $a < N$. Therefore, we define the Hamiltonian shown in Eq. 1.29 as the effective Hamiltonian on the Hilbert space given by our N_{max} truncation. Thus, the sequence of interactions, $\mathcal{V}_{N_{max},\Omega}^{(2)}, \mathcal{V}_{N_{max},\Omega}^{(3)}, ..., \mathcal{V}_{N_{max},\Omega}^{(A)}$ provide the building blocks to construct the complete A-body Hamiltonian.

In the NCSM, we observe that as $N_{max} \to \infty$, Eq. 1.29 will need only the original interactions as the full Hilbert space is recovered. Because it is not practical to take $N_{max} \to \infty$, we must select a calculable subspace in Eq. 1.29. We seek to achieve a large enough value for N_{max} and the number of bodies, a, so that we can truncate Eq. 1.29 after few (2 or 3) body terms.

We can divide the full space into a model space defined by the value of N_{max} and the Q space representing what is omitted from the P space. We use the operators P and Q with $P + Q = 1$. Now it is possible to specify the transformation operator, S_a using the decoupling condition:

$$Q_a e^{-S^{(a)}} H_a^{\Omega} e^{S^{(a)}} P_a \;\; = \;\; 0 \tag{1.30}$$

where,

$$P_a S^{(a)} P_a = Q_a S^{(a)} Q_a = 0 \tag{1.31}$$

This method is known as the unitary-model-operator approach (96). It a solution of the form:

$$S^{(a)} \;\; = \;\; arctanh(\omega - \omega^{\dagger}) \tag{1.32}$$

where the operator, ω, satisfies the condition:

$$\omega \;\; = \;\; Q_a \omega P_a. \tag{1.33}$$

After this point, the sequence of calculational ingredients is the same as in the NCFC approach, and is described below.

1.2.3   No-Core Full Configuration

The NCFC approach is similar to the NCSM (29). The main differences are that in the NCFC approach we do not use the Lee–Suzuki renormalization procedure (33) which is commonly employed in the NCSM; and more importantly, we retain the variational principle and estimate the numerical accuracy of our results based on the rate of convergence and dependence on the basis space parameters (2; 3).

We begin with the translationally-invariant Hamiltonian for the A-body system in relative coordinates, shown in Eq. 15. All many-body basis states are included with HO quanta up to and including the amount governed by the N_{max} truncation. Thus, if the highest HO single-particle state for the minimal HO configuration has N_0 HO quanta, then the highest allowed single-particle state in the truncated basis will have $N_0 + N_{\mathrm{max}}$ HO quanta. Furthermore, our calculations are 'No-Core' configuration interaction calculations. This means that all nucleons participate in the interactions on an equal footing.

As we increase N_{max}, and approach convergence, we expect physical observables to become independent of both the HO parameter $\hbar\Omega$ and the truncation parameter N_{max}. However, due to current limits to our finite basis, our calculations do show some parameter dependence, even in the largest basis spaces. As we discuss shortly, we apply previously established extrapolation tools to take the continuum limit of the binding energy.

The HO basis for single-particle states, in combination with this many-particle N_{max} truncation, leads to exact factorization of the nuclear wavefunctions into a cm wavefunction and a translationally-invariant (ti) wavefunction:

$$\Psi(\vec{r_i}) \;\; = \;\; \Phi_{\mathrm{cm}}^{\Omega}(\vec{R}) \otimes \phi_{\mathrm{ti}} \tag{1.34}$$

where $\vec{R} = (\frac{1}{A}) \sum_{i=1}^{A} \vec{r_i}$ and ϕ_{ti} depends only on intra-nucleon coordinates. In order to separate the cm excited states from the low-lying states of interest, we adopt the Lawson method (34) whereby we add a Lagrange multiplier term, $\lambda(H_{\mathrm{cm}}^{\Omega} - \frac{3}{2}\hbar\Omega)$, to the many-body Hamiltonian, Eq. 1.16,

$$H \;\; = \;\; H_A + \lambda(H_{\mathrm{cm}} - \frac{3}{2}\hbar\Omega) \,. \tag{1.35}$$

The "3/2 hw" factor represents the zero point energy of the cm motion. With λ positive, states with cm excitations are separated by multiples of $\lambda\hbar\Omega$ from the states with the lowest HO cm motion. Since the Lagrange multiplier term acts only on the cm coordinate, it is independent of the intra-nucleon coordinates and it does not affect the energy eigenvalues or the translationally-invariant wavefunctions ϕ_{ti} of the low-lying states. Indeed, observables for the low-lying states are independent of λ, as long as $\lambda\hbar\Omega$ is much larger than the excitation energy of the highest state of interest.

In the truncated basis space, we can now write the many-body Schrödinger equation as a finite matrix equation with a real, symmetric, sparse matrix. The eigenvalues of this matrix give us the binding energy, and the corresponding eigenvectors give us the wavefunctions. In any finite basis space, the eigen-energies satisfy the variational principle and show uniform and monotonic convergence from above with increasing $N_{\max}$, allowing for extrapolation to the infinite basis space. To obtain the extrapolated gs energy $E_{gs}(\infty)$, we use a fitting function of the form:

$$E_{gs}(N_{\max}) \;=\; a \,\exp(-c\,N_{\max}) + E_{gs}(\infty) \,. \tag{1.36}$$

This is an empirical method (1; 2; 3) that is valid within estimated uncertainties that we now define. We assign equal weight to each of three successive values of $N_{\max}$ at a fixed $\hbar\Omega$ and perform a regression analysis. The difference between extrapolated results from two consecutive sets of three $N_{\max}$ values is used as the estimate of numerical uncertainty associated with the extrapolation. The optimal $\hbar\Omega$ value for this extrapolation appears to be the $\hbar\Omega$ that minimizes the difference between the extrapolated energy and the result at the largest $N_{\max}$. Typically, this corresponds to a $\hbar\Omega$ value slightly above the variational minimum. Of course, the extrapolated results should be independent of $\hbar\Omega$, within their numerical error estimates, and we do check for such consistency. Furthermore, we often adjust our numerical error estimate by considering the results over a range of 5 MeV in $\hbar\Omega$.

For other observables, we do not have a robust and reliable extrapolation method; we therefore use the degree of (in)dependence from the basis space parameters $\hbar\Omega$ and $N_{\max}$ as a measure for convergence as we describe further below on a case-by-case basis.

1.3   Wavefunctions

In the many-body framework that we are using, we expand the nuclear wavefunction Ψ in a basis of Slater determinants of single-particle HO states. Note that we use single-particle coordinates, rather than relative coordinates, in the nuclear wavefunction. That means that our wavefunctions, and therefore, our one-body density matrices calculated as expectation values of one-body operators, will include cm motion.

The normalized wavefunction is given by the slater determinant:

$$
\Psi = \frac{1}{\sqrt{n!}}
\begin{vmatrix}
\phi_{a_1}(x_1) & \phi_{a_1}(x_2) & ... & \phi_{a_1}(x_n) \\
\phi_{a_2}(x_1) & \phi_{a_2}(x_2) & ... & \phi_{a_2}(x_n) \\
\vdots & \vdots & & \vdots \\
\phi_{a_n}(x_1) & \phi_{a_n}(x_2) & ... & \phi_{a_n}(x_n)
\end{vmatrix}
\tag{1.37}
$$

(50) The ϕ's are single-particle Three Dimensional Harmonic Oscillator Wavefunctions (TD-HOWF). The TDHOWF potential is given by:

$$
U(r) = \frac{1}{2} m\Omega^2 r^2
\tag{1.38}
$$

where m represents the mass of the nucleon, which we take to be average of the neutron and proton mass (938.92 MeV). Insertion of this potential into the Schrödinger equation with the simplification $\nu \equiv \frac{m\Omega}{2\hbar}$, we obtain the wavefunction:

$$
\psi_{nlmm_s} = N_{nl} r^l e^{-\nu r^2} L_n^{l+\frac{1}{2}}(2\nu r^2) Y_l^m(\theta, \phi) \chi_{s_\alpha m_s}
\tag{1.39}
$$

where $L_n^{l+\frac{1}{2}}(2\nu r^2)$ represents an associated Laguerre Polynomial and is defined using the Rodrigues formula:

$$
L_\mu^q(z) = \frac{e^z z^{-q}}{\mu!} \frac{d^\mu}{dz^\mu}(z^{\mu+q} e^{-z}),
\tag{1.40}
$$

$Y_l^m(\theta, \phi)$ is a spherical harmonic, and $\chi_{s_\alpha m_s}$ is a Pauli spinor. The normalization factor, N_{nl}, is given by:

$$
N_{nl} = \sqrt{\frac{2(2\nu)^{l+3/2}\Gamma(n+1)}{\Gamma(n+l+3/2)}}
\tag{1.41}
$$

(30)(51)

When using an LS coupling configuration, a group of single-particle states is specified by the orbits of each particle, denoted by n, the radial quantum number, and l, the orbital angular momentum. For the case of coupled orbital and spin motion (coupled j representation), n and l are used in combination with j, the total angular momentum of the single-particle. In order to completely describe the many-body state, additional quantum numbers, such as m_j for the coupled-j representation or m_l, m_s for LS coupling, are necessary, depending on whether LS-coupling or j-coupling is utilized (50). We call this the m-scheme because particle states have specific m-values. It is important to note that for NN interactions, angular momentum projection is conserved. The m-scheme and its associated symmetries are employed in this work along with the coupled-j representation.

1.4 The JISP16 Interaction

1.4.1 A General History of NN Interactions

NN interactions, in general, are derived using the wealth of NN data that has been experimentally observed, such as deuteron properties and scattering phase shifts. These interactions could, in principle, be calculated from first principles using quantum chromodynamics, though practically, this is currently not feasible. That is, successes with such derived interactions have been quite limited (35)(36), in contrast with the potentials fit to the NN data.

The first NN interaction was presented in 1935 by Yukawa (37). Yukawa drew inspiration from Bohr, Heisenberg, and Jordan (38), who, when they quantized the electromagnetic field in 1925, showed that electromagnetic interactions were mediated by virtual particles (virtual photons). Yukawa claimed that the inter-nucleon interactions were mediated by a (then theoretical) particle he called the meson. Yukawa's potential has the form:

$$V(r) \;\; = \;\; -g^2 \frac{e^{-\mu r}}{r} \tag{1.42}$$

where g is an adjustable coupling constant and $\mu = mc/\hbar$.

The Yukawa potential successfully reproduced much experimental low-energy NN scattering data. Yukawa then augmented his potential with spin-dependence and a tensor force arising from the one-pion exchange potential (OPEP)(30).

Many scientists built on Yukawa's work. Many attempts were made at adding a repulsive "hard core" to Yukawa's potential (39), though the most popular modification came from Reid with his soft-core potential(40). Modern potentials generally fit NN data to a high degree of accuracy, such as the NN interaction adopted here and described below. In contrast to the work of Yukawa and others that adopt a local NN interaction form, the one we employ is non-local and therefore challenging to present in graphical form.

1.4.2 JISP16

The selection of an appropriate potential is one of the major factors that determines how well one's calculation compares to experiment. We adopted the NN interaction JISP16 (J-matrix Inverse Scattering Potential optimized for nuclei up to ^{16}O). JISP16 is a realistic NN interaction initially developed from NN data using inverse scattering techniques. It is then adjusted with phase-shift equivalent unitary transformations to describe light nuclei without explicit three-body interactions (52; 53; 54). JISP16 provides good convergence rates for the ground state (gs) energies of nuclei with $A \leq 16$.

JISP16 is constructed in a HO basis using the J-matrix formalism of inverse scattering theory. The NN potential matrix is obtained for individual partial waves independently. JISP16 can be thought of as an effective interaction since it has been phenomenologically tuned to successfully reproduce energies and various observables for relatively light nuclei ($A \leq 16$). As such, it can be treated as a realistic NN interaction which simulates (through the phenomenological tuning) NNN interaction contributions. One of the goals of this work is to derive an extensive set of results for the Li isotopes that greatly expand the available results for JISP16 to compare with experiment.

Though it is known that certain effects, e.g., meson exchange currents, can contribute significantly to certain observables (i.e., magnetic moments and transitions), we do not take these effects explicitly into account. We may therefore expect some deviation from experiment. This is discussed in greater detail below (see discussion on calculated magnetic observables).

In order to eliminate ambiguities arising from the phase-equivalent transformation, we invoke a phenomenological ansatz that the NN potential matrix for uncoupled partial waves is

a tridiagonal matrix, which would make the JISP16 potential an inverse scattering tridiagonal potential (ISTP). This provides computational simplicity and storage benefits in that the ISTP matrix has the minimum number of non-vanishing off-diagonal NN matrix elements for any basis space.

In order to fully understand the J-matrix inverse scattering approach, we summarize several defining relations here(54). The Schrdinger equation for a partial wave with fixed orbital angular momentum, l, is:

$$H^l \psi_{lm}(E, \vec{r}) = E\psi_{lm}(E, \vec{r}) \tag{1.43}$$

where $\psi_{lm}(E, \vec{r}) = \frac{u_l(E,r)}{r} Y_l^m(\hat{r})$. The radial component of the wavefunction is expanded in terms of radial HOWF's, defined above:

$$u_l(E, r) = \sum_{n=0}^{\infty} a_{nl}(E) R_{nl}(r) \tag{1.44}$$

This wavefunction is a solution to the infinite set of equations:

$$\sum_{n'=0}^{\infty} (H_{nn'}^l - \delta_{nn'} E) a_{n'l}(E) = 0 \tag{1.45}$$

where the Hamiltonian is defined such that:

$$H_{nn'}^l = T_{nn'}^l + V_{nn'}^l \tag{1.46}$$
$$T_{n,n-1}^l = -\frac{1}{2}\sqrt{n(n+l+1/2)} \tag{1.47}$$
$$T_{n,n}^l = \frac{1}{2}(2n+l+3/2) \tag{1.48}$$
$$T_{n,n+1}^l = -\frac{1}{2}\sqrt{(n+1)(n+l+3/2)} \tag{1.49}$$
$$\tag{1.50}$$

$V_{nn'}^L$ is assumed to be non-vanishing for the same matrix entries as the kinetic energy operator and has an upper limit to n and n', above which it is taken to be zero. This defines a cutoff in the model space for $V_{nn'}^L$ which we define as N (n and $n' \leq N$). Above that cutoff, the model space, shown in Eq. 1.45 takes the form:

$$T_{n,n-1}^l a_{n-1,l}(E) + (T_{nn}^l - E)a_{nl}(E) + T_{n,n+1}^l a_{n+1,l}(E) = 0 \tag{1.51}$$

This equation produces two independent solutions. These solutions can be taken to be a superposition of regular solutions, $S_{nl}(E)$, and irregular solutions, $C_{nl}(E)$, where:

$$a_{nl}(E) = cos\delta(E)S_{nl}(E) + sin\delta(E)C_{nl}(E) \tag{1.52}$$

and

$$S_{nl}(E) = \sqrt{\frac{\pi\nu n!}{\Gamma(n+l+3/2)}}q^{l+1}\exp(-q^2/2)L_n^{l+1/2}(q^2) \tag{1.53}$$

$$C_{nl}(E) = (-1)^l\sqrt{\frac{\pi\nu n!}{\Gamma(n+l+3/2)}}\frac{1}{q^l\Gamma(1/2-l)}\exp(-q^2/2)\Phi(-n-l-1/2,-l+1/2;q^2) \tag{1.54}$$

where $\Phi(a,b;z)$ is a confluent hypergeometric function (55), where $q = \sqrt{2E}$ and $\delta(E)$ is the scattering phase shift.

For the internal portion of the model space, the solutions for $a_{nl}(E)$ are given by:

$$a_{nl}(E) = G_{nN}T_{N,N+1}^l a_{N+1,l}(E) \tag{1.55}$$

where the matrix elements

$$G_{nn'} = -\sum_{\lambda'=0}^{N}\frac{\langle n|\lambda'\rangle\langle\lambda'|n'\rangle}{E_{\lambda'}-E} \tag{1.56}$$

are calculated using eigenvalues, (E_λ), and eigenvector components, $(\langle n|\lambda\rangle)$, of the truncated Hamiltonian. One can calculate the phase shift for orbital angular momentum l at energy at the center-of-mass scattering energy E using the relation:

$$tan\delta(E) = -\frac{S_{Nl}(E)-G_{NN}T_{N,N+1}^l S_{N+1,l}(E)}{C_{Nl}(E)-G_{NN}T_{N,N+1}^l C_{N+1,l}(E)} \tag{1.57}$$

In the inverse scattering J-matrix approach, we take the phase shift from Eq. 1.57 to be known at any energy. The eigenvalues and eigenvectors are then extracted from this information. This is performed by first assigning a rank to the desired potential matrix (N). For a finite-dimensional matrix, it will be possible to define the phase shift for a finite energy interval. As the matrix increases in rank, the phase shift is able to be defined for larger and larger energy intervals.

Knowing the phase shift $\delta(E)$, we can use Eq. 1.52 to calculate $a_{N+1,l}(E)$. One can find the eigenvalues, E_λ through the transcendental equation:

$$a_{N+1,l}(E_\lambda) = 0 \tag{1.58}$$

In order to calculate the eigenvectors, it can be shown that:

$$a_{Nl}(E_\lambda) = |\langle N|\lambda\rangle|^2 \alpha_l^\lambda T_{N,N+1}^l \tag{1.59}$$

where,

$$\alpha_l^\lambda = \frac{da_{N+1,l}(E)}{dE}\Big|_{E=E_\lambda} \tag{1.60}$$

The eigenvectors of the truncated Hamiltonian should be orthonormal such that:

$$\sum_{\lambda=0}^{N} \langle n|\lambda\rangle\langle\lambda|n'\rangle = \delta_{nn'} \tag{1.61}$$

Because $\langle N|\lambda\rangle$'s are components of the eigenvectors, we should have:

$$\sum_{\lambda=0}^{N} \langle N|\lambda\rangle\langle\lambda|N\rangle = 1 \tag{1.62}$$

though, in general, this is violated. While $\langle N|\lambda\rangle$ can describe the phase shifts, it cannot be used to construct a Hermitian Hamiltonian matrix. In order to work around this problem, we modify Eq. 1.62 so that $\langle N|\lambda = N\rangle$ corresponds to the highest eigenvalue, E_N. Because this voids the description of phase shifts at energies that differ from the highest eigenvalue, the phase shift description is restored through variation of E_N.

It should be noted that any of the phase equivalent transformations employed that do not change both the truncated eigenvalues and eigenvector components, give a potential matrix that leads to the same $\delta(E)$ phase shift for all values of E. In order to resolve this ambiguity, we invoke the ansatz mentioned above that the potential matrix is tridiagonal, as discussed in (54). The Hamiltonian can then be defined:

$$H_{00}^l\langle 0|\lambda\rangle + H_{01}^l\langle 1|\lambda\rangle = E_\lambda\langle 0|\lambda\rangle \tag{1.63}$$

$$H_{n,n-1}^l\langle n-1|\lambda\rangle + H_{nn}^l\langle n|\lambda\rangle + H_{n,n+1}^l\langle n+1|\lambda\rangle = E_\lambda\langle n|\lambda\rangle \tag{1.64}$$

$$H_{N,N-1}^l\langle N-1|\lambda\rangle + H_{NN}^l\langle N|\lambda\rangle = E_\lambda\langle N|\lambda\rangle \tag{1.65}$$

Once the Hamiltonian matrix elements have been calculated, the potential interaction matrix elements can be trivially extracted:

$$V_{nn}^l = H_{nn}^l - T_{nn}^l \tag{1.66}$$

$$V_{n,n\pm1}^l = H_{n,n\pm1}^l - T_{n,n\pm1}^l \tag{1.67}$$

1.4.3 Previous Calculations with JISP16

Over the past decade, the JISP16 interaction has been used quite successfully to describe ground state energies, as can be seen in Table 1.1. Table 1.1 displays recent published calculations of ground state energies using both the full JISP16 interaction and the bare interaction and compares with experiment. One of the goals of the present work is to increase the size of the model space for ^{6}Li and ^{7}Li from $N_{max} = 12, 10$ to $N_{max} = 16, 14$ for ^{6}Li and ^{7}Li respectively. We also add data for ^{8}Li. While the work in the table was performed using either NCSM or NCFC calculations, JISP16 has been used by a variety of groups using a range of *ab initio* techniques, as will be discussed below.

The hyperspherical harmonic approach has been used in combination with JISP16 (42)(43) in order to calculate various observables in ^{3}H, ^{3}He, ^{6}Li and ^{6}He. These results compare favorably with our results as can be seen in Tables 1.2 and 1.3. In these tables, we present binding energies and Gamow-Teller matrix elements calculated in the NSCM/NCFC approach and compare with the hyperspherical harmonic approach and experiment. We can see that not only are the two methods in good agreement with each other, but in agreement with experiment as well.

JISP16 has also been used in the Monte Carlo Shell Model (MCSM) (44). Results obtained in the MCSM compare well to those obtained in the NCSM/NCFC approach. In Table 1.4, we display results for binding energies, root-mean-square (RMS) radii, and magnetic dipole moments. The discrepancy between the two methods is generally less than a few percent.

One of the greatest triumphs of the JISP16 interaction is the prediction and subsequent observation of the low-lying spectroscopy of the exotic, highly unstable, ^{14}F(45)(46). *A*b initio calculations performed with JISP16 predicted a 1^- excited state between the 2^- gs and the 2nd excited state, a 3^- state. These papers showed that *a*b initio techniques using the JISP16 interaction are useful for much more than a theoretical verification of experiment; the calculations can also be used to make predictions and guide experiment.

Not only does JISP16 have a successful history of comparison to the gs energies and spectra of light nuclei, it successfully describes the NN data with good precision.. When compared with

the 1992 np database, JISP16 has a $\chi^2/d = 1.03$ and $\chi^2/d = 1.05$ for the 1999 np database (47). In Table 1.5 we show the χ^2/d measurement for several of the current popular potentials. We see that JISP16 is comparable to other contemporary potential, with the exception of the N3LO NN interaction, which JISP16 outperforms considerably.

1.5 Lanczos Algorithm

Because the matrix is extremely sparse, we employ the Lanczos algorithm. The Lanczos algorithm is a well-known adaptation of power methods to determine eigenvalues and eigenvectors. It is particularly useful for sparse matrices (56), to perform a partial diagonalization of the Hamiltonian matrix.

Lanczos recursion was first described in (57) and forms the backbone of various procedures used to compute eigenvalues and eigenvectors of real symmetric matrices. The basic algorithm is described below, where we begin with an n-dimensional, square, real, symmetric matrix, denoted by $\mathbf{M}$, and $\vec{v}_1$ as a randomly generated vector with unit norm. We also define $\beta_1 \equiv 0$ and $v_0 \equiv 0$. Now, for i=1,2,...m, we need to define the Lanczos vector, $\vec{v}_i$ as well as the scalar quantities, α_i and β_{i+1}:

$$\alpha_i \equiv \vec{v}_i^T \mathbf{M} \vec{v}_i \tag{1.68}$$

$$\beta_{i+1} \vec{v}_{i+1} = \mathbf{M} \vec{v}_i - \alpha_i \vec{v}_i - \beta_i \vec{v}_{i-1} \tag{1.69}$$

$$\beta_{i+1} \equiv \vec{v}_{i+1}^T \mathbf{M} \vec{v}_i \tag{1.70}$$

For m=1,2,...n, we define a tri-diagonal Lanczos matrix, $\mathbf{T}_m$, which has the following form:

$$\mathbf{T}_m = \begin{bmatrix} \alpha_1 & \beta_2 & & & & 0 \\ \beta_2 & \alpha_2 & \beta_3 & & & \\ & \beta_3 & \alpha_3 & \ddots & & \\ & & \ddots & \ddots & \beta_{m-1} & \\ & & & \beta_{m-1} & \alpha_{m-1} & \beta_m \\ 0 & & & & \beta_m & \alpha_m \end{bmatrix} \tag{1.71}$$

It can be seen that $\vec{v}_{i+1}$ is calculated by orthogonalizing the vector $\mathbf{M}\vec{v}_i$ with respect to the previously calculated vectors, $\vec{v}_{i-1}$ and $\vec{v}_i$.

When full convergence is reached,

$$\mathbf{T}_m \;\; = \;\; \bar{\mathbf{V}}\mathbf{M}\mathbf{V} \tag{1.72}$$

where the transformation matrix, $\mathbf{V}$ comprises the vectors $\vec{v}_i$. One can approximate the eigenvalues of $\mathbf{M}$ by using the eigenvalues of $\mathbf{T}_m$ (56). The eigenvectors of $\mathbf{M}$ can be simply calculated by multiplying the transformation matrix, $\mathbf{V}$ by the eigenvectors of $\mathbf{T}_m$.

Nucleus	Experiment	Bare	Effective	$\hbar\Omega$	N_{max}
^{3}H	8.482	8.354	8.496(20)	7	14
^{3}He	7.718	7.648	7.797(17)	7	14
^{4}He	28.296	28.297	28.374(57)	10	14
^{6}He	29.269	-	28.32(28)	17.5	12
^{6}Li	31.995	-	31.00(31)	17.5	12
^{7}Li	39.245	-	37.59(30)	17.5	10
^{7}Be	37.600	-	35.91(29)	17	10
^{8}Be	56.500	-	53.40(10)	15	8
^{9}Be	58.165	53.54	54.63(26)	16	8
^{9}B	56.314	51.31	52.53(20)	16	8
^{10}Be	64.977	60.55	61.39(20)	19	8
^{10}B	64.751	60.39	60.95(20)	20	8
^{10}C	60.321	55.26	56.36(67)	17	6
^{11}B	76.205	69.2	73.0(31)	17	6
^{11}C	73.440	66.1	70.1(32)	17	6
^{12}B	79.575	71.2	75.9(48)	15	6
^{12}C	92.162	87.4	91.0(49)	17.5	6
^{12}N	74.041	64.5	70.2(48)	15	6
^{13}B	84.453	73.5	82.1(67)	15	6
^{13}C	97.108	93.2	96.4(59)	19	6
^{13}N	94.105	89.7	93.1(62)	18	6
^{13}O	75.558	63.0	72.9(62)	14	6
^{14}C	105.285	101.5	106.0(93)	17.5	6
^{14}N	104.659	103.8	106.8(77)	20	6
^{14}O	98.733	93.7	99.1(92)	16	6
^{15}N	115.492	114.4	119.5(126)	16	6
^{15}O	111.956	110.1	115.8(126)	16	6
^{16}O	127.619	126.2	133.8(158)	15	6

Table 1.1 Binding energies (in MeV) of nuclei obtained with the bare and effective JISP16 interaction are compared with experiment. The results presented in this work update the Li isotope entries in this table. Uncertainties are defined in Sec. 1.2 and apply to the corresponding number of significant figures as appear in parenthesis. (41)

Nucleus	Experiment	NCSM/NCFC	Hyperspherical Harmonic
^{3}H	8.482	8.496(20)	8.367(20)
^{3}He	7.718	7.797(17)	7.661(17)
^{6}He	29.269	28.70(13)	28.32(28)
^{6}Li	31.995	31.46(5)	31.49(3)

Table 1.2   Binding energies of light nuclei calculated using the NCSM/NCFC approach are compared with those calculated in the Hyperspherical Harmonic approach and experiment. Theory results are based on the JISP16 NN interaction. Energies are given in MeV. Hyperspherical Harmonic energies are taken from (42)(43) Uncertainties are defined in Sec. 1.2 and apply to the corresponding number of significant figures as appear in parenthesis.

Nucleus	Experiment	NCSM/NCFC	Hyperspherical Harmonic
^{6}Li	2.161	2.225(2)	2.227(2)

Table 1.3   GT matrix elements of ^{6}Li calculated using the NCSM/NCFC approach are compared with those calculated in the Hyperspherical Harmonic approach and experiment. Hyperspherical Harmonic matrix elements are taken from (43).

Nucleus	Method	E(MeV)	$\langle r^2 \rangle^{1/2}$(fm)	$\mu(\mu_N)$
^{4}He	NCFC	28.738	1.379	
	MCSM	28.738	1.379	
^{6}He	NCFC	23.684	1.813	
	MCSM	23.701	1.813	
^{6}Li	NCFC	27.168	1.846	0.832
	MCSM	27.168	1.846	0.835
^{7}Li	NCFC	-33.202	1.901	2.993
	MCSM	-33.276	1.899	3.036
^{8}Be	NCFC	-50.756	1.960	
	MCSM	-50.756	1.957	
^{10}B	NCFC	-42.338	1.836	0.509
	MCSM	-42.331	1.837	0.503
^{12}C	NCFC	-76.621	1.723	
	MCSM	-76.621	1.723	

Table 1.4   Various observables calculated in the MCSM approach and the NCSM approach are compared. MCSM results are taken from (44). NCSM/NCFC results are taken from (2). In both cases, JISP16 was used as the NN interaction Comparisons were made a similar sized model spaces, defined in (44).

Interaction	1992	1999
JISP16	1.03	1.05
AV18	1.08	1.07
CD-Bonn	1.03	1.02
N3LO	-	1.10

Table 1.5 χ^2/d values are shown for various NN interactions for the 1992 and 1999 np databases. JISP16 values are from (47). N3LO values are from (48). Other values can be found in (49).

CHAPTER 2.   The One Body Density Matrix

2.1   Background and Definitions

The One Body Density Matrix (OBDM) was first introduced by Löwdin in 1955 (93). The nonlocal version is defined:

$$\rho(\vec{x}_1', \vec{x}_1) \;=\; A \int \Psi^*(\vec{x}_1', \vec{x}_2, ..., \vec{x}_A)\Psi(\vec{x}_1, \vec{x}_2, ..., \vec{x}_A)d^3x_2....d^3x_A \tag{2.1}$$

Where Ψ's are the many-body wavefunctions defined in section 1 and A is the total number in nucleons. The vector $\vec{x}_i$ represents a combination of a spatial coordinate, $\vec{r}_i$, and a spin coordinate, $\vec{s}_i$. Including spin as well as other quantum numbers (such as isospin) is straightforward so we will not burden the notation with these complexities at the present level of treatment. The diagonal elements represent the local OBDM and are represented by $\rho(\vec{x_1}, \vec{x_1})$. The non-local OBDM can be related to the local OBDM through the relation:

$$\rho(\vec{x_1}) \;=\; \int \rho(\vec{x_1}', \vec{x_1})\delta(\vec{x_1} - \vec{x_1}')d^3x_1' \tag{2.2}$$

These are normalized such that:

$$\int \rho(\vec{x}_1)d^3x_1 \;=\; A \tag{2.3}$$

and we say that the probability to find the particle in question in the region $d\vec{x}$ is $\rho(\vec{x})d\vec{x}$. We will begin to define the OBDM in terms of single particle wavefunctions instead of many-body wavefunctions. As such, the numerical subscripts on the coordinate variables will be suppressed.

For the purposes of this work, we are interested in the spin-independent OBDM. In order to construct this quantity, we simply sum over the spin degree of freedom and identify the probability of finding a particle (of any spin) in the region d^3r as $\rho(\vec{r})d^3r$.

The OBDM can also be constructed from the single particle HO wavefunctions that make up our single-particle basis space. The OBDM can be expressed as:

$$\rho^{fi}(\vec{r}, \vec{r}') = \sum_{\alpha,\beta} \rho^{fi}_{\alpha\beta} \psi_\alpha(\vec{r}') \psi_\beta(\vec{r}) \tag{2.4}$$

where a Greek subscript, α for example, represents a set of single-particle quantum numbers $(n_\alpha, l_\alpha, j_\alpha, m_\alpha, \tau_{z,\alpha})$. The coefficients, $\rho^{if}_{\alpha\beta}$ are the matrix elements of a space-fixed OBDM and are calculated through:

$$\rho^{fi}_{\alpha\beta} = \langle \Psi_f | a^\dagger_\alpha a_\beta | \Psi_i \rangle. \tag{2.5}$$

It should be noted that the single-particle wavefunction, ψ, is actually a sum of the single-particle wavefunctions defined in Eq. 1.39. In our basis, the particles are defined through the quantum numbers, $(n_\alpha, l_\alpha, j_\alpha, m_\alpha, \tau_{z,\alpha})$, where m_α is the magnetic projection of the total angular momentum quantum number, j_α. The TDHOWF's are defined using the quantum numbers, n, l, m_l. Therefore, one must couple orbital angular momentum (l) and spin (s) into j through:

$$\psi_\alpha(r) = \sum_{m_l, m_s} \langle l_\alpha m_l s_\alpha m_s | j_\alpha m_{j\alpha} \rangle \phi_{n_\alpha l_\alpha m_l} \chi_{s_\alpha m_s} \tag{2.6}$$

The local one-body density in the space-fixed (sf) coordinate system is defined by:

$$\rho^{fi}_{\text{sf}}(\vec{r}) = \sum_{\alpha,\beta} \rho^{fi}_{\alpha\beta} \, \psi^\star_\alpha(\vec{r}) \, \psi_\beta(\vec{r}) \,. \tag{2.7}$$

and is once again normalized to the number of nucleons

$$\int \rho^{fi}_{\text{sf}}(\vec{r}) d^3r = A \,. \tag{2.8}$$

We say that the one-body density is space-fixed (sf) because it includes contributions from the center of mass (cm) motion of the many-body wavefunctions $\Psi(\vec{r}_1 ..... \vec{r}_A)$. This results from our use of single-particle coordinates as opposed to relative coordinates in the nuclear wavefunction. The resulting one-body density distributions will therefore include contributions from the cm motion. However, because of the exact factorization of the cm wavefunction and the translationally-invariant wavefunction, see Eq. (1.34), this density is actually a convolution

of the cm density $\rho_{\text{cm}}^{\Omega}$ and the translationally-invariant (ti) density ρ_{ti}

$$\rho_{\text{sf}}^{\Omega}(\vec{r}_1) \;\;=\;\; \int \rho_{\text{ti}}(\vec{r}_1 - \vec{R})\, \rho_{\text{cm}}^{\Omega}(\vec{R})\, d^3R, \tag{2.9}$$

where we suppress the state labels for simplicity and insert a superscript Ω to signify the dependence on the HO basis space used in the evaluation of the eigenfunctions.

For the HO basis, $\rho_{\text{cm}}^{\Omega}$ is a simple Gaussian (the gs density of H_{cm}) with explicit dependence on Ω that smears out ρ_{ti}. This smearing can obfuscate interesting details of ρ_{ti}. Furthermore, it introduces a spurious dependence on the basis parameter Ω into $\rho_{\text{sf}}^{\Omega}$ that masks the convergence. Even in the limit of a completely converged calculation, the single-particle density $\rho_{\text{sf}}^{\Omega}$ depends on Ω, whereas ρ_{ti} becomes independent of the basis.

In order to eliminate these smearing effects and to help develop a physical intuition for the *ab initio* structure of a nucleus, it would be helpful to see the coordinate space density distributions free of spurious cm motion. This can be achieved by a deconvolution of the cm density and the translationally-invariant density using standard Fourier methods (51):

$$\rho_{\text{ti}}(\vec{r}_1) \;\;=\;\; F^{-1}\!\left[\frac{F[\rho_{\text{sf}}^{\Omega}(\vec{r}_1)]}{F[\rho_{\text{cm}}^{\Omega}(\vec{R})]}\right] \tag{2.10}$$

where $F[f(\vec{r})]$ is the 3-dimensional Fourier transform of $f(\vec{r})$. At convergence, the dependence on Ω should cancel on the RHS of this equation. That means that after this deconvolution, we can better investigate the convergence of the density.

2.2 The OBDM in Operator Notation

In order to perform these Fourier transforms in an analytic and computationally inexpensive manner, we first perform a multipole expansion on the sf one-body density. In order to facilitate this, consider the local density operator (58):

$$\begin{aligned}
\hat{\rho}_{\text{sf}}(\vec{r}) \;\;&=\;\; \sum_{k=1}^{A} \delta^3(\vec{r} - \vec{r}_k) \\
&=\;\; \sum_{k=1}^{A} \frac{\delta(r - r_k)}{r^2} \sum_{lm} Y_l^{\star m}(\hat{r}_k) Y_l^{m}(\hat{r})
\end{aligned} \tag{2.11}$$

where $\hat{r}$ is the unit vector in the direction $\vec{r}$, and $Y_l^m(\hat{r})$ is a spherical harmonic. Note that it

has the property:

$$Y_l^{-m}(\hat{r}) \ = \ (-1)^m Y_l^{\star m}(\hat{r}). \tag{2.12}$$

Inserting this operator into the many body state, $|A\lambda_i J_i M_i\rangle$, where A represents the number

of nucleons, J_i is the total angular momentum, M_i is the angular momentum projection, and

λ_i represents all other quantum numbers, we find:

$$\rho_{sf}(\vec{r}) \ = \ \sum_{Kk} Y_K^{*k}(\hat{r}) \langle A\lambda_f J_f M_f | \sum_{j=1}^{A} \frac{\delta(r-r_j)}{r^2} Y_K^k(\hat{r}_j) | A\lambda_i J_i M_i \rangle, \tag{2.13}$$

which, via the Wigner-Eckert theorem, becomes:

$$\rho_{sf}(\vec{r}) \ = \ (-1)^{J_f - M_f} \begin{pmatrix} J_f & K & J_i \\ -M_f & k & M_i \end{pmatrix}$$

$$\times Y_K^{*k}(\hat{r}) \langle A\lambda_f J_f || \sum_{j=1}^{A} \frac{\delta(r-r_j)}{r^2} Y_K(\hat{r}_j) || A\lambda_i J_i \rangle. \tag{2.14}$$

Note that for a generic operator, T_K, (59):

$$\langle \lambda_f J_f || T_K || \lambda_i J_i \rangle \ = \ \frac{1}{\hat{K}} \sum_{\alpha,\beta} \langle \alpha || T_K || \beta \rangle \langle \lambda_f J_f || (a_\alpha^\dagger \tilde{a}_\beta)^{(K)} || \lambda_i J_i \rangle \tag{2.15}$$

where $\hat{K} = \sqrt{2K+1}$,

$$(a_\alpha^\dagger \tilde{a}_\beta)^{(K)} \ = \ \sum_{m_{j_\alpha}, m_{j_\beta}} (-1)^{j_\beta - m_{j_\beta}} \langle j_\alpha m_{j_\alpha} j_\beta m_{j_\beta} | Kk \rangle a_\alpha^\dagger a_\beta, \tag{2.16}$$

and

$$\tilde{a}_{j,m_j} = (-1)^{j-m_j} a_{j,-m_j}. \tag{2.17}$$

From Eq. 2.15, it follows that the quantity to be calculated is:

$$\langle \alpha || \hat{\rho} || \beta \rangle \ = \ \langle \alpha || \sum_{j=1}^{A} \frac{\delta(r-r_j)}{r^2} || \beta \rangle \langle \alpha || Y_K(\hat{r}_i) || \beta \rangle \tag{2.18}$$

where (50)

$$\langle \alpha || \sum_{j=1}^{A} \frac{\delta(r-r_j)}{r^2} || \beta \rangle \ = \ R_\alpha(r) R_\beta(r) \tag{2.19}$$

$$\langle \alpha || Y_K(\hat{r}_j) || \beta \rangle \ = \ \frac{(-1)^{j_\alpha + 1/2}}{\sqrt{4\pi}} \hat{j}_\alpha \hat{j}_\beta \hat{l}_\alpha \hat{l}_\beta \langle l_\alpha 0 l_\beta 0 | K0 \rangle \begin{Bmatrix} j_\alpha & j_\beta & K \\ l_\beta & l_\alpha & \frac{1}{2} \end{Bmatrix} \tag{2.20}$$

and $R_\alpha(r)$ is the radial component of the TDHOWF, ϕ, given by:

$$R_{nl}(r) = \left[\frac{2(2\nu)^{l+3/2}\Gamma(n+1)}{\Gamma(n+\frac{l}{2}+\frac{3}{2})}\right]^{1/2} e^{-\nu r^2} L_n^{l+\frac{1}{2}}(2\nu r^2)$$

(2.21)

with $L_n^{l+\frac{1}{2}}$ as the associated Laguerre polynomials.

From the above, we arrive at the desired result:

$$\rho_{\text{sf}}(\vec{r}) = \sum_K \frac{\langle JMK0|JM\rangle}{\sqrt{2J+1}} Y_K^{\star 0}(\hat{r})\, \rho_{\text{sf}}^{(K)}(r)$$

(2.22)

where $\rho_{\text{sf}}^{(K)}(r)$ is the Kth multipole of the sf density. For initial and final states with spin J, the multipoles range from $K = 0$ to $K = 2J$. As we will see below, this multipole expansion greatly simplifies the Fourier transforms needed for the deconvolution.

With a HO single-particle basis, each multipole is given by

$$\rho_{\text{sf}}^{(K)}(r) = \sum R_\alpha(r)R_\beta(r)\frac{-1}{\hat{K}}\langle l_\alpha \frac{1}{2} j_\alpha||Y_K||l_\beta \frac{1}{2} j_\beta\rangle$$
$$\times \langle A\lambda J||(a_\alpha^\dagger \tilde{a}_\beta)^{(K)}||A\lambda J\rangle$$

(2.23)

2.3   Deconvolution

As shown in Eq. 2.10, in order to isolate the ti density, we perform a series of Fourier transforms. We use the relation:

$$\int d^3r \exp(i\vec{q}\cdot\vec{r})\,\rho_{\text{sf}}^{(K)}(r)\, i^K Y_K^{\star 0}(\hat{r}) = \tilde{\rho}_{\text{sf}}^{(K)}(q)\, Y_K^{\star 0}(\hat{q})\,,$$

(2.24)

where the multipole component of the density in momentum space is expressed as

$$\tilde{\rho}_{\text{sf}}^{(K)}(q) = 4\pi \int j_K(qr)\, \rho_{\text{sf}}^{(K)}(r)\, r^2 dr$$

(2.25)

with j_K the spherical Bessel Functions of the first kind. Thus, the deconvolution of each multipole gives:

$$\rho_{\text{ti}}^{(K)}(r) = \frac{1}{2\pi^2} \int j_K(qr)\, \frac{\tilde{\rho}_{\text{sf}}^{(K)}(q)}{\tilde{\rho}_{\text{cm}}(q)}\, q^2 dq$$

(2.26)

where,

$$\tilde{\rho}_{\text{cm}}(q) = \frac{\tilde{\rho}_{\text{cm}}^{(0)}(q)}{2\sqrt{\pi}} \tag{2.27}$$

$$= \frac{8\sqrt{2}}{\sqrt{\pi}} \nu^{3/2} \int_0^\infty \frac{e^{-2\nu R^2} \sin(qR)}{qR} R^2 dR$$

For spherically symmetric nuclei, this deconvolution simplifies even further because we only have one term in the multipole expansion, $K = 0$

$$\rho_{\text{ti}}^{(0)}(r) = \frac{1}{2\pi^2} \int_0^\infty \frac{\sin(qr)}{qr} \frac{\tilde{\rho}_{\text{sf}}^{(0)}(q)}{\tilde{\rho}_{\text{cm}}(q)} q^2 dq, \tag{2.28}$$

and the 3-dimensional ti density is simply,

$$\rho_{\text{ti}}(\vec{r}) = \frac{\rho_{\text{ti}}^{(0)}(r)}{2\sqrt{\pi}} \tag{2.29}$$

without any angular dependence.

Another advantage of the multipole expansion is that it allows for a straightforward calculation of the (sf or ti) density for any magnetic projection M, once the multipoles $\rho^{(K)}(r)$ are known. The multipoles $\rho^{(K)}(r)$ are completely determined from reduced matrix elements, which do not depend on M. The only dependence of $\rho_{\text{sf}}(\vec{r})$ on M is entirely through the explicitly M-dependent Clebsch–Gordan coefficients in Eq. (2.22).

2.4 Observables

The OBDM can be used to calculate any one-body observable. A complete set of static and one-body transition matrix elements can be used to calculate a two-body observable. In this section, formulae to calculate various observables using the OBDM or one-body density distribution (OBDD) are presented.

2.4.1 Electromagnetic Observables

To leading order, the electric multipole moment is given by:

$$\hat{q}_K^k = \int \rho_p(\vec{r}) r^K Y_K^k d^3 r \tag{2.30}$$

where ρ_p represents the one-body proton density distribution and K represents the degree of the multipole radiation. Mass instead of charge observables can also be calculated for the neutron OBDDs using similar equations,i.e., replacing ρ_p with ρ_n would give the expression for the mass quadrupole moment rather than the electric quadrupole moment. The reduced transition rate is:

$$B(E,K) = \sum_{k,M_f} |\langle A\lambda_f J_f M_f| \int \rho_p(\vec{r}) r^K Y_K^k d^3 r |A\lambda_f J_i M_i\rangle|^2 \qquad (2.31)$$

The fact that $\rho(r) r^K Y_K^k$ is an irreducible tensor of degree K leads to the necessary condition that $|J_f - J_i| \le K \le J_f + J_i$ in order for $B(E,K)$ to be non-vanishing. Using our definition for ρ, as well as the Condon-Shortley phase convention, one can see that (50):

$$B(E,K) = \sum_{k,M_f} \langle A\lambda_f J_f M_f| \sum_j r_j^K Y_K^k(\hat{r}_j)|A\lambda_f J_i M_i\rangle^2 \qquad (2.32)$$

$$(2.33)$$

Where the sum is over the protons. Utilizing the Wigner-Eckert Theorem leads us to(50):

$$B(E,K) = \frac{1}{2J_i+1} |\langle A\lambda_f J_f \parallel \hat{Q}_K \parallel A\lambda_f J_i\rangle|^2 \qquad (2.34)$$

$$\hat{Q}_K^k = \sum_{\alpha,\beta} \langle \alpha|\hat{q}_\lambda^\mu|\beta\rangle a_\alpha^\dagger a_\beta \qquad (2.35)$$

Once we have obtained the one-body density matrix elements $\rho_{\alpha\beta}$ (OBDMEs), we can easily calculate observables that can be expressed as one-body operators. For initial and final states with total angular momentum $J_{i,f}$ and possibly additional quantum numbers $\lambda_{i,f}$, but with the same magnetic projection M, the matrix elements using the canonical one-body electromagnetic current operator E2 are given by

$$
\begin{aligned}
M_{\text{E2}}^{if} &= \langle \lambda_f J_f M|\text{E2}|\lambda_i J_i M\rangle \\
&= \sum_{\alpha\beta} \rho_{\alpha\beta}^{fi} \langle \alpha| \int r^2 Y_2^0(\hat{r}) d^3 r |\beta\rangle , \qquad (2.36)
\end{aligned}
$$

with α and β restricted to the protons only ($\tau_z = \frac{1}{2}$). The fact that the OBDM includes cm motion does not matter for E2 matrix elements (nor for M1 matrix elements discussed below):

the cm wavefunction is an *s*-wave, and does not contribute to the integral due to the factor $Y_2^0(\hat{r})$.

For comparison with experiments, it is more convenient to convert these M-dependent matrix elements to reduced matrix elements using the Wigner–Eckart theorem (50). For a proper tensor operator T_{Kk}, the reduced matrix element is defined by:

$$
\begin{aligned}
\langle \lambda_f J_f || T_K || \lambda_i J_i \rangle &= \langle \lambda_f J_f M_f | T_{Kk} | \lambda_i J_i M_i \rangle \\
&\times \frac{\sqrt{2J_f + 1}}{\langle J_f M_f K k | J_i M_i \rangle}
\end{aligned}
\tag{2.37}
$$

provided that the Clebsch–Gordan coefficient in the denominator, $\langle J_f M_f K k | J_i M_i \rangle$ (following the conventions of Ref. (50)), is not zero. In terms of the reduced E2 matrix elements, reduced E2 transition rates are given by (60):

$$
\mathrm{B(E2}; i \to f) = \frac{1}{2J_i + 1} \langle \lambda_f J_f || \ \mathrm{E2} \ || \lambda_i J_i \rangle^2
\tag{2.38}
$$

in units $\mathrm{e}^2 \ \mathrm{fm}^4$. The quadrupole moment is conventionally defined through the E2 matrix element for $M = J$:

$$
\mathcal{Q} = \left(\frac{16\pi}{5} \right)^{1/2} \langle \lambda J M = J | \ \mathrm{E2} \ | \lambda J M = J \rangle
\tag{2.39}
$$

and can also be expressed in terms of the reduced matrix element as (60):

$$
\mathcal{Q} = \left(\frac{16\pi}{5} \right)^{1/2} \frac{1}{\hat{J}} \langle J J 2 0 | J J \rangle \langle \lambda J || \ \mathrm{E2} \ || \lambda J \rangle
\tag{2.40}
$$

in units $\mathrm{e} \ \mathrm{fm}^2$.

The matrix elements for the M1 transitions and magnetic moments receive contributions both from the proton and neutron intrinsic spins and from the proton orbital motion. Again, we consider only the canonical one-body electromagnetic current operator, in which case they can be calculated from the OBDMEs:

$$
\begin{aligned}
M_{\mathrm{M1}}^{fi} &= \langle \lambda_f J_f M | \mathrm{M1} | \lambda_i J_i M \rangle \\
&= \sum_{\alpha\beta} \rho_{\alpha\beta}^{fi} \ \langle \alpha | \frac{1}{2}(1 + \tau_z)(L + g_p \sigma) + \frac{1}{2}(1 - \tau_z) g_n \sigma | \beta \rangle
\end{aligned}
$$

where $g_p = 5.586$ and $g_n = -3.826$ are the proton and neutron gyromagnetic ratios in nuclear magneton (μ_N) units; the quantities L, σ and τ represent the conventional orbital angular

momentum, spin and isospin operators. In terms of the reduced M1 matrix element, the M1 transition rates are given as (60)

$$B(M1; i \rightarrow f) \quad = \quad \frac{1}{2J_i + 1}\langle \lambda_f J_f || \text{ M1 } ||\lambda_i J_i \rangle^2 \tag{2.41}$$

in units μ_N^2, and the magnetic moment is defined as,

$$\mu \quad = \quad \left(\frac{4\pi}{3}\right)^{1/2} \langle \lambda J || \text{ M1 } ||\lambda J \rangle \tag{2.42}$$

in units μ_N.

2.4.2   Gamow-Teller Transitions

The Gamow-Teller (GT) matrix element (M_{GT}) also is not affected by the cm contribution to the one-body density. M_{GT} is related to the OBDM through the relation:

$$\langle J_f | M_{GT} | J_i \rangle \quad = \quad \sum_{\alpha\beta} \rho_{\alpha\beta} \langle \alpha | \hat{M}_{GT} | \beta \rangle \tag{2.43}$$

where $\hat{M}_{GT} = \sigma_z \tau_-$. In order to obtain the single-particle expectation value, we proceed as follows:

$$\langle \alpha | \hat{M}_{GT} | \beta \rangle \quad = \quad \langle j_\alpha m_\alpha \lambda_\alpha | P \hat{M}_{GT} P | j_\beta m_\beta \lambda_\beta \rangle \tag{2.44}$$

where λ is restricted to the quantum numbers n, l. P is the parity operator which performs a parity transformation (inversion). In three dimensions, this simply flips the sign of the spatial coordinates. We say that a function is symmetric under the parity transformation when, for a generic function $f(x)$, $f(-x) = f(x)$, and antisymmetric if $f(-x) = -f(x)$. As our code, MFDn, works on one nucleus at a time, we assume that isospin is a good quantum number and one of the nuclear states can be considered an isobaric analogue of the parent transition nucleus. We therefore neglect the isospin lowering operator and our calculation relies solely on the spin operator, σ_z. It would be impractical to read in wavefunctions from previously calculated nuclei as I/O operations can be a major bottleneck in massively parallel calculations. Note that:

$$\langle j_\alpha m_\alpha \lambda_\alpha | P \hat{M}_{GT} P | j_\beta m_\beta \lambda_\beta \rangle \quad = \quad \delta_{\lambda_\alpha \lambda_\beta} \langle j_\alpha m_\alpha | P \hat{M}_{GT} P | j_\beta m_\beta \rangle \tag{2.45}$$

where,

$$|jm\rangle \;=\; \sum_{m_l m_s} \langle l m_l s m_s | jm \rangle |l m_l \rangle |s m_s \rangle. \tag{2.46}$$

We now see that: and hence,

$$\langle J_f | \hat{M}_{GT} | J_i \rangle \;=\; \sum_{\alpha\beta} \rho_{\alpha\beta} \delta_{\lambda_\alpha \lambda_\beta} \sum_{m_l m_s} \langle l m_l s m_s | jm \rangle^2 m_s. \tag{2.47}$$

2.4.3 RMS radius

The radii calculated by MFDn are heavily influenced by the cm component of the one-body density. In order to calculate the most realistic RMS radius from the OBDD, the ti component must first be isolated. There are approximate corrections that can be made, however, if one is unable to perform the deconvolution.

The RMS radius is related to the OBDD through the relation:

$$\langle r^2 \rangle^{1/2} \;=\; \left[\frac{\int \rho_{ti}(\vec{r}) r^2 d^3 r}{\int \rho_{ti}(\vec{r}) d^3 r} \right]^{1/2} \tag{2.48}$$

and can be related to the sf OBDD through (61):

$$\left[\frac{\int \rho_{ti}(\vec{r}) r^2 d^3 r}{\int \rho_{ti}(\vec{r}) d^3 r} \right]^{1/2} \;=\; \left[\frac{\int \rho_{sf}(\vec{r}) r^2 d^3 r}{\int \rho_{sf}(\vec{r}) d^3 r} - \frac{3b^2}{2A} \right]^{1/2} \tag{2.49}$$

where,

$$b \;=\; \frac{\hbar c}{\sqrt{\hbar \Omega m c^2}} \tag{2.50}$$

CHAPTER 3.   Non-Density Results

3.1   GS Energy and Excitation Spectra

The gs energies of the Li isotopes as a function of the HO energy, $\hbar\Omega$, are shown at a sequence of N_{max} values in Fig. 3.1. We also provide the extrapolated gs energy as a function of $\hbar\Omega$, as described above. Our results with JISP16 for selected spectral and other observables of ^{6}Li,^{7}Li, and ^{8}Li are summarized in Tables 3.1, 3.2, and 3.3 and compared with experiment when available.

The gs energy for ^{6}Li is rapidly converging as indicated by the emerging independence of the two basis parameters ($N_{\max}$, $\hbar\Omega$). The convergence is most rapid around $\hbar\Omega = 17.5$ to 20 MeV, where the variational upper bound on the energy is minimal. Our extrapolated gs energy (2) shows that the system is underbound by 0.50 MeV. Excitation energies are well converged at higher $N_{\max}$ (12 and above) values, at least for 3^+ and 0^+ states. Note that these states are narrow resonances: the experimental width of the 3^+ is 24 keV and the width of the first excited 0^+ is 8 eV.

The excitation energy of the first 2^+ state, shown in Fig. 3.2 is much less converged, and shows a systematic increase with increasing $\hbar\Omega$. Such $\hbar\Omega$-dependence of the excitation energy is typical for wide resonances as observed in comparisons of NCSM results with inverse scattering analysis of α-nucleon scattering states (62; 1). In light of these previous analyses, the significant $\hbar\Omega$-dependence seems commensurate with the large experimental width of 1.3 MeV for this 2^+ state.

The gs energy for ^{7}Li converges much the same as the gs energy for ^{6}Li. Once again, the variational upper bound on the energy is minimized between $\hbar\Omega$ values of 17.5 and 20 MeV. From Table 3.2 we see that the gs energy is underbound by about 0.67 MeV. The gs energy
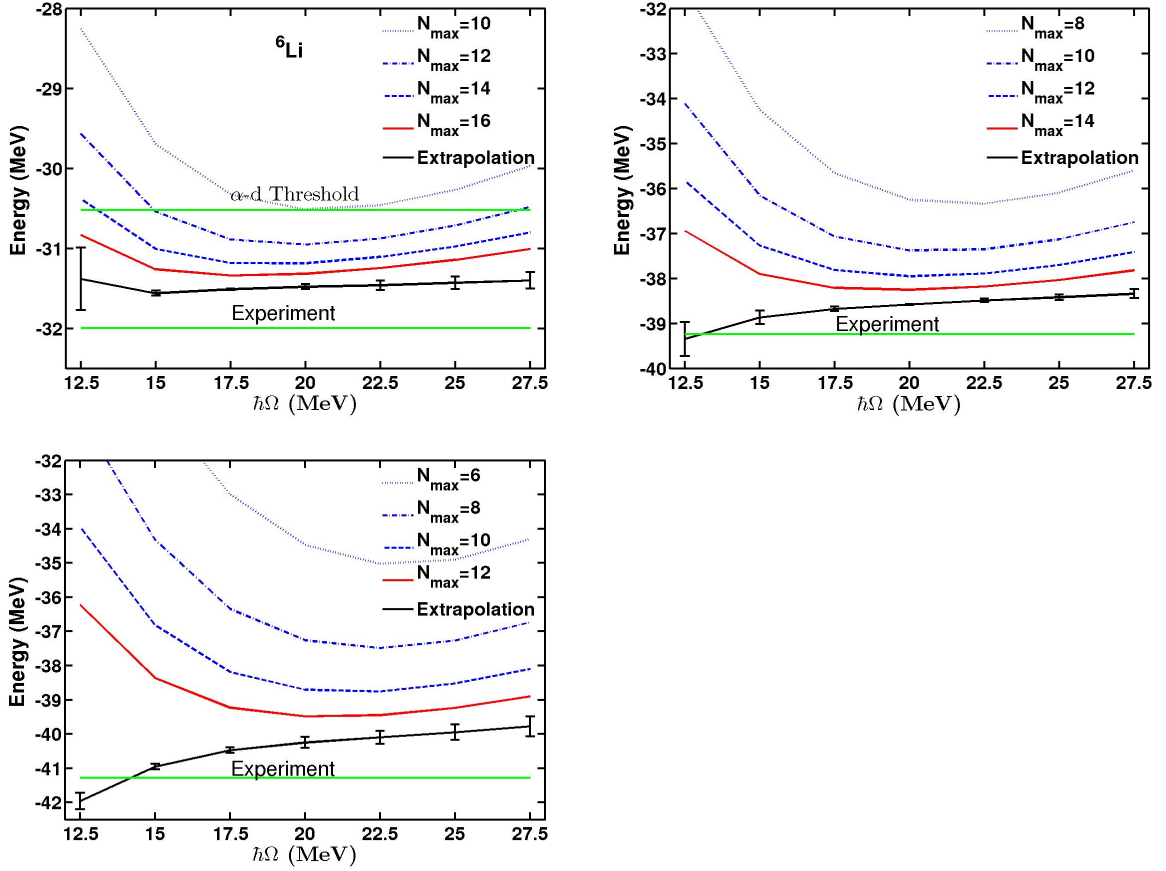
Figure 3.1   The gs energy of ^{6}Li, ^{7}Li, and ^{8}Li for a sequence of N_{max} values (indicated in the legends) as a function of the HO energy. The extrapolated gs energy is shown at specific values of $\hbar\Omega$ with undertainties (defined in the text) indicated as error bars.

and excitation energies compare favorably to other methods and interactions (63; 64).

We evaluated the low-lying states in basis spaces up to $N_{\max} = 14$. We only consider isospin $\frac{1}{2}$ states – the lowest isospin $\frac{3}{2}$ has more than 10 MeV excitation energy. The lowest five states in the excitation energy spectrum compare well with experiment and the correct level ordering is preserved as shown in Fig. 3.2. The excitation energy of four of these five states shows rapid numerical convergence with $N_{\max}$ and stability with respect to variations in the HO energy. However, the convergence of the lower of the two $\frac{5}{2}^-$ states is significantly slower. Indeed, experimentally this state has a large width of 0.88 MeV, whereas the width of the other states is less than 0.1 MeV. Thus, as in ^{6}Li, we again observe a good correlation between experimental width and convergence rate of excitation energies.
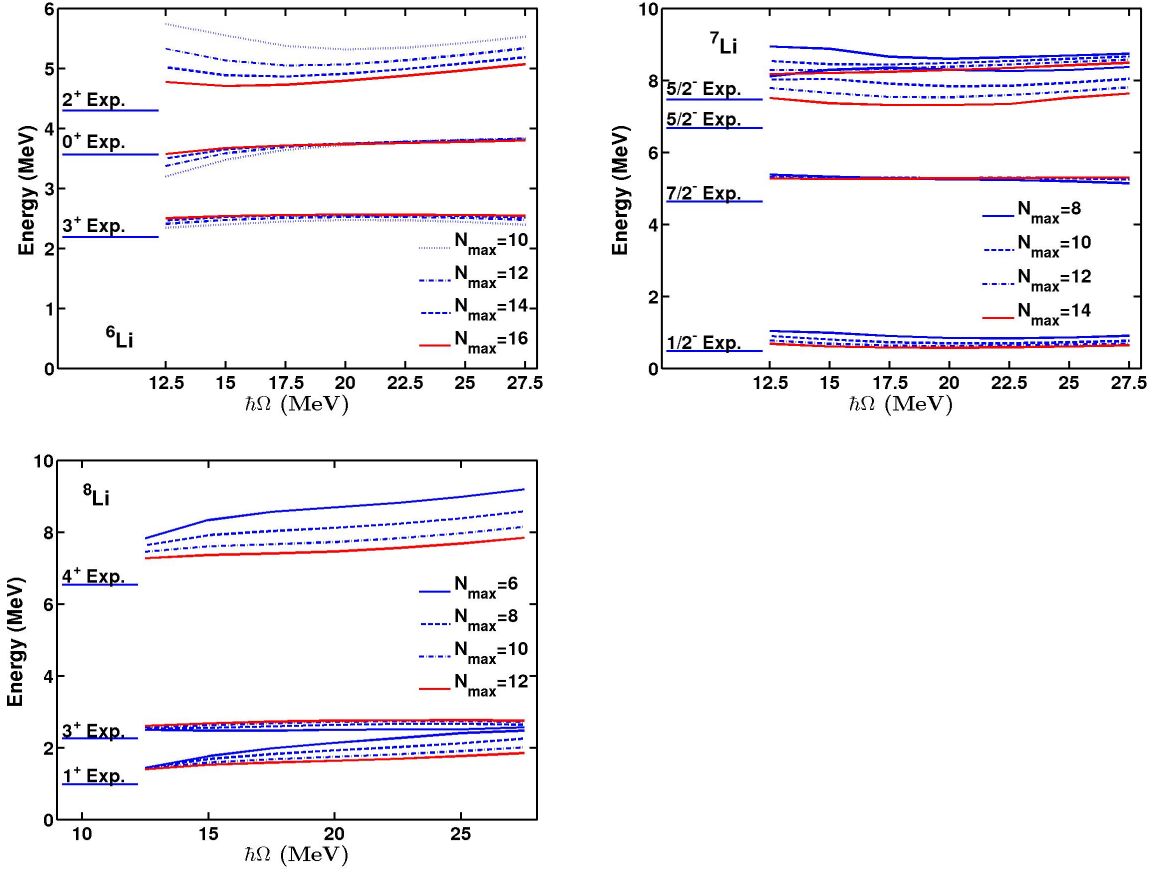
Figure 3.2   The excitation spectra of ^{6}Li, ^{7}Li, and ^{8}Li for a sequence of N_{max} values (indicated in the legends) as a function of the HO energy.

The gs energy for ^{8}Li converges much the same as the gs energies previously shown. The variational upper bound on the energy is minimized between $\hbar\Omega$ values of 20.0 and 22.5 MeV, slightly higher than the ligher isotopes. From Table 3.3 we see that the gs energy is underbound by about 1.0 MeV.

In addition to the gs, we examined several narrow low-lying states: the lowest two excited states, which are narrow states, with a width of 33 keV or less, as well as a narrow low-lying 4^+ state at 6.53 MeV with a width of 35 keV. We do not consider isospin 2 states – the lowest isospin 2 has more than 10 MeV excitation energy. The excitation energies obtained with JISP16 compare reasonably well with the experimental excitation energies, though the level splittings are a bit too large (see Fig. 3.2). The convergence of the spectrum is similar as for the other Li-isotopes, though the convergence of the 4^+ state is somewhat slower than expected

based on its small width. In our calculations there are several additional states below this 4^+ state, which is typically the 8th state in our calculated spectrum, depending on the basis space; experimentally, it is the 7th observed state.

Both the gs binding energy and the excitation energies calculated with JISP16 compare favorably to those calculated with alternative realistic NN interactions, i.e. Argonne V18, CD-Bonn, INOY, and SRG evolved N3LO interactions (63; 65; 66; 67). However, with the addition of appropriate three-body interactions, such as Illinois-2 (63; 75) or chiral three-body forces (68; 69; 70), one can obtain somewhat better agreement with data than with the NN-only interaction JISP16.

3.2   Radii

In Fig. 3.3, we show the dependence of the RMS point-proton radius on the basis space parameters $N_{\max}$ and $\hbar\Omega$ for ^{6}Li. It appears that this radius is converging less rapidly than the gs and excitation energies. Furthermore, the convergence is neither monotonic nor uniform: at small values of the HO energy the radius tends to decrease with increasing $N_{\max}$, whereas at larger values of $\hbar\Omega$ the radius increases with increasing $N_{\max}$; around $\hbar\Omega = 10$ to 12.5 MeV the RMS radius is nearly independent of $N_{\max}$. Because of this, it is difficult to make realistic estimates of uncertainties for radii and other long-range observables such as quadrupole moments which exhibit similar patterns.

The convergence patterns shown in Fig. 3.3 may be understood from the following observation: since the HO wavefunctions fall off like a Gaussian, e^{-cr^2} while the true nuclear wavefunction falls off like an exponential, e^{-dr}, observables whose calculations are weighted towards the tail of the wavefunction, such as the RMS radius, will converge slower than those observables that depend less on the tails, such as the energy and the magnetic moment (see below). Furthermore, it is well known that the RMS radius, and also other long-range operators such as the quadrupole moment, are minimally affected by the short-range correlations (71; 67). And the value of $\hbar\Omega$ that minimizes the gs energy is not necessarily the value of $\hbar\Omega$ that best represents the long-range behavior of the wavefunction.

In Fig. 3.4 we show the radial density distribution for two sets of finite basis spaces, with
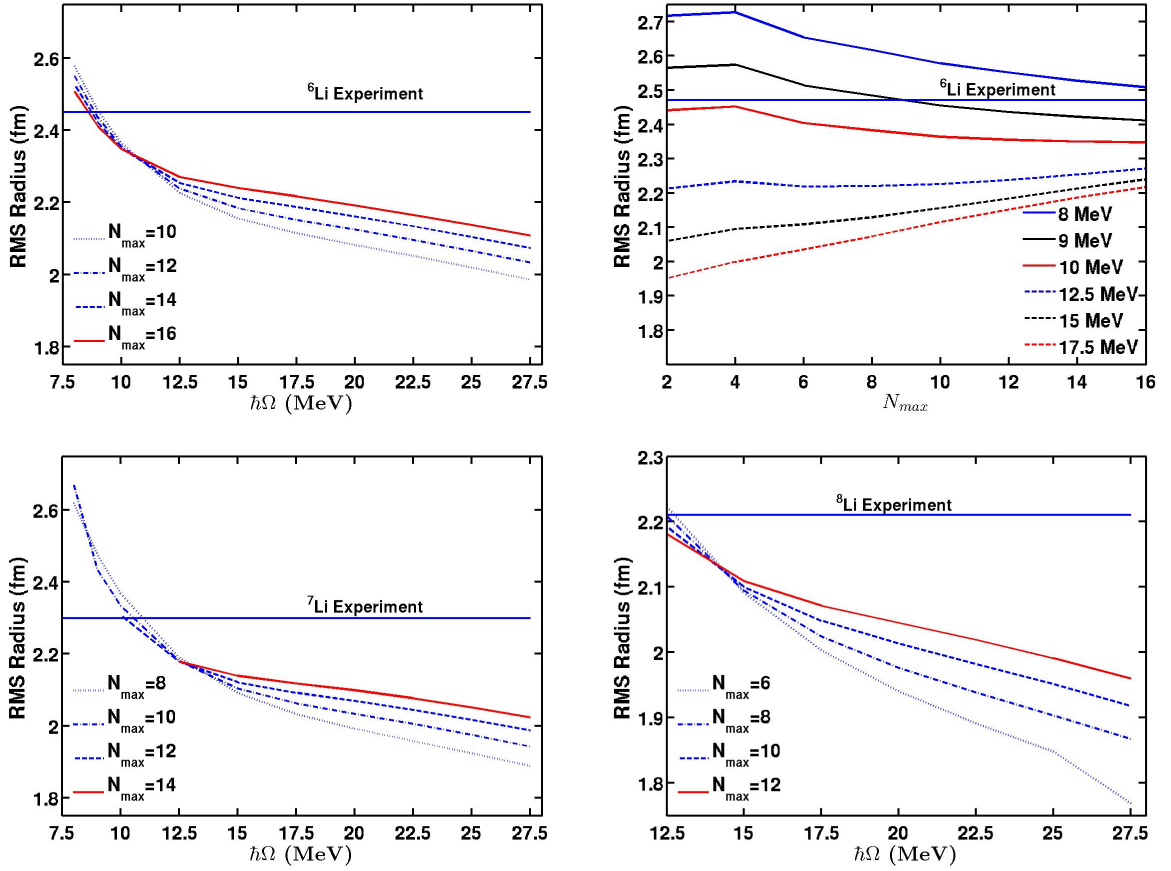
Figure 3.3   The RMS point-proton radius of the gs of ^{6}Li as a function of HO energy at various $N_{\max}$ values (top left) and as function of $N_{\max}$ at various values of the HO energy (bottom). The RMS point-proton radius of the gs of ^{7}Li and ^{8}Li as a function of HO energy at various $N_{\max}$ values are also shown (bottom left and right, respectively)

$\hbar\Omega = 10$ and 17.5 MeV respectively. The lower panel shows that the exponential tail is much better represented in a HO basis with $\hbar\Omega = 10$ than in a HO basis with 17.5 MeV, and that the long-range behavior of the one-body density is therefore converging much more rapidly in a HO basis with $\hbar\Omega = 10$, and rather poorly converging in the HO basis that minimizes the gs energy. That is, the radial density calculated with $\hbar\Omega = 10$ MeV shows much more consistent long-range behavior at the three highest $N_{\max}$ values than the density calculated with $\hbar\Omega = 17.5$ MeV. This leads us to the conclusion that while the value of $\hbar\Omega$ that minimizes the gs energy is an appropriate value when calculating gs and excitation energies, as well as magnetic observables, this value is not appropriate for calculations of observables that depend
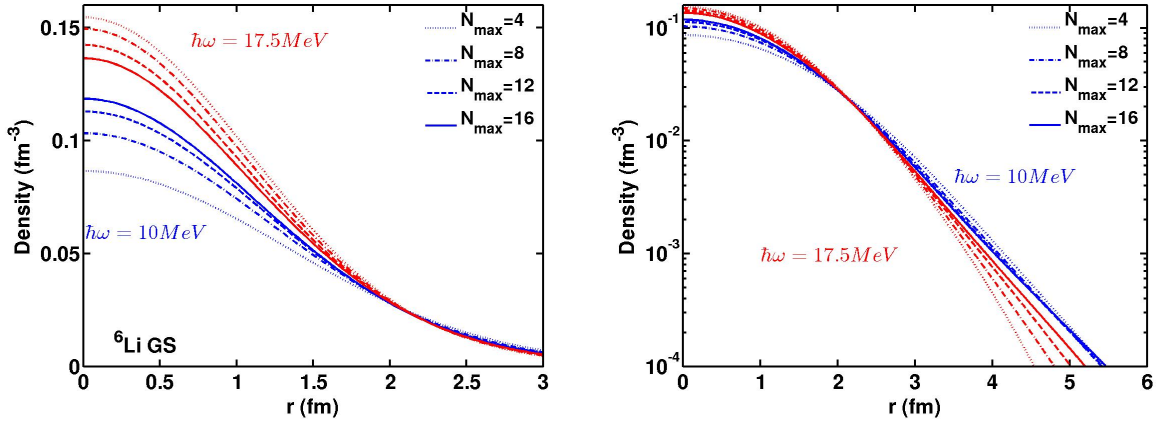
Figure 3.4   The angle-averaged density of the ^{6}Li gs for various $N_{\max}$ values at $\hbar\Omega = 10$ and 17.5 on a linear (left) and semi-logarithmic (right) scale.

primarily on long-range correlations, even in the moderately large basis spaces considered here.

There is no a-priori reason why any two observables should converge with the same pattern in the basis space parameters (Nmax, hw). Hence we seek the optimal (Nmax, hw) values for each observable. We we will quote results for long-range observables at the $\hbar\Omega$ value where the RMS radii for various $N_{\max}$ values intersect as seen in the top portion of Fig. 3.3, rather than at the $\hbar\Omega$ value that minimizes the gs energy. To be specific, for the Li-isotopes under discussion here, we simply take the results at $\hbar\Omega = 10$ to 12.5 MeV (where the $N_{\max}$ dependence appears to be minimal) as our approximation to the converged value of the RMS radius. In a similar fashion, we will cite results for the region of minimal $N_{\max}$ dependence for other observables that depend primarily on long-range correlations. Such observables include RMS radii, E2 moments, and B(E2) transitions. Robust extrapolations to the infinite basis space and reliable error estimates for these observables remain an open question. Density distributions will be discussed in more detail in subsequent chapters.

In order to convert measured nuclear charge radii, $\langle r_c^2 \rangle^{1/2}$, to point-proton radii, we use (72)

$$\langle r_{pp}^2 \rangle \quad = \quad \langle r_c^2 \rangle - R_p^2 - \frac{N}{Z} R_n^2 - \frac{3\hbar^2}{4M_p^2 c^2} \tag{3.1}$$

Here, $R_p^2 = 0.769(12)$ fm^2 is the RMS proton charge radius, $R_n^2 = -0.177(4)$ fm^2 the RMS neutron charge radius, M_p the proton mass, $\langle r_c^2 \rangle_{so}$ the spin-orbit charge density, and $\frac{3\hbar^2}{4M_p^2 c^2} \approx 0.033$ fm^2 the Darwin–Foldy correction. In addition to these correction terms there is also a

spin-orbit contribution to the charge radius, but this contrubution is model-dependent, and (for the nuclei discussed here) less than 1% for realistic wavefunctions (73). For the experimental radii we use the values of Ref. (73), which were obtained from high-precision laser spectroscopy measurements of isotope shifts in combination with the ^{6}Li charge radius as absolute reference. Using the ^{7}Li charge radius as reference in combination with the same isotope shifts gives radii that are about 2% to 3% smaller than the ones we have listed in the tables below (74).

The RMS point proton radii for ^{7}Li and ^{8}Li show similar convergence properties to that of ^{6}Li. The obtained RMS point-proton radii are similar to those obtained with CD-Bonn; both CD-Bonn and JISP16 give results that are about 10% too small compared to experiment. INOY (65) gives an even smaller radius, whereas AV18 plus Illinois-2 leads to a radius (75) that is closer to the experimental value for the isotopes examined in this work.

3.3 Electromagnetic Observables

Fig. 3.5 displays the magnetic dipole moments and magnetic dipole transition rates to the gs for selected states of ^{6}Li, ^{7}Li, and ^{8}Li. These observables converge quickly, and for calculations at $N_{\mathrm{max}} = 12$, are almost independent the HO energy. In fact, most of the magnetic observables are already reasonably well converged (to within 10%) at $N_{\mathrm{max}} = 8$, with the noticable exception of the two $\frac{5}{2}^-$ excited states of ^7Li. This is partially due to a strong state mixing between these two states. We require larger basis spaces to fully differentiate these states, because they are close together in energy, and their quantum numbers are identical.

Our estimate for the infinite basis space results for magnetic dipole observables is based on the residual dependence on N_{max} and $\hbar\Omega$ over a 10 MeV window in $\hbar\Omega$. This window does include the optimal $\hbar\Omega$ for the extrapolations and the variational upperbound, but is not necessarily centered around these values. Our numerical error estimate is the RMS sum of the variation with $\hbar\Omega$ over this window and the difference between the results in the two largests N_{max} calculations (rounded up), i.e. treating the variation with each of the two basis space parameters as independent sources of numerical uncertainties.

With JISP16, the magnetic moments of the gs of ^{6}Li and ^{7}Li is about 2% and 10% too low respectively. This could easily arise from our neglect of meson-exchange currents in our current

calculations. GFMC calculations with AV18 plus Illinois-2 three-body forces (76) found that the magnetic moment of the ^{7}Li gs receives a 10% correction from meson-exchange currents, changing the magnetic moment from 2.9 μ_N to 3.2 μ_N. It is quite remarkable that our result for the magnetic moment, with the naive pointlike M1 operator, is in fact quite close to the obtained with CD-Bonn, with INOY, and with AV18 plus Illinois-2, all about 10% below the experimental datum. (Note that the exchange current correction to the ^{6}Li gs magnetic moment was only 2% in Ref. (76).)

The B(M1) from the first excited state to the gs is about 20% too low compared to experiment for ^{7}Li. The transition from the second excited state to the gs of ^{6}Li is approximately 8% lower than experiment. Again, this is in qualitative agreement with the findings of Ref. (76): with AV18 plus Illinois-2 there is about 10% increase in the M1 transition matrix element due meson-exchange currents, which results in a 20% increase in the corresponding B(M1).

The convergence properties of the calculated magnetic dipole observables of ^{8}Li are similar to those for ^{6}Li and ^{7}Li discussed above. Because we can only go up to $N_{\max} = 12$, the numerical error estimates are slightly larger than for ^{6}Li and ^{7}Li. The gs magnetic moment is approximately 20% lower than experiment. This seems reasonable, in light of our discussions of magnetic moments above, that this discrepancy is at least partially due to the fact that we do not incorporate meson-exchange currents. Note that CD-Bonn gives a similar magnetic moment as JISP16, but that INOY provides a moment that is slightly closer to experiment, and AV18/IL2 gives a magnetic moment in excellent agreement with data; however, the effect of meson-exchange currents is unclear for this nucleus. The B(M1) transition rates from the 1^+ and 3^+ to the gs are 20% and 50% lower than experiment, but the experimental error bars are large. The magnetic moment of the 4^+ state is remarkably well converged, despite its excitation energy not being very well converged.

Proton and neutron E2 moments for ^{6}Li, ^{7}Li, and ^{8}Li are shown in 3.6; B(E2) transitions are shown in 3.7. Issues relating to the convergence properties of the E2 moments or B(E2) transitions and their associated extrapolations have been discussed above.

In the case of ^{6}Li, the electric quadrupole moment of the gs is actually quite well converged, and in excellent agreement with the experimental value - perhaps better than might be expected

due to basis space limitations and long-range nature of the quadrupole moment operator. The transition rates do not fare nearly so well in this case. The transition from the first excited state to the gs differs from experiment by about 40 %, while the transition from the third excited state to the gs differs by approximately 70 %.

The electric quadrupole moment of the gs of ^{7}Li differs from experiment by about 20 %. The B(E2) transition rate from the first excited state to the ground state differs by about 33 %. For this isotope, it is plain to see that the NNN interactions (AV18/IL2) perform significantly better than JISP16 (an NN interaction) (77; 63; 75).

The electric quadrupole moment of the gs of ^{8}Li differs from experiment by about 20 %. There is no experimental data available for comparison for the B(E2) transition rates. Once again, we see that the NNN interaction performs significantly better than JISP16. Other NN interaction data is not available at the time of this publication. It appears that while convergence rates may have a significant effect on RMS radii, their effect is much more difficult to quantify here. For the radii, we chose a HO energy ($\hbar\Omega$) at which the observable's dependence on N_{max} was minimized. This gave values for the radii that were relatively close to experiment and compared well to alternative interactions. For the case of the E2 moment or its related transition, this strategy worked well in the case of ^{6}Li, but much less so for ^{7}Li and ^{8}Li. For these cases, the use of a NNN interaction seems to make a larger difference.

3.4 Gamow-Teller Transitions

The $(0^+, 1)$ excited state of ^{6}Li is the isobaric analog of the ground state of ^{6}He, and can be used to calculate the Gamow–Teller transition between ^{6}Li and ^{6}He. Assuming isospin symmetry, the Gamow–Teller matrix element M_{GT} is to good approximation given by

$$M_{\mathrm{GT}} = \sum_{\alpha,\beta} \rho_{\alpha\beta}^{if} \langle\alpha|\sigma\tau_+|\beta\rangle \tag{3.2}$$

and is related to the half-life (78) through

$$|M_{\mathrm{GT}}|^2 = \frac{1}{\frac{f_A}{f_V}g_A^2} \frac{2\pi^3 \ln 2/(G^2|V_{ud}|^2)}{(fT_{1/2})_t m_e^5} \tag{3.3}$$

where $g_A = 1.2695(29)$ is the axial constant, $\frac{f_A}{f_V} = 1.00529$ accounts for the difference in the statistical rate function of the vector and axial-vector transitions, m_e is the mass of the electron, $G = 1.166371(6) \cdot 10^{-11} \mathrm{MeV}^{-2}$ is the Fermi coupling constant, and $V_{ud} = 0.9738(4)$ is the CKM matrix element that mixes the quarks involved in the decay. Our M_{GT} result, presented in Table 3.1, compares quite well to that calculated in (78) using the hyperspherical-harmonic expansion method with the same (JISP16) interaction; they also obtained a value of $M_{\mathrm{GT}} = 2.227$. It is interesting to note that Ref. (78) found the exchange current corrections to the GT matrix element to be of the order of a few percent.
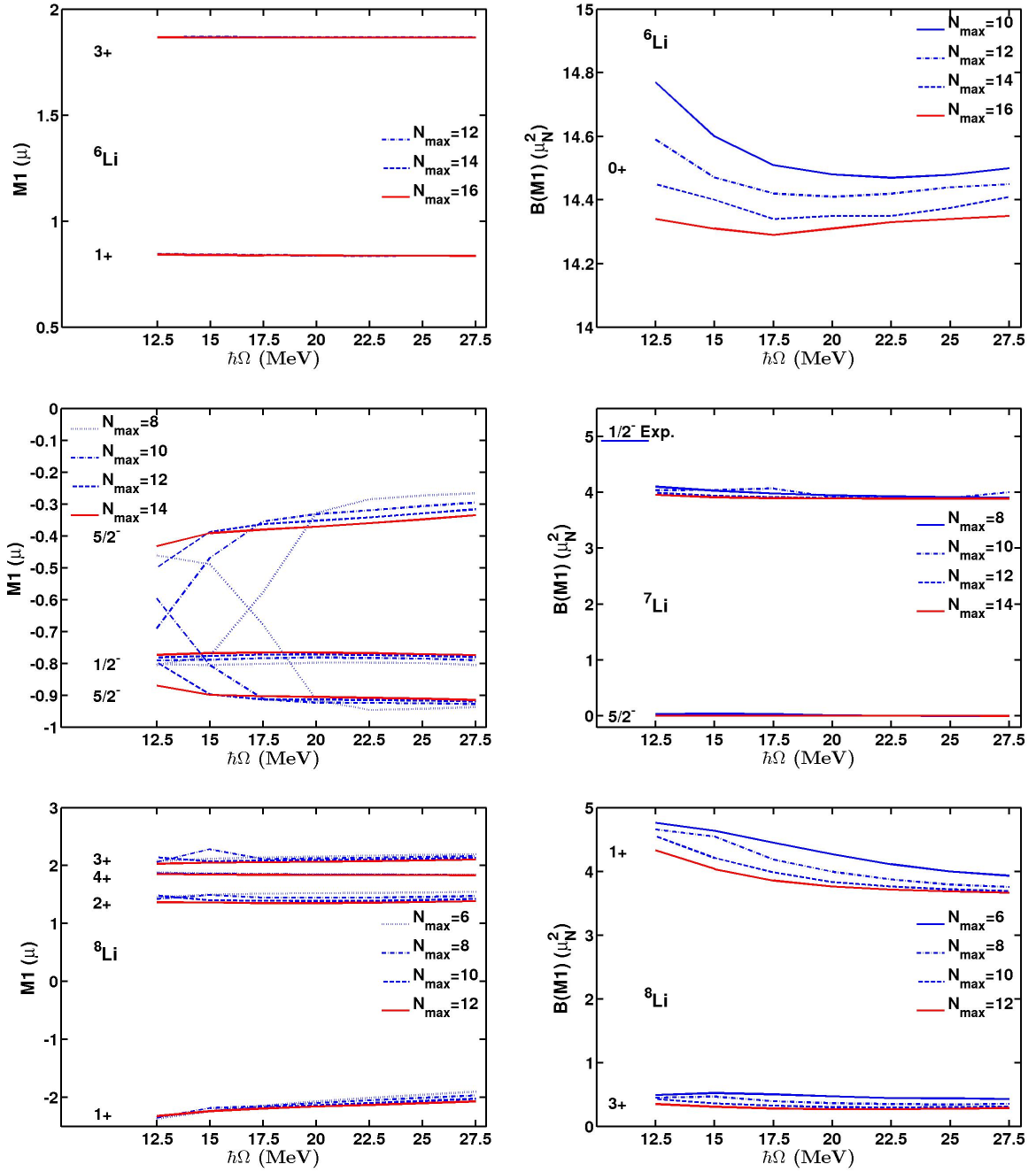
Figure 3.5   The M1 moments (left) and B(M1) transitions (right) are shown at various $N_{\max}$ values as a function of the HO energy for ^{6}Li, ^{7}Li, and ^{8}Li (top to bottom).

Figure 3.6   The E2 neutron moments (left) proton moments (right) are shown at various N_{max} values as a function of the HO energy for ^{6}Li, ^{7}Li, and ^{8}Li (top to bottom). Note that the E2 moments for neutrons are matter quardupole moments.
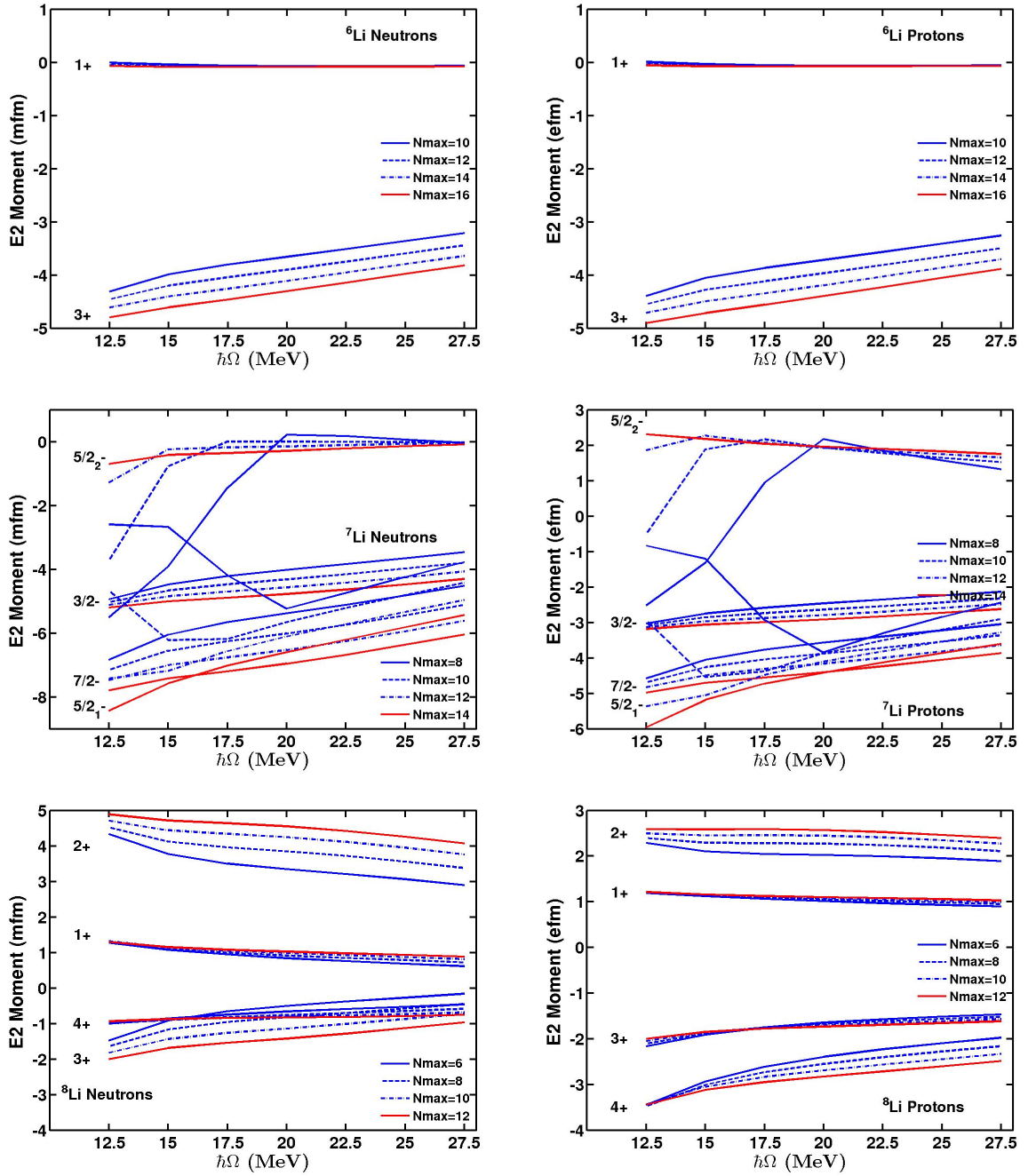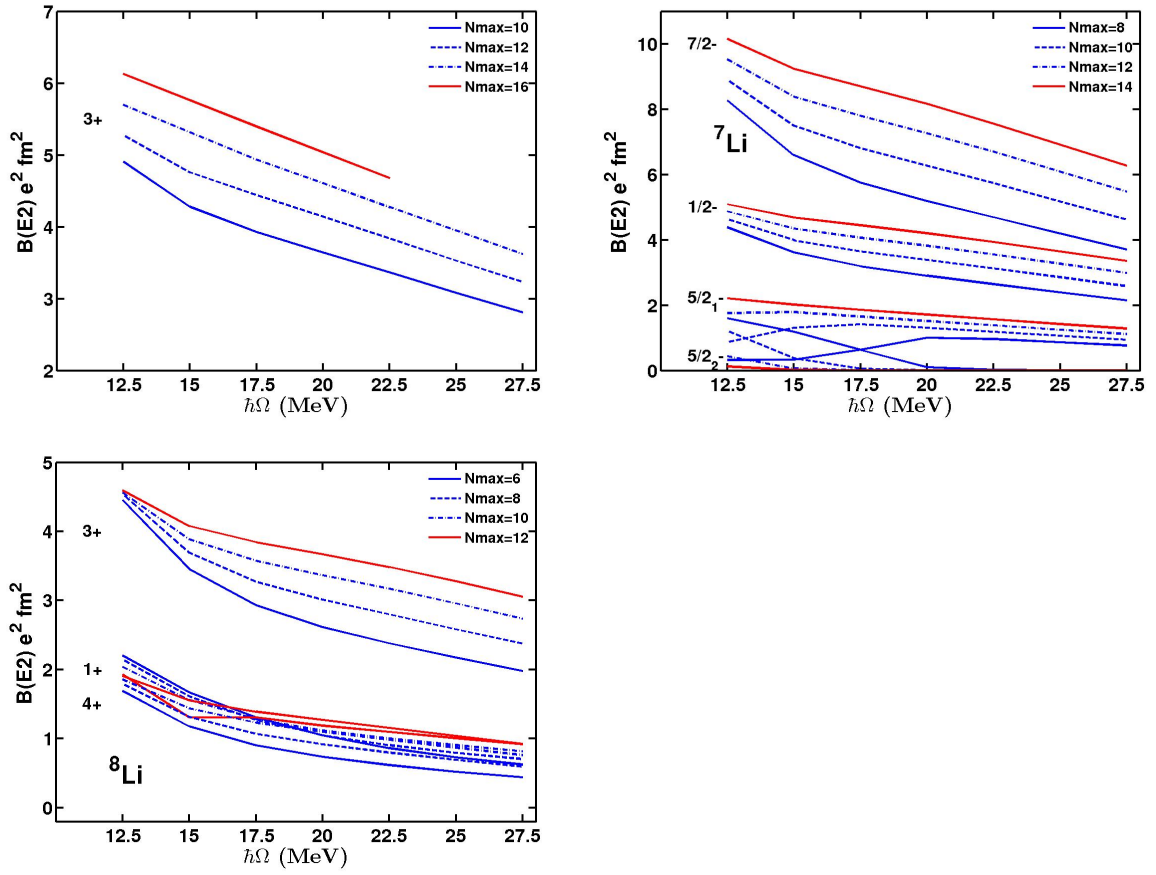
Figure 3.7   The E2 neutron moments (left) proton moments (right) are shown at various $N_{\max}$ values as a function of the HO energy for ^{6}Li, ^{7}Li, and ^{8}Li (top to bottom).

^{6}Li	Expt.	JISP16	AV18/IL2	CD-B	INOY
$E_{\mathrm{b}}(1^+,0)$	31.994	31.49(3)	32.0(1)	29.07	32.3(2)
$\langle r^2_{pp}\rangle^{1/2}$	2.45(5)	2.3	2.39(1)	2.25	2.14
$E_{\mathrm{x}}(3^+,0)$	2.186(2)	2.56(2)	2.2(2)		
$E_{\mathrm{x}}(0^+,1)$	3.56(1)	3.68(6)	3.4(2)		
$E_{\mathrm{x}}(2^+,0)$	4.312(22)	4.5(3)	4.2(2)		
$E_{\mathrm{x}}(2^+,1)$	5.366(15)	5.9(2)	5.5(2)		
$Q(1^+,0)$	-0.082(2)	-0.077(5)	-0.32(6)	-0.066	0.080
$Q(3^+,0)$	-	-4.9			
$\mu(1^+,0)$	0.822	0.839(2)	0.800(1)	0.843	0.843
$\mu(3^+,0)$	-	1.866(2)			
B(E2;$(3^+,0)$)	10.7(8)	6.1	11.65(13)		
B(E2;$(2^+,0)$)	4.4(23)	7.5	8.66(47)		
B(M1;$(0^+,1)$)	15.43(32)	14.2(1)	15.02(11)		
B(M1;$(2^+,0)$)	-	< 0.001	0.002(1)		
B(M1;$(2^+,1)$)	0.1 (3)	0.05(1)			
M_{GT}	2.170	2.227(2)	2.18(3)		

Table 3.1   Selected ^{6}Li observables calculated up through $N_{\mathrm{max}} = 16$. The energies are in MeV; the RMS point-proton radius is in fm; the quadrupole moments are in e fm^2; the magnetic moments are in μ_N; the B(E2) transition rates are in e^{2}fm^4; and the B(M1) transition rates are in μ_N^2fm^2. All listed transitions are to the ground state. The energies are obtained from extrapolations to the infinite basis space, with error estimates as discussed in the text; the dipole observables as well as the gs quadrupole moment are converged within the quoted uncertainty; the other quadrupole observables observables and the RMS point-proton radius are evaluated at $\hbar\Omega = 12.5$ MeV. We used Ref. (73) for the experimental value of the RMS radius and Ref. (78) for GT matrix element; the other experimental values are from Refs. (79; 80). AV18/IL2 data are from Refs. (76; 77; 63; 75) and include meson-exchange corrections for the dipole observables; CD-Bonn and INOY data are from Ref. (65), and were calculated at N_{max}=16 and $\hbar\Omega$=11 and 14 MeV respectively for CD-Bonn and INOY, with the INOY gs energy extrapolated to the infinite basis space.

^{7}Li	Expt.	JISP16	AV18/IL2	CD-B	INOY
$E_{\mathrm{b}}(\frac{3}{2}^-)$	39.244	38.57(4)	38.9(1)	35.56	39.6(4)
$\langle r_{pp}^2 \rangle^{1/2}$	2.30(5)	2.2	2.25(1)	2.22	2.05
$E_{\mathrm{x}}(\frac{1}{2}^-)$	0.477	0.52(6)	0.2(1)		
$E_{\mathrm{x}}(\frac{7}{2}^-)$	4.630(1)	5.25(5)	4.9(1)		
$E_{\mathrm{x}}(\frac{5}{2}_1^-)$	6.680(50)	7.1(2)	6.6(1)		
$E_{\mathrm{x}}(\frac{5}{2}_2^-)$	7.460(10)	8.1(1)	7.2(1)		
$Q(\frac{3}{2}^-)$	-4.06(8)	-3.2	-3.6(1)	-3.20	-2.79
$Q(\frac{7}{2}^-)$	-	-5.0			
$Q(\frac{5}{2}_1^-)$	-	-6.0			
$Q(\frac{5}{2}_2^-)$	-	2.3			
$\mu(\frac{3}{2}^-)$	3.256	2.954(5)	3.168(13)	3.01	3.02
$\mu(\frac{1}{2}^-)$	-	-0.76(1)			
$\mu(\frac{7}{2}^-)$	-	3.3(1)			
$\mu(\frac{5}{2}_1^-)$	-	-0.90(2)			
$\mu(\frac{5}{2}_2^-)$	-	-0.39(5)			
B(E2;$\frac{1}{2}^-$)	15.7(10)	10.2	16.2(5)		
B(E2;$\frac{7}{2}^-$)	3.4	5.1	9.92(14)		
B(E2;$\frac{5}{2}_1^-$)	-	1.5			
B(E2;$\frac{5}{2}_2^-$)	-	<0.1			
B(M1;$\frac{1}{2}^-$)	4.92(25)	3.89(2)	4.92(7)		
B(M1;$\frac{5}{2}_1^-$)	-	0.002(1)			
B(M1;$\frac{5}{2}_2^-$)	-	0.02(1)			
M_{GT}					

Table 3.2   Selected ^{7}Li observables calculated up through $N_{\mathrm{max}} = 14$, with the same units as in Table 3.1. The energies are obtained from extrapolations to the infinite basis space, and the magnetic dipole observables are nearly converged, with error estimates as discussed in the text; the RMS point-proton radius and electric quadrupole observables are evaluated at $\hbar\Omega = 12.5$ MeV. Experimental values are from Refs. (73; 79; 80). AV18/IL2 data are from Refs. (76; 77; 63; 75) and include meson-exchange corrections for the dipole observables; CD-Bonn and INOY data are from Ref. (65), and were calculated at N_{max}=12 and $\hbar\Omega$=11 and 16 MeV respectively for CD-Bonn and INOY, with the INOY gs energy extrapolated to the infinite basis space.

^{8}Li	Expt.	JISP16	AV18/IL2	CD-B	INOY
$E_{\text{b}}(2^+)$	41.277	40.3(2)	41.9(2)	35.82	41.3(5)
$\langle r_{pp}^2 \rangle^{1/2}$	2.21(6)	2.1	2.09(1)	2.17	2.01
$E_{\text{x}}(1^+)$	0.981	1.5(2)	1.4(3)		
$E_{\text{x}}(3^+)$	2.255(3)	2.8(1)	2.5(3)		
$E_{\text{x}}(4^+)$	6.53(2)	7.0(3)	7.2(3)		
$Q(2^+)$	3.27(6)	2.6	3.2(1)	2.78	2.55
$Q(1^+)$	-	1.2			
$Q(3^+)$	-	-2.0			
$Q(4^+)$	-	-3.4			
$\mu(2^+)$	1.654	1.3(1)	1.65(1)	1.24	1.42
$\mu(1^+)$	-	-2.2(2)			
$\mu(3^+)$	-	2.0(1)			
$\mu(4^+)$	-	1.84(1)			
B(E2;1^+)	-	1.9			
B(E2;3^+)	-	4.6			
B(E2;4^+)	-	1.9			
B(M1;1^+)	5.0(16)	3.7(2)			
B(M1;3^+)	0.52(23)	0.25(5)			
M_{GT}					

Table 3.3   Selected ^{8}Li observables calculated up through $N_{\max} = 12$, with the same units as in Table 3.1. The energies are obtained from extrapolations to the infinite basis space, and the magnetic dipole observables are nearly converged, with error estimates as discussed in the text; the RMS point-proton radius and electric quadrupole observables are evaluated at $\hbar\Omega = 12.5$ MeV. Experimental values are from Refs. (73; 81; 82). AV18/IL2 data are from Refs. (75; 63) and does not include meson-exchange corrections for the magnetic moment; CD-Bonn and INOY data are from Ref. (65), and were calculated at $N_{max}=12$ and $\hbar\Omega=12$ and 16 MeV respectively for CD-Bonn and INOY, with the INOY gs energy extrapolated to the infinite basis space.

CHAPTER 4.   Density Results

4.1   Select Li Results

A closer look at the 3-dimensional one-body densities, free of spurious cm effects, helps to develop a physical intuition for the *ab initio* structure of a nucleus. Although it is easier to perform the deconvolution of the cm density after integrating out all angle-dependence, one can also deconvolute the full 3-dimensional density. However, a detailed investigation of the numerical convergence can be challenging for these 3-dimensional densities since different regions will likely converge at different rates. This can be seen in Fig. 4: the interior region of the density appears to be converging nicely while the tail region is much more dependent on the N_{max} truncation. We therefore present all our 3-dimensional density distributions in the largest basis space at $\hbar\Omega = 12.5$ MeV only, where the RMS radius, as well as the quadrupole moments (which are closely related to the shape of the wavefunction), generally appear to be reasonably converged.

In order to produce the density that represents the actual shape of a specific state of a nucleus in a translationally-invariant (inertial) frame, we set $M_J = J$ for all our calculations of the local density. We select the maximal positive angular momentum projection along axis of quantization, the z-axis. This also seems like the natural choice since the quadrupole moment Q is defined as the E2 matrix element at $J = M_J$ (or equivalently, to the reduced E2 matrix element). Note that even though we calculate 3-dimensional density distributions, our results are symmetric under rotations around the z-axis: the wavefunctions have azimuthal symmetry.

Fig. 4.1 shows the matter density for the lowest two states of ^{6}Li. Both states are oblate (wider in the horizontal direction - perpendicular to the z-axis), though the $(1^+, 0)$ state is nearly spherical whereas the $(3^+, 0)$ state is strongly oblate (elongated along the x-axis). Indeed,
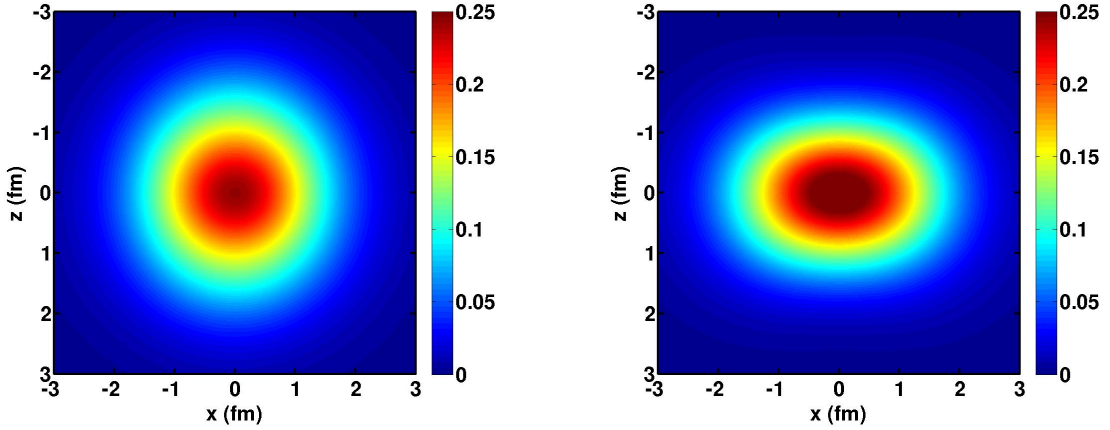
Figure 4.1   The $y = 0$ slice of the translationally-invariant matter density in the x-z plane for the gs of ^{6}Li (left, $J = 1$) is contrasted with the density for the first excited state (right, $J = 3$). These densities were calculated at $N_{\mathrm{max}} = 16$ and $\hbar\Omega = 12.5$ MeV.

the relative deformation of the translationally-invariant densities for the gs and first excited state is implied by the results in Table 3.1 for their respective quadrupole moments. The gs has a negative calculated quadrupole that is near zero, in close agreement with experiment. In contrast, the first excited state has a large and negative calculated quadrupole moment.

In the literature, one often encounters the long-established collective model, which works in an intrinsic (non-inertial) reference frame. This often causes confusion when describing the shape of a nuclear density distribution. In order to clarify this, it is worth commenting that our use of the terms "prolate" and "oblate" characterize the shapes in the inertial frame, not a body-fixed axis as is common for discussions of shapes in the collective model (60). In the inertial frame of reference positive quadrupole moments correspond to prolate shapes and negative quadrupole moments correspond to oblate shapes.

Fig. 4.2 illustrates the effect of M_J on the density distribution as we see the oblate shape of the density at $M_J = 3$ (top left) morph into the prolate shape at $M_J = 0$ (bottom right). Calculating the density when $J \neq M_J$ gives a density whose azimuthal symmetry axis is not aligned with the spin, e.g. at $M_J = 0$ the spin is aligned with the x-y plane, perpendicular to the z-axis. The oblate shape we found at $M_J = 3$ is now also perpendicular to the z-axis. On the other hand, we do have an azimuthal symmetry around the z-axis. Therefore, what we
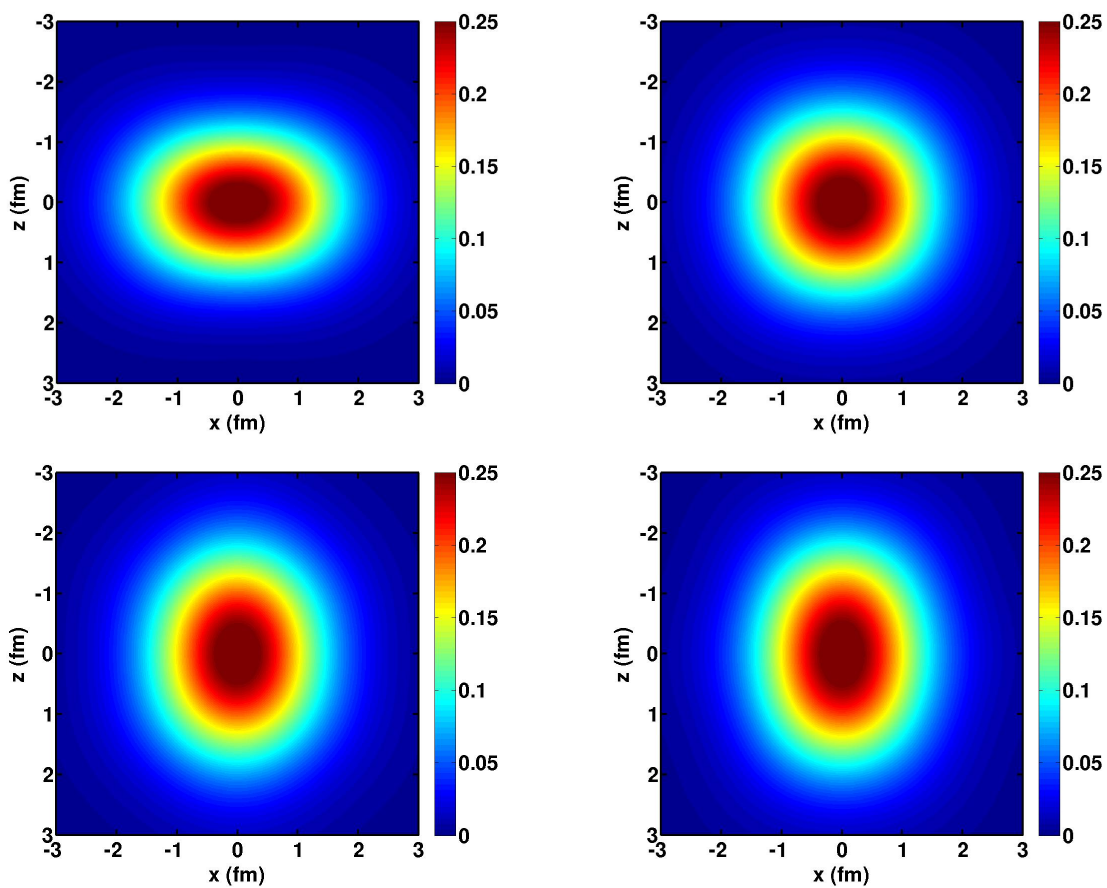
Figure 4.2   The $y = 0$ slice of the translationally-invariant matter density in the x-z plane for first excited 3^+ state of ^{6}Li with $M_j = 3, 2, 1, 0$ clockwise from the top left.
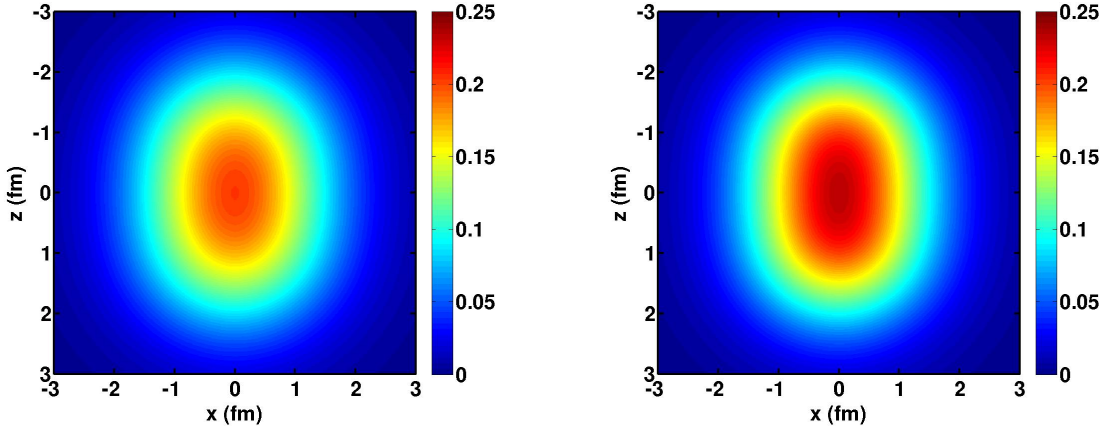
Figure 4.3   The $y = 0$ slice of the gs matter density of ^{7}Li before (left) and after (right) decon-volution of the spurious cm motion. These densities were calculated at $N_{\max} = 14$ and $\hbar\Omega = 12.5$ MeV.

obtain is an oblate shape perpendicular to the z-axis, but with its principle axis (symmetry axis) averaged over all directions in the x-y plane. This results in a prolate shape at $M_J = 0$, as we see in the bottom panel of Fig. 4.2. Note that we see the same for the E2 matrix element: with $M_J = 0$, the E2 matrix element for this state is positive, but the corresponding quadrupole moment, shown in Table 3.1, is negative.

The effect of the cm motion on the density is shown in Fig. 4.3 for the gs of ^{7}Li. The left panel shows the space-fixed (sf) density including the cm motion, $\rho_{\text{sf}}^{\Omega}(\vec{r})$. Whereas the right panel shows the translationally-invariant density, $\rho_{\text{ti}}(\vec{r})$. The smearing of the density due to the cm motion leads to a diminished central density; the sf density has a central value of 0.204 nucleons/fm^3 while the ti density has a central value of 0.233 nucleons/fm^3.

The cm motion smearing spreads out the sf density leading to a slower falloff and a larger radius than the ti density. Furthermore, the ti density has a more pronounced oblate shape than the sf density, as would be expected from smearing with a spherically-symmetric function that averages out the non-spherical details. In order to characterize the degree of deformation, we compare the ratio of the long axis to the short axis of the elliptical density slices. The ratio of the long to short axes at half central density is 1.78 for the ti density and 1.60 for the sf density. Note that the extent of the smearing effect from cm motion depends on the HO energy of the basis. The sf density depends on $\hbar\Omega$, even in the limit $N_{\max} \to \infty$, whereas the ti density
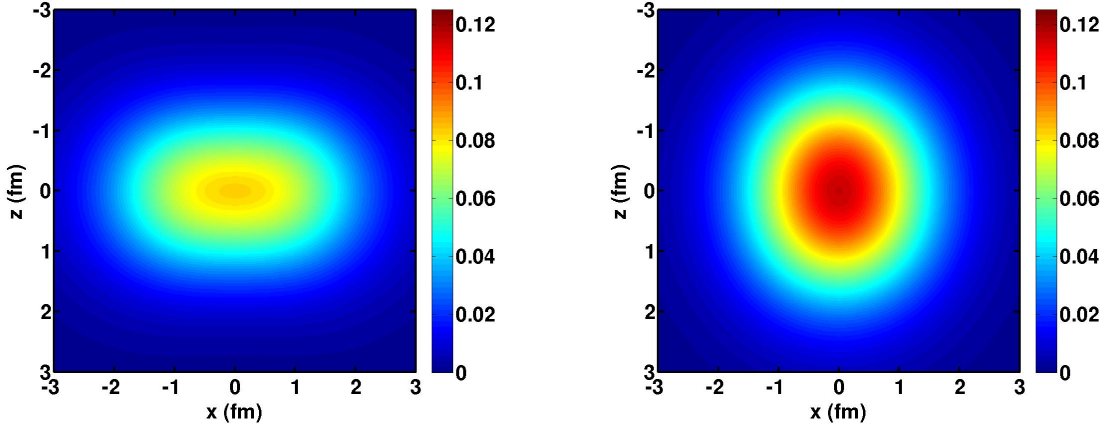
54

Figure 4.4   The $y = 0$ slices of the translationally-invariant proton densities for the first excited $\frac{5}{2}^-$ state (left) and for the second excited $\frac{5}{2}^-$ state (right) of ^{7}Li. These densities were calculated at $N_{\max} = 14$ and $\hbar\Omega = 12.5$ MeV.

becomes independent of the basis in this limit.

Fig. 4.4 contrasts proton densities of the fourth and fifth excited states of ^{7}Li. Although their quantum numbers are equal, $(J^\pi, T) = (\frac{5}{2}^-, \frac{1}{2})$, they have other features that make them quite distinct. Experimentally, the first excited $\frac{5}{2}^-$ is broad, whereas the second excited $\frac{5}{2}^-$ is narrow: their experimental resonance widths are 0.88 MeV and 0.09 MeV respectively. Indeed, as may be expected, our calculated excitation energy is better converged for the higher of these two states. Furthermore, our calculations show significant differences in their structure: the first excited $\frac{5}{2}^-$ has a large negative quadrupole moment, while the second has a moderate positive quadrupole moment (see Table 3.2). Indeed, the density shown in the left panel of Fig. 4.4 is strongly oblate. In contrast the density shown in the right panel shows a moderately prolate shape (we note again that the densities are symmetric around the azimuthal axis, which is the vertical axis is these plots). Another noteworthy difference is observed in the magnitude of the central proton density: the more diffuse $(\frac{5}{2}^-, \frac{1}{2})_1$ state has a central proton density of only 0.08 protons/fm^3 while the $(\frac{5}{2}^-, \frac{1}{2})_2$ state has a central proton density of 0.12 protons/fm^3, 50% higher.

As discussed above, the quadrupole moments and B(E2) transition rates are not well converged due to basis space limitations. In spite of these limitations, the quadrupole moments allow us to qualitatively understand the shape of the proton densities of these states: prolate
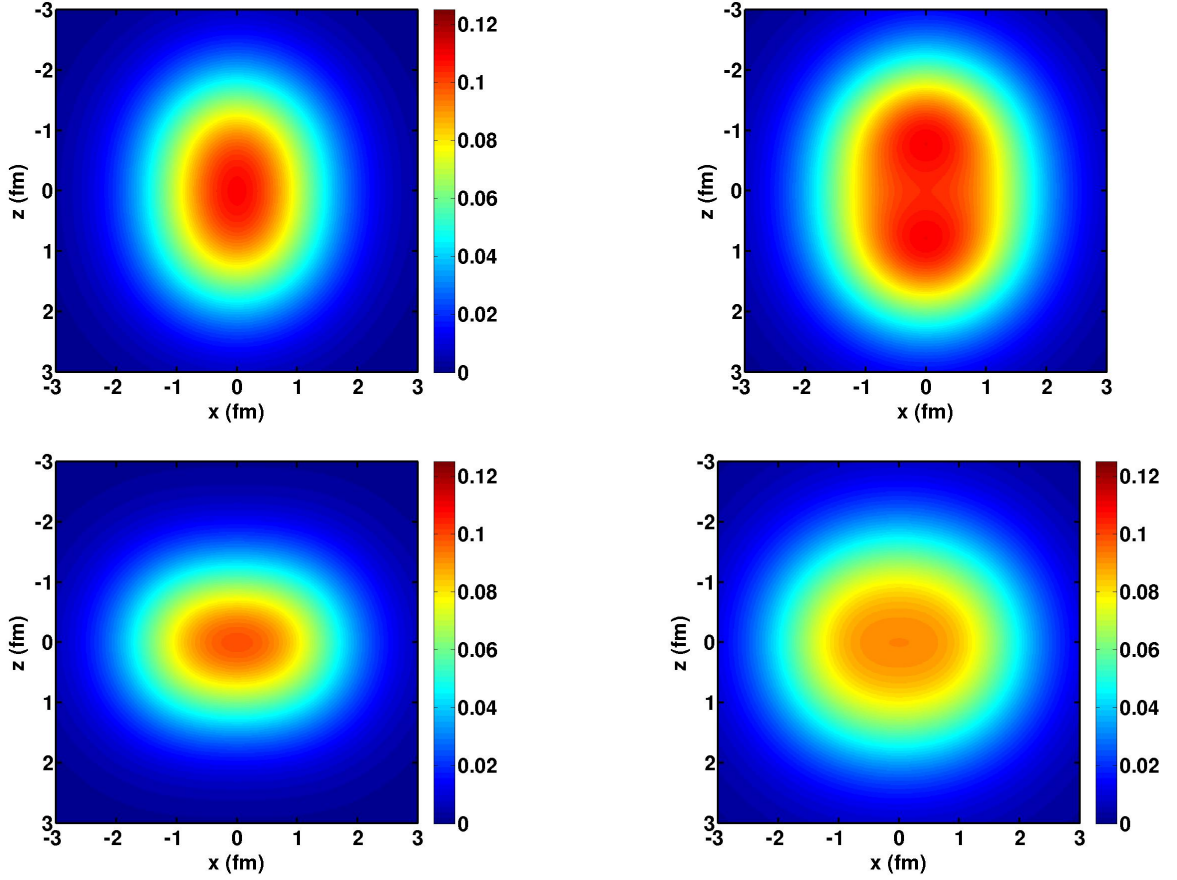
Figure 4.5   The $y = 0$ slice of the translationally-invariant proton (left) and neutron (right) densities of the 2^+ gs (top) and the first excited 4^+ state (bottom) of ^{8}Li. These densities were calculated at $N_{\max} = 12$ and $\hbar\Omega = 12.5$ MeV.

for the 2^+ gs and the first excited 1^+, but oblate for the first excited 3^+ and 4^+ states. Indeed, that is what we see in the left-hand panels of Fig. 4.5, where we plot these densities for the gs and for the 4^+ state.

Interestingly, the neutron density differs by more than a simple scale change from the proton density for these two states, as can be seen from the right-hand panels of Fig. 4.5. In the 2^+ state, the deformation of the neutrons is significantly larger than that of the protons, whereas in the 4^+ state, the deformation of the neutrons is much smaller than that of the protons. This could be experimentally tested using experiments such as PREX (97), which measures neutron mass distributions.

A case of special interest can be seen in the top right panel of Fig. 4.5, or in more detail
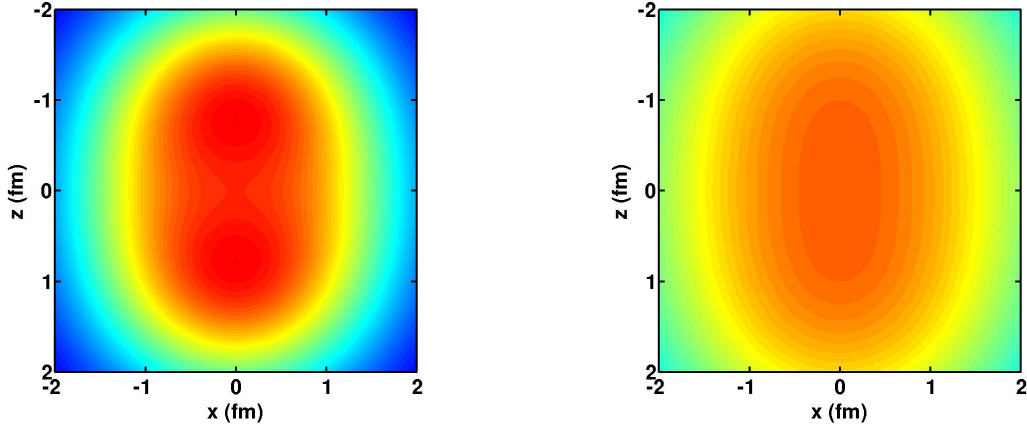
Figure 4.6   The $y = 0$ slice of the translationally-invariant neutron density (left) of the 2^+ gs of ^{8}Li. The space-fixed density for the same state is on the right. These densities were calculated at $N_{\max} = 12$ and $\hbar\Omega = 12.5$ MeV.

in Fig. 4.6. In the left panel of Fig. 4.6 we clearly see non-trivial neutron clustering that is obfuscated in the sf frame (right), highlighting the importance of the deconvolution procedure and the significance of the translationally-invariant density. Furthermore, the ti density (left panel) has a significantly higher density in the central region than the sf density (right panel). Both the ti and the sf densities are normalized to give the same integrated density of five neutrons. That means that the sf density is smeared out over a larger region, and falls off to zero slower than the ti density. This is also evident in Fig. 4.3, where we contrasted the sf and ti matter density of the gs of ^{7}Li: the central density is significantly higher in the ti frame than in the sf frame.

Another way of visualizing these densities is by plotting their multipole components, $\rho^{(K)}(r)$, as is done in Fig. 4.7 for the 2^+ gs and the first excited 4^+ state of ^{8}Li. Qualitatively, the multipole components look very similar for the protons and neutrons in the ground state. The main difference seems to be that the proton densities fall off more rapidly with r than the neutron densities. This is understandable since this is a neutron-rich system and the single-neutron removal energy is less than that of the single-proton removal energy. Note, however, that in comparing in comparing Figs. 4.6 and 4.7 the clustering of the neutrons in the gs of ^{8}Li, shown in the left panel of Fig. 4.6, is not evident from the multipole components $\rho^{(K)}$ of the neutron density displayed in the top right panel Fig. 4.7. Thus, even though the radial
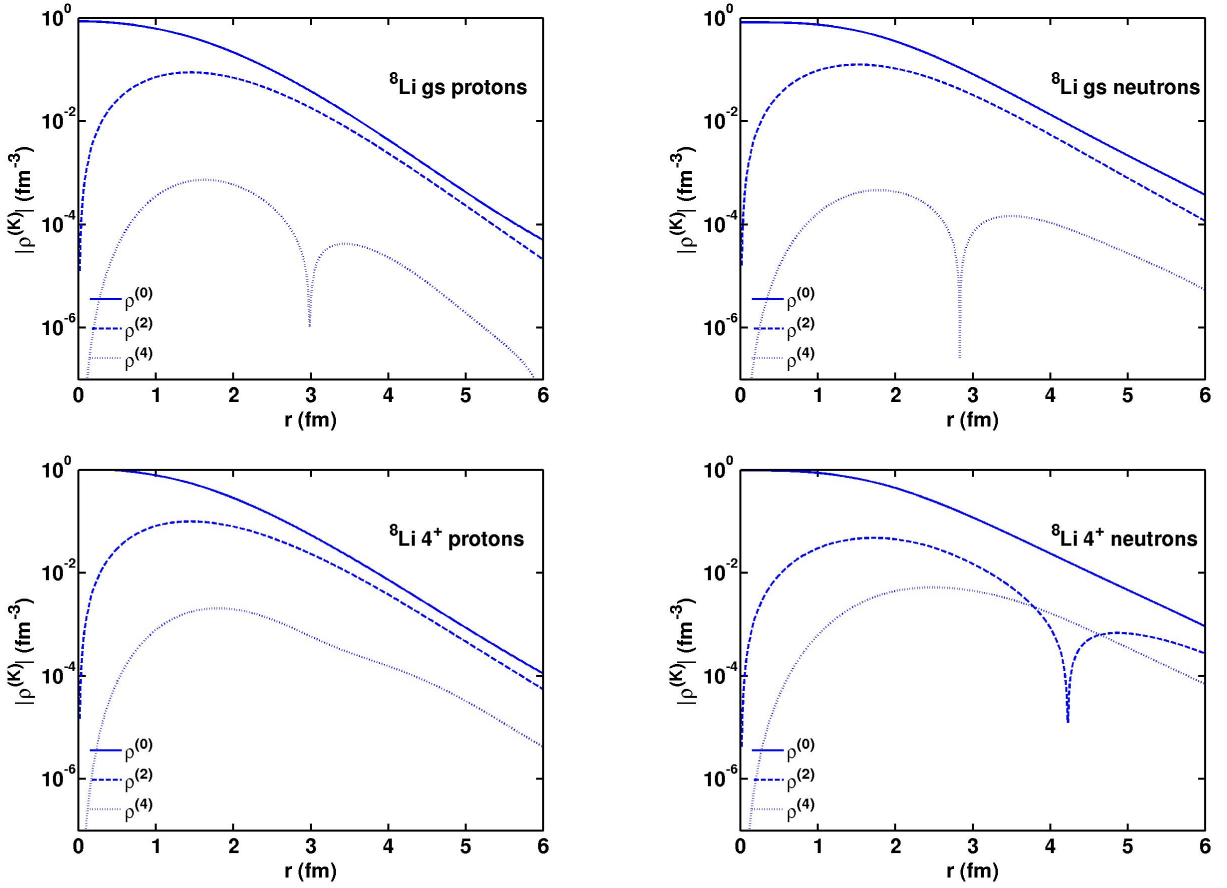
Figure 4.7   The multipole components $\rho_{ti}^{(K)}(r)$ of the proton (left) and neutron (right) densi-
ties of the 2^+ gs (top) and the first excited 4^+ state of ^{8}Li. These densities were
calculated at $N_{\max} = 12$ and $\hbar\Omega = 12.5$ MeV. Monopole and quadrupole distribu-
tions for the gs are all positive. The $K = 4$ distributions for the gs are negative
in the interior and positive in the tail region. For the 4^+ state, the monopoles
are positive while the quadrupole is negative for the protons and negative for the
interior of the neutrons. Both $K = 4$ distributions are positive for the 4^+ state.

multipole densities of the protons and neutrons look qualitatively similar, the corresponding
3-dimensional densities look qualitatively different.

On the one hand, the monopole proton and densities of the first excited 4^+ state of ^{8}Li
are similar to those of the ground state, with the proton density falling off more rapidly than
the neutron density. On the other hand, the higher multipole components $\rho^{(K)}(r)$ of the first
excited 4^+ state of ^{8}Li look are qualitatively quite different than those of the ground state,
as well as different for the protons and the neutrons. The quadrupole density of the neutrons
in the 4^+ state have a node, in contrast to those of the protons. Neither the proton nor the

neutron octupole density has a node in the 4^+ state, whereas both the proton and the neutron octupole density has a node in the ground state.

We provide another view of the multipole content of the local non-spherical charge-dependent density distributions for the gs of ^{8}Li in Fig. 4.8. Here, we plot the various multipole components for the proton density (left panels) and neutron density (right panels) defined as their total contribution to the total density - i.e. as the respective full terms contributing to the sum given in Eq. 2.23. The angular dependences are governed by the spherical harmonic factors. These densities reveal significant differences between the protons and the neutrons at each multipolarity. Note, in particular, that the neutron quadrupole density has larger (in magnitude) features than the proton quadrupole density. While, for the hexadecapole densities, the situation is reversed with the protons having larger (in magnitude) features.

To determine the relative density distributions, it is often convenient to subtract the proton density from the neutron density (or vice-versa). In Fig. 4.9, we show the neutron minus proton density of the gs of ^{8}Li. We see that the proton density is slightly higher in the center of the nucleus, while the neutron density is higher everywhere else, and notably so above and below the center along the azimuthal axis. Fig. 4.9 shows indications of clustering (localization of a group of nucleons in a subvolume of the nucleus) more clearly that simply presenting the neutron density alone.

Although these densities are not (yet) fully converged, we feel that the qualitative features will persist in the limit of a complete basis. In particular salient differences between different states and/or between the proton and neutron densities are likely to survive such a limit.

4.2   Selected Be Results

The following density distributions were calculated from OBDM's provided by Maris et al (83). We present results for the gs, 2nd excited state. and 7th excited state of ^{9}Be. These densities provide an overview of typical interesting features we see in ^{9}Be. We continue to see indications of neutron clustering in these figures as well as proton clustering in the gs and 7th excited state. The indications of proton clustering are likely due to the extra proton when compared to the Li isotopes. Neutron minus proton density distributions show the localization

in different regions of both species of particles. These results further show the importance of the deconvolution procedure. They indicate that the deconvolution is more important as the number of nucleons increases.

In Fig. 4.10, we examine the ti densiy of the protons, neutrons, and neutrons minus protons of the $3/2^-$ gs of ^{9}Be. We see indications of possible clustering in both the proton and neutron densities. The proton density is slightly higher in the center, and the neutron density is higher everywhere else, as expected, due to the number of neutrons. The neutrons appear to form a toroidal shell around the higher central proton density.

In Fig. 4.11, we examine the ti densiy of the protons, neutrons, and neutrons minus protons of the 2nd excited state ($J^\pi = 5/2^-$) of ^{9}Be. In this case the proton and neutron density distributions have opposite signed quadrupole moments. $Q_{prot} = -2.2$ and $Q_{neut} = 0.2$. This is apparent from the obviously oblate proton distribution and nearly spherical neutron distribution. As we have seen before, the proton density is higher than the neutron density only in the center. As expected, due to the oblate shape of the proton density distribution, the neutrons outweigh the protons most significantly along the azimuthal axis.

In Fig. 4.12, we examine the ti densiy of the protons and neutrons of the 7th excited state ($J^\pi = 9/2^-$) of ^{9}Be. Both the proton and neutron density distributions have a strong prolate shape and appear to form a toroid in the x-y plane.
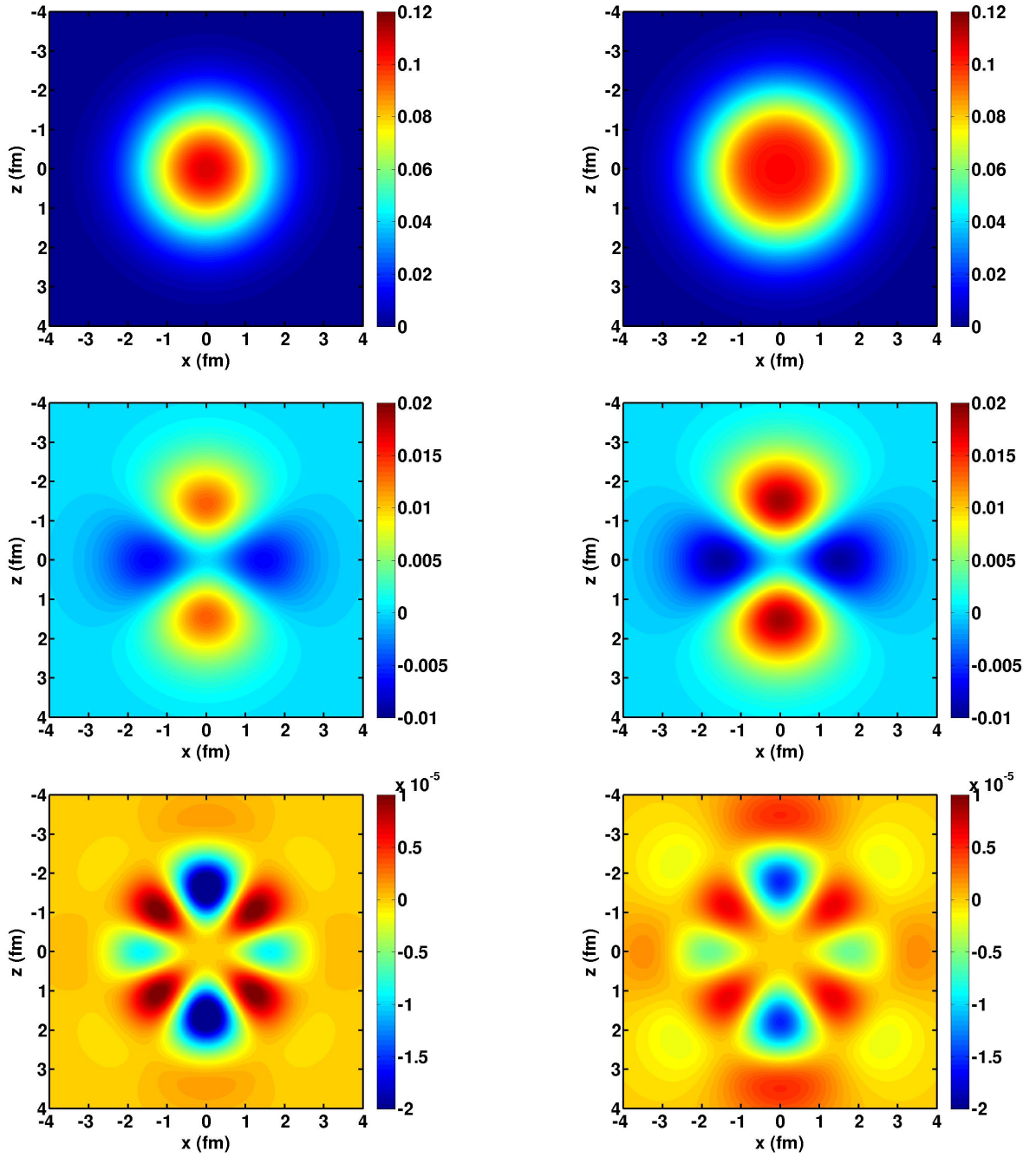
Figure 4.8   The $y = 0$ slices of the translationally-invariant proton (left) and neutron (right) densities of the 2^+ gs of ^{8}Li. From top to bottom, we present the monopole, quadrupole and hexadecapole densities respectively. These densities were calculated at $N_{\max} = 12$ and $\hbar\Omega = 12.5$ MeV.
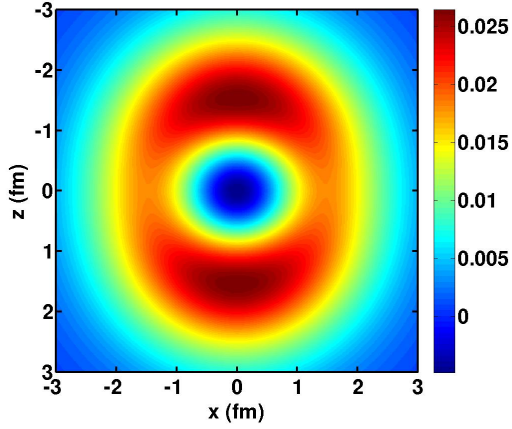
Figure 4.9   The $y = 0$ slices of the translationally-invariant neutron density minus the proton density ofthe 2^+ gs of ^{8}Li. The proton and neutron densities were calculated at $N_{\max} = 12$ and $\hbar\Omega = 12.5$ MeV.
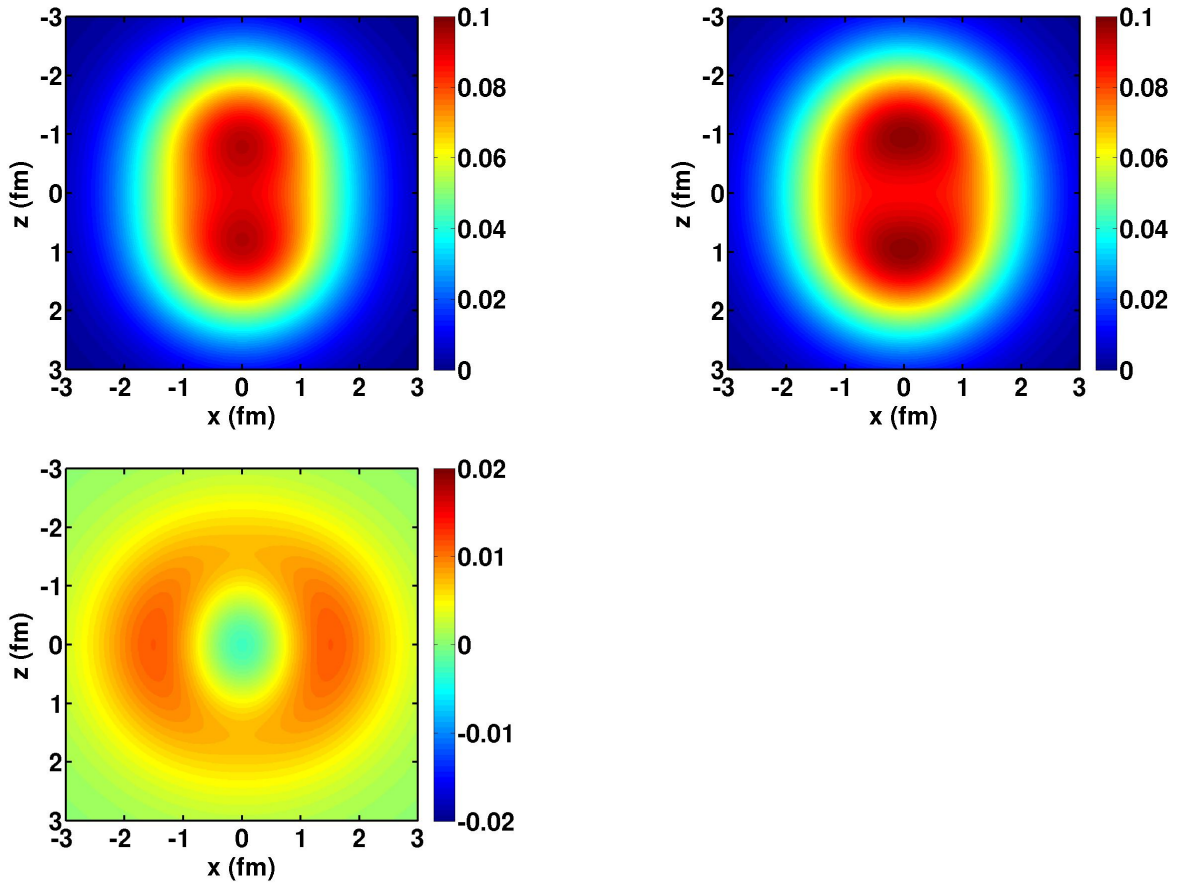
Figure 4.10   The $y = 0$ slices of the translationally invariant proton density (top left), neutron density (top right), and neutron minus proton density (bottom) of the $3/2^-$ gs of ^{9}Be. These densities were calculated at $N_{max} = 10$ and $\hbar\Omega = 12.5$ MeV.
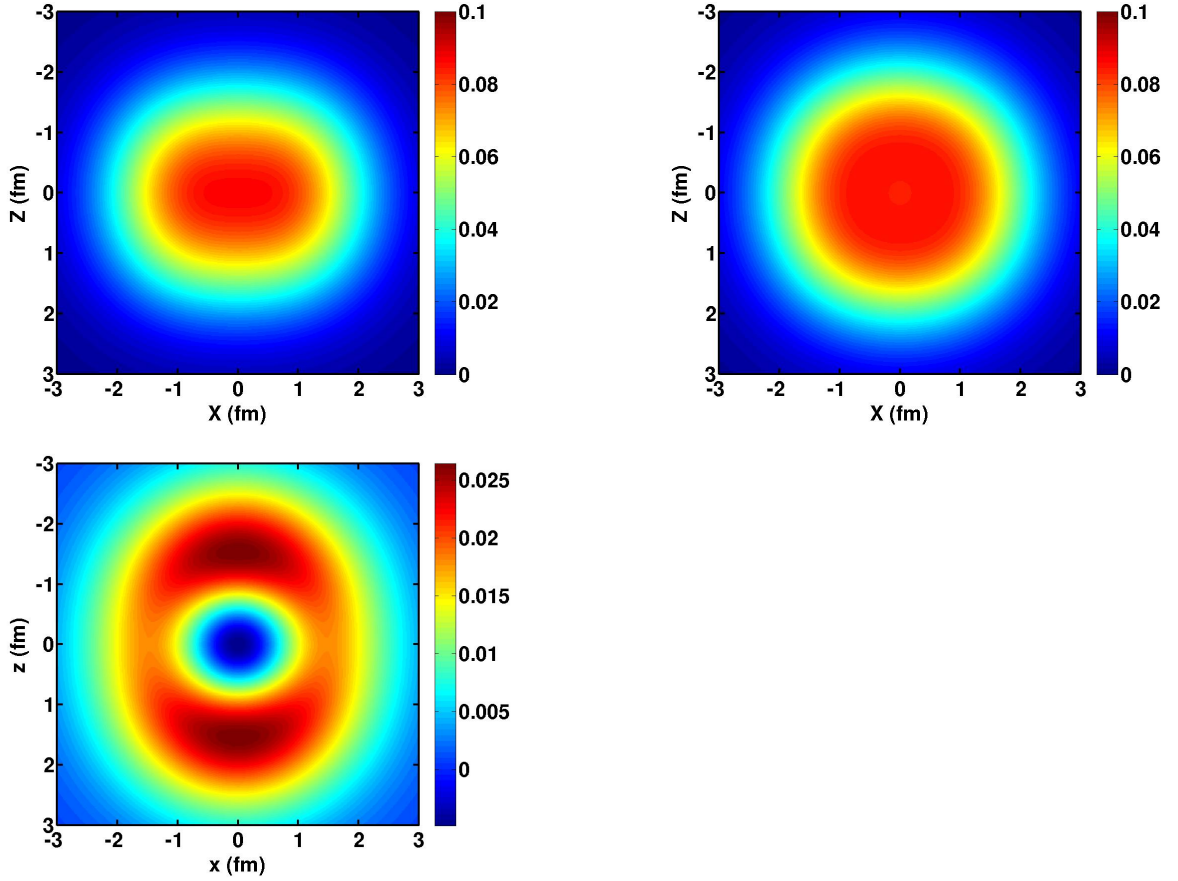
Figure 4.11   The $y = 0$ slices of the translationally invariant proton density (top left), neutron density (top right), and neutron minus proton density (bottom) of the 2nd excited state (J=5/2$^-$) of ^{9}Be. These densities were calculated at $N_{max} = 10$ and $\hbar\Omega = 12.5$ MeV.
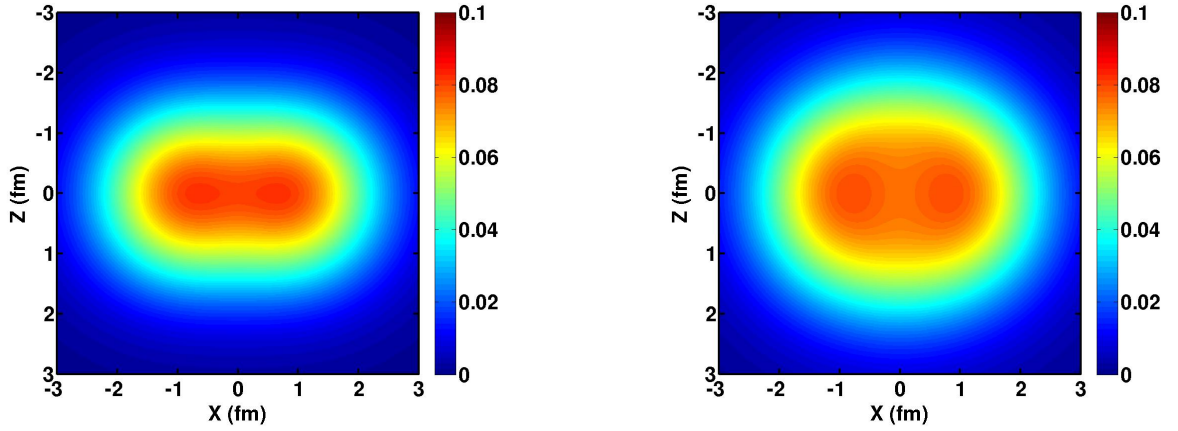

Figure 4.12   The $y = 0$ slices of the translationally invariant proton density (left) and neutron density (right) of the 7th excited state (J=9/2$^-$) of ^{9}Be. These densities were calculated at $N_{max} = 10$ and $\hbar\Omega = 12.5$ MeV.

CHAPTER 5.   The Wigner Function

The Wigner Function (WF) is a quantum-mechanical analog to the classical phase space distribution. The WF was first introduced by Wigner in (7) as the Fourier transform of a non-local OBDM:

$$W(\vec{R}, \vec{p}) \;=\; \left(\frac{1}{2\pi}\right)^3 \int d^3y\, e^{-i\vec{p}\cdot\vec{y}} \rho(\vec{r_1} + \frac{\vec{y}}{2}, \vec{r_1} - \frac{\vec{y}}{2}), \tag{5.1}$$

where $\vec{R} = \vec{r}_1 + \vec{r}_2$. Many basic observables, e.g., matter density, momentum density, etc., are calculated using the same integrals over the WF as one would use in classical physics (84). The WF is often used as a starting point for semi-classical approximations.

The WF in nuclear physics has been used to study fragmentation cross sections (85), dynamics and surface vibrations of heavy ion collisions (86), and to calculate the smoothly varying regions of the binding energies of nuclei (87). The WF can also be used to calculate the kinetic energy density (84).

The WF is normalized such that:

$$\int W(\vec{R}, \vec{p}) d^3R \;=\; \tilde{\rho}(\vec{p}) \tag{5.2}$$

$$\int W(\vec{R}, \vec{p}) d^3p \;=\; \rho(\vec{R}) \tag{5.3}$$

$$\tag{5.4}$$

In this section, we provide derivations for a sf and ti WF. We then introduce a novel method to display the full 6-dimensional WF.

5.1   Derivation of Space Fixed Wigner Function

We begin with the sf OBDM as it is output from MFDn:

$$\rho_{\alpha\beta}^{fi} \;=\; \langle \Psi_f | a_\alpha^\dagger a_\beta | \Psi_i \rangle. \tag{5.5}$$

In subsequent expressions, we will supress the superscript, fi for compactness of notation. Using Eq. 5.5 we construct the non-local density distribution:

$$\rho_{sf}(\vec{r_1}, \vec{r_1}') = \sum_{\alpha\beta} \rho_{\alpha\beta} \phi_\alpha^*(\vec{r_1}) \phi_\beta(\vec{r_1}') \tag{5.6}$$

where α represents the quantum numbers n, l, j, m_j. We will let Latin indices represent the quantum numbers n, l, m_l. The product of two TDHOWF's in the n, l, j, m_j basis is:

$$\phi_\alpha(\vec{r_1}) \phi_\beta(\vec{r_1}') = \sum_{m_l m_s} \delta_{m_{j_\alpha} m_{j_\beta}} \langle l_\alpha m_l s m_s | j_\alpha m_j \rangle \langle l_\beta m_l s m_s | j_\beta m_j \rangle \phi_i(\vec{r_1}) \phi_j(\vec{r_1}'), \tag{5.7}$$

where $i = \{n_\alpha, l_\alpha, m_l\}$.

Which gives us the OBDM:

$$\rho(\vec{r_1}, \vec{r_1}') = \sum_{i,j} c_{ij} \phi_i^*(\vec{r_1}) \phi_j(\vec{r_1}') \tag{5.8}$$

where

$$c_{ij} = \rho_{\alpha\beta} \langle l_\alpha m_l s m_s | j_\alpha m_j \rangle \langle l_\beta m_l s m_s | j_\beta m_j \rangle \tag{5.9}$$

The Wigner function for a single term of the OBDM is

$$W_{ij}(\vec{R}, \vec{p}) = \left(\frac{1}{2\pi}\right)^3 \int d^3y \, e^{-i\vec{p}\cdot\vec{y}} \phi_i^*(\vec{r_1} + \frac{\vec{y}}{2}) \phi_j(\vec{r_1} - \frac{\vec{y}}{2}). \tag{5.10}$$

The Wigner function for the entire OBDM is

$$W(\vec{R}, \vec{p}) = \sum_{i,j} c_{ij} W_{ij}(\vec{R}, \vec{p}). \tag{5.11}$$

In order to solve the Wigner function analytically, we must use the Talmi Transformation, which states that, for two generic TDHOWF's:

$$\psi_{n_1 l_1 m_1}(\vec{q_1}) \psi_{n_2 l_2 m_2}(\vec{q_2}) = \sum \langle l_1 m_1 l_2 m_2 | \lambda\mu \rangle \langle lmLM | \lambda\mu \rangle (nlNL\lambda | n_1 l_1 n_2 l_2 \lambda)$$
$$\times \psi_{nlm}(\vec{q}) \psi_{NLM}(\vec{Q}) \tag{5.12}$$

where $\vec{q} = \vec{q_1} - \vec{q_2}$ and $\vec{Q} = \frac{(\vec{q_1} + \vec{q_2})}{2}$. This leads to:

$$W_{ij}(\vec{R}, \vec{p}) = \frac{(-1)^{m_1}}{(2\pi)^3} \int d^3y \, e^{-i\vec{p}\cdot\vec{y}} \sum \langle l_1 m_1 l_2 m_2 | \lambda\mu \rangle \langle lmLM | \lambda\mu \rangle (nlNL\lambda | n_1 l_1 n_2 l_2 \lambda)$$
$$\times \phi_{nlm}(\vec{y}) \phi_{NLM}(\vec{R}) \tag{5.13}$$

where $(nlNL\lambda|n_1l_1n_2l_2\lambda)$ is a Talmi-Moshinsky Bracket, defined in (50). Note that we use the Spherical Harmonic convention:

$$Y_l^{-m}(\theta,\phi) \;=\; (-1)^m \bar{Y}_l^m(\theta,\phi). \tag{5.14}$$

Because our calculations are done in the m-scheme, we have $m_{j\alpha} = m_{j\beta}$, so $m_1 = m_2$ and $\mu = 0$. We can now show that

$$
\begin{aligned}
W_{ij}(\vec{R},\vec{p}) \;=\; & \frac{(-1)^{m_1}}{(2\pi)^3} \int d^3y\, e^{-i\vec{p}\cdot\vec{y}} \sum \langle l_1 - m_1 l_2 m_1|\lambda 0\rangle \langle lmL - m|\lambda 0\rangle (nlNL\lambda|n_1l_1n_2l_2\lambda) \\
& \times \phi_{nlm}(\vec{y})\phi_{NL-m}(\vec{R})
\end{aligned} \tag{5.15}
$$

The Fourier Transform of a TDHOWF is well-known and has the form

$$\frac{1}{(2\pi)^{3/2}} \int d^3q\, e^{-i\vec{p}\cdot\vec{q}} \psi_{nlm}(\vec{q}) \;=\; i^{2n+l}\psi_{nlm}(\vec{p}) \tag{5.16}$$

Our Wigner Function then becomes

$$
\begin{aligned}
W_{ij}(\vec{q},\vec{p}) \;=\; & \frac{(-1)^{m_1}}{(2\pi)^{3/2}} \sum \langle l_1 - m_1 l_2 m_1|\lambda 0\rangle \langle lmL - m|\lambda 0\rangle (nlNL\lambda|n_1l_1n_2l_2\lambda) \\
& i^{2n+l}\phi_{nlm}(\vec{p})\phi_{NL-m}(\vec{R})
\end{aligned} \tag{5.17}
$$

Using the following form of the single-particle TDHOWF,

$$\phi_{nlm}(\vec{r}) \;=\; \left[\frac{2(n!)}{\Gamma(n+l+\frac{3}{2})}\right]^{1/2} r^l e^{-r^2/2} L_n^{l+\frac{1}{2}}(r^2)Y_l^m(\theta\phi) \tag{5.18}$$

where $L_n^{l+\frac{1}{2}}$ is an Associated Laguerre Polynomial and Y_l^m is a Spherical Harmonic, r is in units of νr, p is in units of p/ν, our Wigner Function becomes

$$
\begin{aligned}
W_{ij}(\vec{R},\vec{p}) \;=\; & \frac{(-1)^{m_1}}{(2\pi)^{3/2}} \sum \langle l_1 - m_1 l_2 m_1|\lambda 0\rangle \langle lmL - m|\lambda 0\rangle (nlNL\lambda|n_1l_1n_2l_2\lambda) \\
& \left[\frac{4n!N!}{\Gamma(n+l+\frac{3}{2})\Gamma(N+L+\frac{3}{2})}\right]^{1/2} p^l R^L e^{-(R^2+p^2)} \\
& L_n^{l+\frac{1}{2}}(p^2)Y_l^m(\hat{p})L_N^{L+\frac{1}{2}}(R^2)Y_l^{-m}(\hat{R})i^{2n+l}
\end{aligned} \tag{5.19}
$$

The WF can now be written as:

$$W_{ij}(\vec{R},\vec{p}) \;=\; \frac{(-1)^{m_1}}{(8\sqrt{2}\pi^{5/2})} \sum \langle l_1 - m_1 l_2 m_1|\lambda 0\rangle \langle lmL - m|\lambda 0\rangle (nlNL\lambda|n_1l_1n_2l_2\lambda)$$

$$\left[\frac{2^{n+N+l+L+4}n!N!}{(2n+2l+1)!!(2N+2L+1)!!}\right]^{1/2}\left[\frac{(2l+1)(2L+1)(l-|m|)!(L-|m|)!}{(l+|m|)!(L+|m|)!}\right]^{1/2}$$

$$(-1)^{n+\frac{l}{2}+m}p^l R^L e^{-(R^2+p^2)}L_n^{l+\frac{1}{2}}(p^2)L_N^{L+\frac{1}{2}}(R^2)$$

$$P_l^m(cos(\theta_p))P_L^m(cos(\theta_R))e^{-im(\phi_R-\phi_p)} \tag{5.20}$$

Each value of m has a corresponding -m, so we can further simplify our expression to arrive at the final result:

$$
\begin{aligned}
W_{ij}(\vec{R},\vec{p}) &= \frac{(-1)^{m_1}}{(8\sqrt{2}\pi^{5/2})}\sum 4^x(-1)^{n+\frac{l}{2}+m} \\
&\quad \left[\frac{2^{n+N+l+L+4}n!N!(2l+1)(2L+1)(l-|m|)!(L-|m|)!}{(2n+2l+1)!!(2N+2L+1)!!(l+|m|)!(L+|m|)!}\right]^{1/2} \\
&\quad \langle l_1-m_1l_2m_1|\lambda 0\rangle\langle lmL-m|\lambda 0\rangle(nlNL\lambda|n_1l_1n_2l_2\lambda) \\
&\quad p^l R^L e^{-(R^2+p^2)}L_n^{l+\frac{1}{2}}(p^2)L_N^{L+\frac{1}{2}}(R^2) \\
&\quad P_l^m(cos(\theta_p))P_L^m(cos(\theta_R))cos[m(\phi_R-\phi_p)]
\end{aligned}
\tag{5.21}
$$

where $x=0$ when $m=0$ and $x=1$ when $m\neq 0$. The sum is over $2n_1+l_1+2n_2+l_2=2n+l+2N+L$; $m=0, min(l,L)$; and $min(|l_1-l_2|,|l-L|)\leq\lambda\leq min(|l_1+l_2|,|l+L|)$

5.2 Derivation of Translationally Invariant Wigner Function

Following the method of Yabana (88), we write the sf density distribution as a convolution of the cm density distribution and the ti density distribution:

$$
\begin{aligned}
\rho_{sf}^{fi}(\vec{r_A},\vec{r_A}') &= \int d^3r_1...d^3r_{A-1}\Psi_0\left(\frac{\sum_{i=1}^{A-1}\vec{r_i}+\vec{r_A}}{A}\right)\Psi_0^*\left(\frac{\sum_{i=1}^{A-1}\vec{r_i}+\vec{r_A}'}{A}\right) \\
&\quad \Psi_f\left(\vec{\xi_1},...,\vec{\xi_{A-2}},\vec{r_A}-\frac{\sum_{i=1}^{A-1}\vec{r_i}}{A-1}\right)\Psi_i\left(\vec{\xi_1},...,\vec{\xi_{A-2}},\vec{r_A}'-\frac{\sum_{i=1}^{A-1}\vec{r_i}}{A-1}\right)
\end{aligned}
\tag{5.22}
$$

where the Ψ_0 is a 0s TDHOWF. The $\vec{\xi_j}'s$ are Jacobi coordinates defined by:

$$\xi_i = \sum_{j=1}^{A}T_{ij}\vec{r_j} \tag{5.23}$$

where $(i=1,...,A)$ and T_{ij} is defined by:

$$
\begin{aligned}
T_{ij} &\equiv -1/i, j=1...i \\
&\quad 1, j=i+1(i\neq A); T_{Aj}=\frac{1}{A}, j=1...A \\
&\quad 0, j=i+2...A.
\end{aligned}
\tag{5.24}
$$

We now introduce the Jacobi coordinates for a system of A-1 particles:

$$\hat{\xi}_j = \xi_j (j = 1...A - 2)$$
$$\hat{\xi}_{A-1} \sum_{r=1}^{A-1} \frac{\vec{r_i}}{A-1}. \tag{5.25}$$

We now change variables from $\{\vec{r_i}\}$ to $\{\vec{\xi_i}\}(i = 1...A - 1)$ and rewrite Eq. 5.22 as:

$$\rho_{sf}^{fi}(\vec{r_A}, \vec{r_A}') = \int d^3\hat{\xi_1}...d^3\xi_{A-1}\Psi_0\left(\frac{(A-1)\hat{\vec{\xi}}_{A-1} + \vec{r_A}}{A}\right)\Psi_0^*\left(\frac{(A-1)\hat{\vec{\xi}}_{A-1} + \vec{r_A}'}{A}\right)$$
$$\times \Psi_f(\hat{\vec{\xi}}_1, .., \hat{\vec{\xi}}_{A-1}, \vec{r_A} - \hat{\vec{\xi}}_{A-1})\Psi_i^*(\hat{\vec{\xi}}_1, .., \hat{\vec{\xi}}_{A-1}, \vec{r_A}' - \hat{\vec{\xi}}_{A-1}). \tag{5.26}$$

Eq. 5.26 can be further rewritten through use of Eq. 2.4:

$$\rho_{sf}^{fi} = \int d^3\xi \Psi_0\left(\frac{(A-1)\vec{\xi} + \vec{r_A}}{A}\right)\Psi_0^*\left(\frac{(A-1)\vec{\xi} + \vec{r_A}'}{A}\right)$$
$$\times \sum_{ij} \rho_{ij}^{ti}(\vec{r_A} - \vec{\xi}, \vec{r_A}' - \vec{\xi}). \tag{5.27}$$

We now explicitly insert the cm density distribution and change variables from $\vec{r_A}, \vec{r_A}'$ through the relation:

$$\vec{r} = \frac{\vec{r_A} + \vec{r_A}'}{2}$$
$$\vec{y} = \vec{r_A} - \vec{r_A}' \tag{5.28}$$

and change $\vec{\xi}$ to $-\vec{\xi} + \vec{r}$. Eq. 5.26 can now be rewritten as:

$$\rho_{ij}^{sf}(\vec{r} + \frac{\vec{y}}{2}, \vec{r} - \frac{\vec{y}}{2}) = \int d^3\xi \left(\frac{2A}{\pi}\right)^{3/2} exp\left[\frac{-2(A-1)^2}{A}\left(\vec{\xi} - \frac{A}{A-1}\vec{r}\right)^2 - \frac{y^2}{2A}\right]$$
$$\times \sum_{ij} \rho_{ij}^{ti}(\vec{\xi} + \frac{\vec{y}}{2}, \vec{\xi} - \frac{\vec{y}}{2}). \tag{5.29}$$

This equation can be inverted to isolate the ti density distribution:

$$\rho_{ij}^{ti}(\vec{\xi} + \frac{\vec{y}}{2}, \vec{\xi} - \frac{\vec{y}}{2}) = \left(\frac{1}{2\pi}\right)^3\left(\frac{A-1}{A}\right)^3 exp\left[\frac{y^2}{2A}\int d^3r d^3k\right.$$
$$\times exp\left[i\vec{k}\left(\frac{A-1}{A}\vec{\xi} - \vec{r}\right) + \frac{k^2}{8A}\right]\rho_{ij}^{sf}(\vec{r} + \frac{\vec{y}}{2}, \vec{r} - \frac{\vec{y}}{2}). \tag{5.30}$$

We now perform the Wigner Transform on Eq. 5.30. We first define:

$$W_{ij}^{(ti)}(\vec{\xi}, \vec{p}) \equiv \left(\frac{1}{2\pi}\right)^3 \int d^3y e^{-i\vec{p}\cdot\vec{y}}\rho_{ij}^{(ti)}(\vec{\xi} + \frac{\vec{y}}{2}, \vec{\xi} - \frac{\vec{y}}{2}). \tag{5.31}$$

We see that:

$$W_{ij}^{(ti)}(\vec{\xi},\vec{p}) = \left(\frac{1}{2\pi}\right)^6 \left(\frac{A-1}{A}\right)^3 \int d^3r d^3k d^3y exp\left[\frac{y^2}{2A}\right] exp\left[i\vec{k}\left(\frac{A-1}{A}\vec{\xi}-\vec{r}\right) + \frac{k^2}{8A}\right] \quad (5.32)$$

$$\times \rho_{ij}^{sf}(\vec{r}+\frac{\vec{y}}{2},\vec{r}-\frac{\vec{y}}{2}). \quad (5.33)$$

We use the definition of the OBDM to rewrite this as:

$$W_{ij}^{(ti)}(\vec{\xi},\vec{p}) = \left(\frac{1}{2\pi}\right)^6 \left(\frac{A-1}{A}\right)^3 \int d^3r d^3k d^3y \exp\left[\frac{y^2}{2A}\right] \exp\left[i\vec{k}\left(\frac{A-1}{A}\vec{\xi}-\vec{r}\right)\right]$$

$$\times \exp\left[\frac{k^2}{8A}\right]\phi_i^*(\vec{r}+\frac{\vec{y}}{2})\phi_j(\vec{r}-\frac{\vec{y}}{2}). \quad (5.34)$$

As above, we perform a Talmi transformation (Eq. 5.12) on the TDHOWF's:

$$W_{ij}^{(ti)}(\vec{\xi},\vec{p}) = \left(\frac{1}{2\pi}\right)^6 \left(\frac{A-1}{A}\right)^3 \int d^3r d^3k d^3y \exp\left[\frac{y^2}{2A}\right] \exp\left[i\vec{k}\left(\frac{A-1}{A}\vec{\xi}-\vec{r}\right)\right] \exp\left[\frac{k^2}{8A}\right]$$

$$\times \sum \langle l_i m_i l_j m_j|\lambda 0\rangle\langle lmLM|\lambda 0\rangle(nlNL\lambda|n_i l_i n_j l_j \lambda)\phi_{nlm}(\vec{y})\phi_{NLM}(\vec{r}). \quad (5.35)$$

We now define

$$\phi^{(x)}(\vec{y}) \equiv \exp\left[\frac{y^2}{2A}\right]\phi(\vec{y}). \quad (5.36)$$

This simply changes the length parameter in the gaussian term of the TDHOWF. While $\phi^{(x)}(\vec{y})$ is not a true TDHOWF, it still has a simple analytic solution to the Fourier transform. Inserting this definition into Eq. 5.35:

$$W_{ij}^{(ti)}(\vec{\xi},\vec{p}) = \left(\frac{1}{2\pi}\right)^6 \left(\frac{A-1}{A}\right)^3 \int d^3r d^3k d^3y \exp\left[i\vec{k}\left(\frac{A-1}{A}\vec{\xi}-\vec{r}\right)\right] \exp\left[\frac{k^2}{8A}\right] \quad (5.37)$$

$$\times \sum \langle l_i m_i l_j m_j|\lambda 0\rangle\langle lmLM|\lambda 0\rangle(nlNL\lambda|n_i l_i n_j l_j \lambda)\phi_{nlm}^{(x)}(\vec{y})\phi_{NLM}(\vec{r}). \quad (5.38)$$

We now define:

$$\widetilde{\phi}^{(\xi)}(\vec{p}) \equiv \int d^3y e^{-i\vec{p}\cdot\vec{y}}\phi^{(x)}(\vec{y}). \quad (5.39)$$

This leads to:

$$W_{ij}^{(ti)}(\vec{\xi},\vec{p}) = \left(\frac{1}{2\pi}\right)^6 \left(\frac{A-1}{A}\right)^3 \sum \langle l_i m_i l_j m_j|\lambda 0\rangle\langle lmLM|\lambda 0\rangle(nlNL\lambda|n_i l_i n_j l_j \lambda)\widetilde{\phi}_{nlm}^{(\xi)}(\vec{p})$$

$$\times \int d^3r d^3k \exp\left[i\vec{k}\left(\frac{A-1}{A}\vec{\xi}-\vec{r}\right)\right] \exp\left[\frac{k^2}{8A}\right]\phi_{NLM}(\vec{r})$$

$$= \left(\frac{1}{2\pi}\right)^6 \left(\frac{A-1}{A}\right)^3 \sum \langle l_i m_i l_j m_j|\lambda 0\rangle\langle lmLM|\lambda 0\rangle(nlNL\lambda|n_i l_i n_j l_j \lambda)\widetilde{\phi}_{nlm}^{(\xi)}(\vec{p})$$

$$\times \int d^3r d^3k \exp\left[i\vec{k}\cdot\left(\frac{A-1}{A}\vec{\xi}\right)\right] \exp\left[-i\vec{k}\cdot\vec{r}\right] \exp\left[\frac{k^2}{8A}\right]\phi_{NLM}(\vec{r}). \quad (5.40)$$

We now define:

$$\widetilde{\phi}_{NLM}(\vec{k}) \;\equiv\; \int d^3r\, e^{-i\vec{k}\cdot\vec{r}}\phi_{NLM}(\vec{r}) \tag{5.41}$$

Our ti Wigner Function now becomes:

$$
\begin{aligned}
W_{ij}^{(ti)}(\vec{\xi},\vec{p}) &= \left(\frac{1}{2\pi}\right)^6\left(\frac{A-1}{A}\right)^3\sum\langle l_im_il_jm_j|\lambda 0\rangle\langle lmLM|\lambda 0\rangle(nlNL\lambda|n_il_in_jl_j\lambda)\widetilde{\phi}_{nlm}^{(\xi)}(\vec{p}) \\
&\quad \times \int d^3k\,\exp\left[i\vec{k}\cdot\left(\frac{A-1}{A}\vec{\xi}\right)\right]\exp\left[\frac{k^2}{8A}\right]\widetilde{\phi}_{NLM}(\vec{k}).
\end{aligned}
\tag{5.42}
$$

Once again we modify the TDHOWF and define:

$$\phi^{(p)}(\vec{\xi}) \;\equiv\; \int d^3k\,\exp\left[i\vec{k}\cdot\left(\frac{A-1}{A}\vec{\xi}\right)\right]\widetilde{\phi}_{NLM}(\vec{k}) \tag{5.43}$$

which leads to our final result:

$$
\begin{aligned}
W_{ij}^{(ti)}(\vec{\xi},\vec{p}) &= \left(\frac{1}{2\pi}\right)^6\left(\frac{A-1}{A}\right)^3\sum\langle l_im_il_jm_j|\lambda 0\rangle\langle lmLM|\lambda 0\rangle(nlNL\lambda|n_il_in_jl_j\lambda) \\
&\quad \times \widetilde{\phi}_{nlm}^{(x)}(\vec{p})\phi_{NLM}^{(p)}(\vec{\xi})
\end{aligned}
\tag{5.44}
$$

5.3   Results

In Fig. 5.1 we compare the sf and ti WF's for the gs of ^{6}Li. These WF's were calculated at $N_{max} = 2$ and $\hbar\Omega = 15 MeV$. The region shown in the figure is the $y = 0$ slice of coordinate space. The arrows represent the momentum vector that maximizes the WF. Because the WF is a pseudo-probability distribution, these momentum vectors can be considered to be the most likely momentum at that point in coordinate space.

The WF by itself can be challenging to interpret in even systems restricted to 1 dimension in coordinate space and 1 dimension in momentum space. Calculating the WF in its full 6 dimensional form adds even new challenges in the interpretation. In Fig. 5.1, we notice that the ti WF has more structure, as expected, but this structure is very difficult to interpret. We notice that the momentum vectors trend to the left throughout the majority of the space presented. The apparent visual asymmetry is an artifact of the choice of the visualization method. In both the sf and ti WF's, we notice an off-axis line which appears to separate the momentum vectors into two different orientations. While the sf WF has these vectors

colliding, the ti WF shows a more subtle shift. The ti WF also shows more symmetry than its sf counterpart.

Further exploration in both the size of the calculation and over a range of proton and neutron numbers is necessary to comment further on these figures.

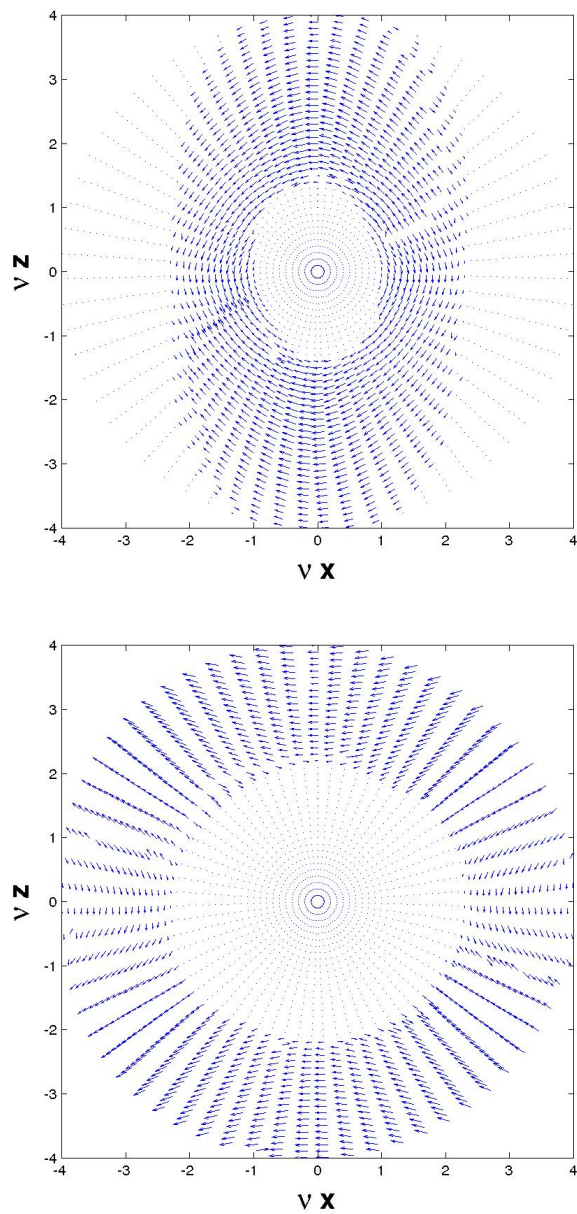Figure 5.1   The $y = 0$ slices of the WF for the gs of ^{6}Li. These were calculated at $N_{max} = 2$ and $\hbar\Omega = 15 MeV$. The arrows represent the momentum vector that maximizes the WF. The sf WF is shown on the top. The ti WF is shown on the bottom.

CHAPTER 6.   Concluding Remarks

We have performed no-core full configuration calculations for the Lithium isotopes, ^{6}Li, ^{7}Li, and ^{8}Li with the realistic NN interaction JISP16. Several observables obtained (gs energies, excitation energies, magnetic dipole moments and reduced magnetic dipole transition probabilities) compare well with both experiment and alternate methods and interactions. For certain observables that are more sensitive to long-range correlations (the RMS radius, electric quadrupole moments, and reduced quadrupole transition probabilities) we were unable to obtain full convergence, though they also compare favorably with alternate methods and interactions.

One-dimensional and three-dimensional translationally-invariant one-body density distributions were calculated for various ground and excited states of ^{6}Li, ^{7}Li, ^{8}Li, and ^{9}Be. These one-body density distributions provide an excellent framework for visualization of nuclear shape distortions and clustering effects. The associated one-body density matrix in the HO basis provides a compact form of all of the quantum one-body information for a given nuclear state. We have made several predictions about the relative differences between neutron and proton density distributions in Li and Be isotopes. With recent advancements in experimental techniques (97), it is now practical to test these predictions.

To improve our convergence, especially for matrix elements of long-range operators, we would require significant increases in basis space sizes (increased $N_{\max}$) and/or alternatives to the HO single-particle basis. Recent advances in the "Importance-Truncated No-Core Shell Model" (89; 90), the "Symmetry-Adapted No-Core Shell Model (SANCSM)" (91) and the "No-Core Monte Carlo Shell Model" (92) are promising new methods for accessing much larger basis spaces.

Further advances in NN interactions, as well as three-body forces, could also help resolve

Nucleus	Previous N_{max}	Previous Result	Current N_{max}	Current Result	Expt.
^{6}Li	12	31.00(31)	16	31.49(3)	31.994
^7Li	10	37.59(30)	14	38.57(4)	39.244
^{8}Li	-	-	12	40.3(2)	41.277

Table 6.1 Current binding energies for Li isotopes are compared with previous results and experiment.

some of the residual differences between theory and experiment. Of course, there is also the possibility that four-body forces may play a significant role.

In Table 6.1, we can see that increasing the model space has not only enhanced our agreement with experimental results, but also shrunk the magnitude of the error estimate by approximately one order of magnitude. Unfortunately, due to the nature of the monotonic convergence, increasing the size of the model space will give us diminishing returns; while the size of the Hamiltonian matrix will still increase by approximately one order of magnitude for each increase in N_{max}, our error bars and experimental agreement will not continue to improve as quickly as the matrix expands. While the SANCSM makes some progress in overcoming these difficulties, it is still to early to determine whether or not it will be successful. It is also important to note that, when using only NN interactions, we are currently unable to quantify the convergence rate of long-range observables. Because of these convergence problems, it is likely that we will need to not only revise the JISP16 interaction, but also include NNN and possibly NNNN terms in order to improve on our current results.

Expressions for the full 6-dimensional space fixed and translationally- invariant Wigner Function were derived. In the literature, the Wigner Function is typically presented as a function of a single coordinate dimension and single momentum dimension. Interpretation of the 6D proved difficult, and as such, we tend not to think of the Wigner Function as an end product by itself, but rather a middle step to more interesting calculations in future work, e.g., fragmentation cross sections.

BIBLIOGRAPHY

[1] P. Maris, A. M. Shirokov and J. P. Vary, Phys. Rev. C **81**, 021301 (2010)

[2] P. Maris, J. P. Vary and A. M. Shirokov, Phys. Rev. C **79**, 014308 (2009)

[3] S. K. Bogner, R. J. Furnstahl, P. Maris, R. J. Perry, A. Schwenk, J. P. Vary, Nucl. Phys. A **801**, 21-42 (2008)

[4] P. Sternberg, E. G. Ng, C. Yang, P. Maris, J. P. Vary, M. Sosonkina, and H. V. Le, in the Proceedings of the 2008 ACM/IEEE conference on Supercomputing IEEE Press, Piscataway, NJ, 15:1-15:12 (2008).

[5] P. Maris, M. Sosonkina, J. P. Vary, E. G. Ng, and C. Yang, Procedia CS 1, 97-106 (2010).

[6] B. D. Keister, W. N. Polyzou, J. Comput. Phys. **134**, 231-235 (1997)

[7] E. P. Wigner, Phys. Rev. **40** 748, (1932).

[8] W. Heisenberg, Zeits. F. Physik **105**, 202 (1932).

[9] J. H. Bartlett, Nature **130**, 165 (1932).

[10] J. H. Bartlett, Phys. Rev. **41**, 370 (1932).

[11] W. M. Elasser, J. de Phys. et Rad. **4**, 549 (1933).

[12] W. M. Elasser, J. de Phys. et Rad. **5**, 389 (1934).

[13] W. M. Elasser, J. de Phys. et Rad. **5**, 635 (1934).

[14] W. M. Elasser, J. de Phys. et Rad. **6**, 473 (1935).

[15] H. A. Bethe and R. F. Bacher, Rev. Mod. Phys. **8**, 82 (1936).

[16] M. G. Mayer, Phys. Rev. **74**, 235 (1948).

[17] M. G. Mayer, Phys. Rev. **75**, 1969 (1949).

[18] M. G. Mayer, Phys. Rev. **78**, 16 (1950).

[19] M. G. Mayer, Phys. Rev. **78**, 22 (1950).

[20] E. Feenberg, Phys. Rev. **75**, 320 (1949).

[21] E. Feenberg and K. C. Hammack, Phys. Rev. **75**, 1877 (1949).

[22] L. Nordheim, Phys. Rev. **75**, 1894 (1949).

[23] Th. Schmidt, Zeits. f. Physik **106**, 358 (1937).

[24] O. Haxel, J. H. D. Jensen, and H. E. Seuss, Die Naturwissenschaften **35**, 376 (1949).

[25] O. Haxel, J. H. D. Jensen, and H. E. Seuss, Zeits. f. Physik **128**, 1295 (1949).

[26] B. A. Brown, Progr. Part. Nucl. Phys. 47, 517 (2001).

[27] T. Otsuka, M. Honma, T. Mizusaki, N. Shimizu, and Y. Utsuno, Prog. Part. Nucl. Phys. 47, 319 (2001).

[28] B. Barrett, P. Navratil, and J. P. Vary, Unpublished

[29] P. Navrátil, J. P. Vary and B. R. Barrett, Phys. Rev. C **62**, 054311 (2000).

[30] D. J. Rowe abd J. L. Wood, *Fundamentals of Nuclear Models*, World Scientific, New Jersey (2010).

[31] J. Da Providencia and C. M. Shakin, Ann. Phys. N.Y. 30, 95 1964.

[32] K. Suzuki and S. Y. Lee, Prog. Theor. Phys. 64, 2091 1980. K. Suzuki, Prog. Theor. Phys. 68, 246 1982; K. Suzuki and R. Okamoto, ibid. 70, 439 1983.

[33] K. Suzuki and S. Y. Lee, Prog. Theor. Phys. **64**, 2091 (1980); K. Suzuki, ibid. 68, 246 (1982); **68**, 1999 (1982); K. Suzuki and R. Okamoto, Prog. Theor. Phys. **92**, 1045 (1994).

[34] D.H. Gloekner and D.R. Lawson, Phys. Lett. B **53**, 313 (1974).

[35] N. Ishii, S. Aoki, T. Hatsuda, Phys. Rev. Lett. **99** 022001, (2007).

[36] R. K. Bhaduri, *M*odels of the Nucleon from Quarks to Soliton, Addison-Wesley, Redwood City, CA (1988).

[37] H. Yukawa, Proc. Phys. Math. Soc. **17** 48, (1935).

[38] M. Born, W. Heisenberg, and P. Jordan, Z. Phys. **35** 557, (1926).

[39] J. Gammel and R. Thaler, Phys. Rev. **107** 1337, (1957). T. Hamada and I. D. Johnston, Nucl. Phys **34** 382, (1962). K. E. Lasilla, Phys. Rev. **126** 881, (1962).

[40] R. V. Reid, Ann. Phys. **50** 411, (1968).

[41] A. M. Shirokov, J. P. Vary, A. I. Mazur, and T. A. Weber, Phys. Lett. B **644** 33, (2007).

[42] N. Barnea, W. Leidemann, and G. Orlandini, Phys. Rev. C **81** 064001 (2010).

[43] S. Vaintraub, N. Barnea, and D. Gazit, Phys. Rev. C **79** 065501 (2009).

[44] T. Abe, P. Maris, T. Otsuka, N. Shimizu, Y. Utsuno, and J. P. Vary, arXiv:1107:1784v1, (2011)

[45] P. Maris, A. M. Shirokov, and J. P. Vary, Phys. Rev. C **81** 021301 (2010)

[46] V. Z. Goldberg, B. T. Roeder, G. V. Rogachev, G. G. Chubarian, E. D. Johnson, C. Fu, A. A. Alharbi, M. L. Avila, A. Banu, M. McCleskey, J. P. Mitchell, E. Simmons, G. Tabacaru, L. Trache, and R. E. Tribble, Phys. Lett. B **692** 207, (2010).

[47] A. M. Shirokov, V. A. Kulikov, A. I. Mazur, E. A. Mazur, P. Maris, and J. P. Vary, Bull. Russ. Aca. Sci. Phys. **74** 538 (2010).

[48] D. R. Entem and R. Machleidt, Phys. Rev. C **68** 041001, (2003).

[49] R. Machleidt, Phys. Rev. C **63** 024001, (2001).

[50] I. Talmi, *Simple Models of Complex Nuclei*, Harwood Academic Publishers, Switzerland (1993).

[51] P. Morse and H. Feshbach, *Methods of Theoretical Physics*, McGraw-Hill, New York (1953).

[52] A. M. Shirokov, J. P. Vary, A. I. Mazur and T. A. Weber, Phys. Lett. B **644**, 33 (2007)

[53] A. M. Shirokov, J. P. Vary, A. I. Mazur, S. A. Zaytsev and T. A. Weber, Phys. Lett. B **621**, 96 (2005)

[54] A. M. Shirokov, A. I. Mazur, S. A. Zaytsev, J. P. Vary and T. A. Weber, Phys. Rev. C **70**, 044005 (2004)

[55] M. Abramowitz and I. A. Stegun, *H*andbook of Mathematical Functions, Dover Publications (1965).

[56] J. Cullum, *Lanczos algorithms for large symmetric eigenvalue computations.* Birkhauser Pubishing, Boston (1985).

[57] C. Lanczos, J. Res. Nat. Bur. Standards, Sect. B **45**, 255 (1950)

[58] G. R. Satchler, *Direct Nuclear Reactions*, Clarendon Press, Oxford (1983).

[59] J. Suhonen, *From Nucleons to Nucleus: Concepts of Microscopic Nuclear Theory*, Springer, Berlin (2007).

[60] A. Bohr and B. Mottelson, *Nuclear Structure*, W.A. Benjamin, New York (1969).

[61] J. W. Negele, Phys. Rev. C **1** 1260 (1970).

[62] A. M. Shirokov, A. I. Mazur, J. P. Vary and E. A. Mazur, Phys. Rev. C **79**, 014610 (2009)

[63] S. C. Pieper, R. B. Wiringa, J. Carlson, Phys. Rev. C **70**, 054325 (2004)

[64] A. Nogga, P. Navrátil, B. R. Barrett and J. P. Vary, Phys. Rev. C **73**, 064002 (2006)

[65] C. Forssen, E. Caurier, P. Navrátil, Phys. Rev. C **79**, 021303 (2009).

[66] P. Navrátil, J. P. Vary, W. E. Ormand and B. R. Barrett, Phys. Rev. Lett. **87**, 172502 (2001)

[67] R. Roth, T. Neff, H. Feldmeier, Prog. Part. Nucl. Phys. **65**, 50-93 (2010)

[68] U. van Kolck, Phys. Rev. C **49**, 2932 (1994).

[69] E. Epelbaum, A. Nogga, W. Gloeckle, H. Kamada, U. G. Meissner and H. Witala, Phys. Rev. C **66**, 064001 (2002)

[70] D. R. Entem and R. Machleidt, Phys. Rev. C **68**, 041001 (2003)

[71] I. Stetcu, B. R. Barrett, P. Navrátil and J. P. Vary, Phys. Rev. C **73**, 037307 (2006)

[72] J. L. Friar, J. Martorell, and D. W. L. Sprung, Phys. Rev. A **56**, 4579 (1997).

[73] W. Nortershauser, T. Neff, R. Sanchez, I. Sick, Phys. Rev. C **84**, 024307 (2011).

[74] R. Sanchez *et al.*, Phys. Rev. Lett. **96**, 033002 (2006).

[75] S. C. Pieper, V. R. Pandharipande, R. B. Wiringa and J. Carlson, Phys. Rev. C **64**, 014001 (2001).

[76] L. E. Marcucci, M. Pervin, S. C. Pieper, R. Schiavilla, R. B. Wiringa, Phys. Rev. C **78**, 065501, (2008).

[77] M. Pervin, S. C. Pieper, and R. B. Wiringa, Phys. Rev. C **76**, 064319, (2007).

[78] S. Vaintraub, N. Barnea, and D. Gazit, Phys. Rev. C **79**, 065501 (2009)

[79] F. Ajzenberg-Selove, Nucl. Phys. A **490**, 1 (1988).

[80] D.R. Tilley, C.M. Cheves, J.L. Godwin, G.M. Hale, H.M. Hofmann, J.H. Kelley, C.G. Sheu, and H.R. Weller, Nucl. Phys. A **708**, 3 (2002).

[81] D.R. Tilley, J.H. Kelley, J.L. Godwin, D.J. Millener, J.E. Purcell, C.G. Sheu, and H.R. Weller, Nucl. Phys. A **745**, 155 (2004).

[82] G. Audi, O. Bersillon, J. Blachot, A.H. Wapstra Nucl. Phys. A **729**, 3 (2003).

[83] P. Maris, Unpublished

[84] S. Shlomo and M. Prakash, Nuc. Phys. A **357** 157 (1981).

[85] J. Hüfner and M. C. Nemes, Phys. Rev. C **23** 2538 (1981).

[86] H. S. Kohler and H. Flocard, Nucl. Phys. A **323** 189 (1979).

[87] M. Durand, M. Brack, and P. Shuck, Z. Phys. A **286**. 381 (1978).

[88] K. Yabana, Prog. Theo. Phys. **76** 414, (1986).

[89] R. Roth, P. Navrátil, Phys. Rev. Lett. **99**, 092501 (2007).

[90] R. Roth, Phys. Rev. C **79**, 064324 (2009)

[91] T. Dytrych, K. D. Sviratcheva, C. Bahri, J. P. Draayer, J. P. Vary, J. Phys. G **35**, 095101 (2008).

[92] T. Abe, P. Maris, T. Otsuka, N. Shimizu, Y. Utsuno and J. P. Vary, arXiv:1204.1755

[93] P. Löwdin, Phys. Rev. **97**, 1474 (1955)

[94] P. Navrátil, Phys. Rev. C **70**, 014317 (2004).

[95] Wolfram Research, Inc., *Mathematica*, Version 8.0, Champaign, IL (2010).

[96] K. Suzuki, Prog. Theor. Phys. 68, 1999 1982; K. Suzuki and R. Okamoto, ibid. 92, 1045 1994.

[97] S. Abrahamyan, Z. Ahmed, H. Albataineh, K. Aniol, D. S. Armstrong, T. Averett, B. Babineau, A. Barbieri, V. Bellini, R. Beminiwattha, J. Benesch, F. Benmokhtar, T. Bielarski, W. Boeglin, A. Camsonne, M. Canan, P. Carter, G. D. Cates, C. Chen, J.P. Chen, O. Hen, F. Cusanno,M. M. Dalton, R. De Leo, K. de Jager,W. Deconinck, P. Decowski, X. Deng, A. Deur, D. Dutta, A. Etile, D. Flay, G. B. Franklin, M. Friend, S. Frullani, E. Fuchey, F. Garibaldi, E. Gasser, R. Gilman, A. Giusa, A. Glamazdin, J. Gomez, J. Grames, C. Gu, O. Hansen, J. Hansknecht, D.W. Higinbotham, R. S. Holmes,

T. Holmstrom, C. J. Horowitz, J. Hoskins, J. Huang, C. E. Hyde, F. Itard, C.M. Jen, E. Jensen, G. Jin, S. Johnston, A. Kelleher, K. Kliakhandler, P. M. King, S. Kowalski, K. S. Kumar, J. Leacock, J. Leckey IV, J. H. Lee, J. J. LeRose, R. Lindgren, N. Liyanage, N. Lubinsky, J. Mammei, F. Mammoliti, D. J. Margaziotis, P. Markowitz, A. McCreary, D. McNulty, L. Mercado, Z.-E. Meziani, R.W. Michaels, M. Mihovilovic, N. Muangma, C. Munoz-Camacho, S. Nanda, V. Nelyubin, N. Nuruzzaman, Y. Oh, A. Palmer, D. Parno, K. D. Paschke, S. K. Phillips, B. Poelker, R. Pomatsalyuk, M. Posik, A. J. R. Puckett, B. Quinn, A. Rakhman, P. E. Reimer, S. Riordan, P. Rogan, G. Ron, G. Russo, K. Saenboon-ruang, A. Saha, B. Sawatzky, A. Shahinyan, R. Silwal, S. Sirca, K. Slifer, P. Solvignon, P. A. Souder, M. L. Sperduto, R. Subedi, R. Suleiman, V. Sulkosky, C. M. Sutera, A. Tobias,W. Troth, G. M. Urciuoli, B.Waidyawansa, D.Wang, J. Wexler, R. Wilson, B. Wojtsekhowski, X. Yan, H. Yao, Y. Ye, Z. Ye, V. Yim, L. Zana, X. Zhan, J. Zhang, Y. Zhang, X. Zheng, and P. Zhu, Phys. Rev. Lett. **108**, 112502 (2012)